III. Results

The results show that through anodization of titanium, a nanotubular oxide film was successfully created (Figure 1and 2). OB proliferation experiments upon electrical stimulation (Figure 3 and 4) showed that under 15V of electrical stimulation, anodized nanotubular titanium had the highest cell density. When long term OB functions (Figure 5) were assessed using 15V of electrical stimulation, it was found that coupling the effects of oxide nanotubular titanium morphology and electrical stimulation gave the most improved OB cell functions with respect to non-stimulated conventional titanium. Moreover, the anodized nanotubular titanium showed lower FB density after 5 days of culture (data not shown).

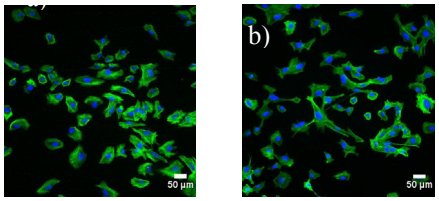

Figure 3: Fluorescently labeled OBs cultured on a) non-stimulated conventional and b) 15V stimulated anodized nanotubular titanium.

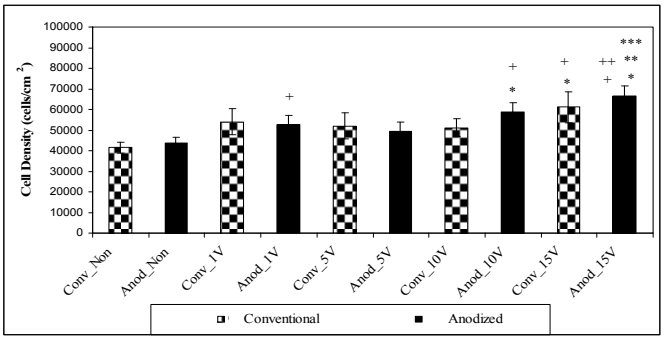

Figure 4: OB proliferation upon electrical stimulation at day 5. Values are mean ± SEM, n=3, *p<0.05 compared to Anod_Non, **p<0.05 compared to Anod_1V, ***p<0.05 compared to Anod_5V, +p<0.05 compared to Conv_Non, ++p<0.05 compared to Conv_10V.

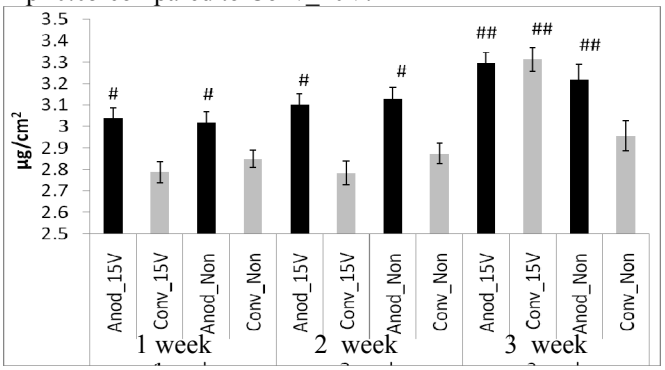

Figure 5: Calcium deposition after 1, 2 and 3 weeks of culture. Values are mean ± SEM, n=3, #p<0.05 compared to its conventional titanium counterpart at week 1 and 2. ##p<0.05 compared to 3 week Conv_Non.

The co-culture experiments indicated that the anodized nanotubular samples stimulated with 15V had higher OB and similar FB density with respect to the non-stimulated conventional titanium samples (Figure 6). Similar results were also observed when the seeding densities were varied to 1OB-2FB and 2OB-1FB (data not shown). Finally, up to 3 day S. Aureus proliferation experiments showed a decrease in bacteria OD not only upon anodization but also upon electrical stimulation, showing evidence for the anti-bacterial effects of coupling a nanofeatured surface with electrical stimulation.

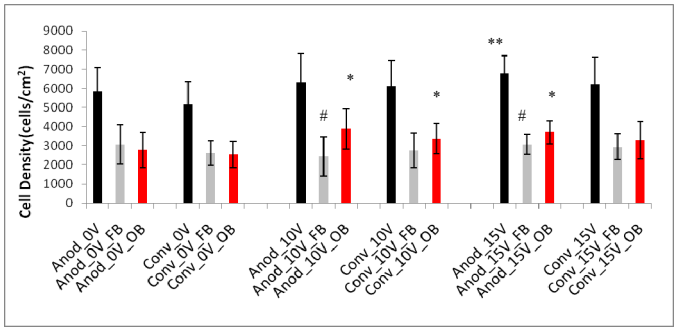

Figure 6: OB, FB and total cell densities upon electrical stimulation after 5 days. Values are mean ±SEM, n=3, *p<0.05 with respect to conv_0V_OB, #p<0.01 compared to osteoblast counterpart at the same voltage, **p<0.05 compared to conv_0V.

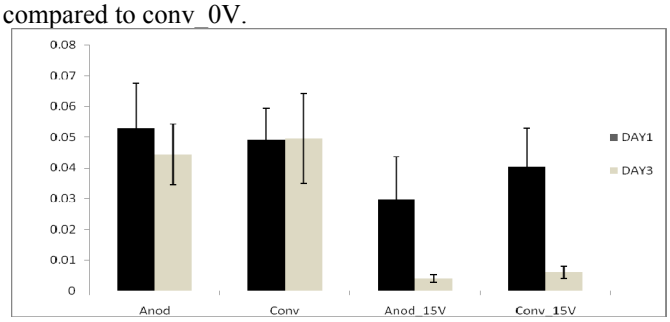

Figure 7: a) S. Aureus proliferation at day 1 and 3. Values are mean ± SEM, n=2.

IV. Conclusions

The combined effect of electrical stimulation and the creation of a nanotubular oxide film enhanced OB functions and at the same time decreased FB and S. Aureus proliferation (possibly leading to less callus formation and less severe problems infection issues), important for improving titanium for orthopedic applications.

Acknowledgement

The authors would like to thank Hermann Foundation for funding.

References

[1] R.L. Price, L.G. Gutwein, L. Kaledin, F. Tepper, and T.J. Webster, "Osteoblast function on nanophase alumina materials: Influence of hemistry, phase, and topography," Journal of Biomedical Materials Research 67A:1284-1293 (2003).

Optimization Metrics for the Design of Filament Array-based Linear Force Transducers

R.R. Agayan[1], R. Tucker[2], H. Hess[1*]
[1]Department of Biomedical Engineering, Columbia University, 363B Engineering Terrace, MC 8904, New York, NY 10027
[2]Department of Bioengineering and Therapeutic Sciences, University of California, San Francisco, San Francisco, CA 94158
Email: hh2374@columbia.edu

***Abstract*—Dense, planar arrays consisting of molecular motors and their complementary filaments have been proposed for the bottom-up construction of a hybrid actuator. The following design metrics were established to quantify filament array quality defined as efficiency of force transduction along a single direction: number density, spatial distribution, orientation distribution. Theoretical models describing the inherent randomness involved in manipulating nanoscale filament structures were used to determine achievable optimums for each design metric. These optimization limits were then validated by analyzing fabricated unipolar filament arrays based on the microtubule-kinesin system.**

I. Introduction

Force-generating biomolecular motors, or protein-based machines, along with the filamentous structures that guide them, have been recognized as attractive means for accomplishing a fundamental aim of nanotechnology—the incorporation of moving parts in useful nanoscale devices. For synthetic biologists [1], motor proteins are ideal tools because they are genetically modifiable and can be bacterially expressed, thus enabling the synergistic combination of rational design plus biological functionality at the molecular scale. Furthermore, biomolecular engines convert chemical energy in the form of adenosine triphosphate (ATP) into mechanical work without the need to first create thermal energy, hence surpassing limitations due to Carnot cycle efficiency in modern diesel and Otto engines.

Motor proteins are employed in synthetic environments such as lab-on-a-chip devices for drug delivery and active transport [2]. Typically, they are configured in what are known as gliding motility assays in which filaments glide atop a layer of force-generating motors. For example, kinesin-powered shuttle systems have been fabricated to transport biological nanoscale cargo via individual microtubules (MTs) gliding on surface-adhered linear protein tracks [3].

The hierarchical organization of molecular motors found in muscle suggests that multiplication of the involved forces can be achieved through the formation of arrays of nanoscale filaments and coupled motors [4-6] to create a macroscale linear actuator. To understand the organizing principles that enable such scaling, we have proposed our own bottom-up design of a mechanical bionanodevice based on the kinesin-MT system, as shown in Fig. 1. In this project, we considered the desired properties of such high quality planar filament arrays for macroscopic force generation, developed metrics for characterizing these structures for optimization purposes, and validated these using both theoretical and experimental models of flow-aligned unipolar MT arrays.

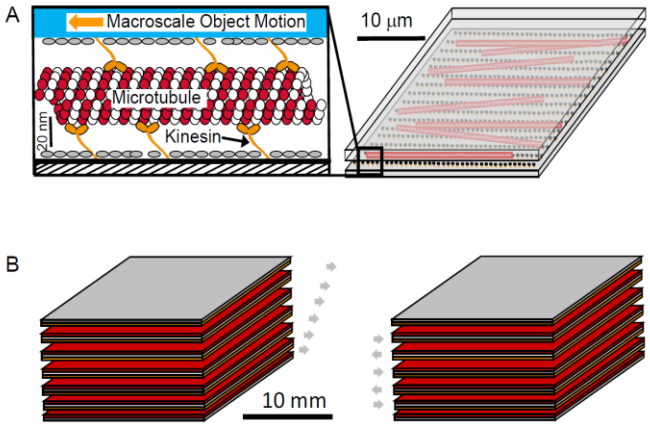

Fig. 1 Bottom-up hierarchical design of a macroscale hybrid linear force actuator comprised of nanoscale components. (A) A dense unipolar array of aligned microtubules, each bound between two substrate layers by numerous coupled motors, provides force multiplication. (B) Several stacked layers provide velocity multiplication.

II. Methods

To ascertain the organizing principles of a molecular engine, we established rational design metrics that quantify filament array quality, specifically efficient force transduction over the full extent of the array. We then determined the achievable optimum for each parameter based on theoretical considerations of the fabrications methods. The metrics are number density, spatial distribution and orientation distribution of filaments.

A. Number Density

The maximal force of an array is expected to scale with the total number of filament-motor interactions which scales with the number density of filaments for a given average filament length and dense motor spacing. In practice, the maximum achievable filament number density can depend on the filament type, method of alignment and binding strength of the filaments to the substrate.

B. Spatial Distribution

The spatial distribution of filaments versus voids suggests

the degree of conformality needed between the two surfaces to accommodate surface roughness at the nanoscale. Filament distributions that deviate from pure randomness can show clustering or regularity that may signal motor defects and reduce overall efficiency.

C. Orientation Distribution

For an ensemble of filaments, the standard deviation of orientation angle with respect to some fixed alignment angle provides a measure of the efficiency of force transduction along a certain direction. This directionality depends on the effectiveness of the filament isopolar alignment method.

Each metric is general for any type of filament (e.g. actin or MTs) and addresses a particular engineering challenge in the fabrication of an array that will adequately scale-up force generation. To determine the achievable optimum for each metric, we developed theoretical models to describe the process of array formation, i.e. Poisson-distributed center of mass coordinates in a random point field and fluctuations in the orientation of the filament tip that obeyed Brownian statistics.

III. Materials

To validate the theoretical models used to establish optimal values of our design parameters for filament-motor-based force generators, isopolar MT array structures were fabricated using shear-flow alignment and subsequently imaged on a fluorescence microscope (see Fig. 2).

Purification of full length, wild-type kinesin was accomplished using a previously described procedure [7]. MTs polymerized from rhodamine-labeled tubulin were diluted in buffer solution containing taxol for stabilization at 20°C. A flow cell was made by sandwiching two microscope cover slips with double-sided tape through which solutions were flowed. A casein solution passivated the inner surfaces followed by kinesin. MTs, antifade, and adenosine 5'-(β,γ-imido) triphosphate (AMP-PNP, a non-hydrolyzable ATP analog) in buffer was perfused into the flow cell and allowed to bind to the kinesin-coated surface. Alignment solution (buffer, antifade, and ATP) was perfused into the flow cell to initiate motility. To achieve high flow rates for MT alignment, about 700 µl of alignment solution were added continuously to one end of the flow cell while excess was removed from the other end of the flow cell with a P200 pipette tip connected to vacuum. Alignment times ranging from 75-200 s were recorded. Glutaraldehyde was used to fix aligned MTs to the surface.

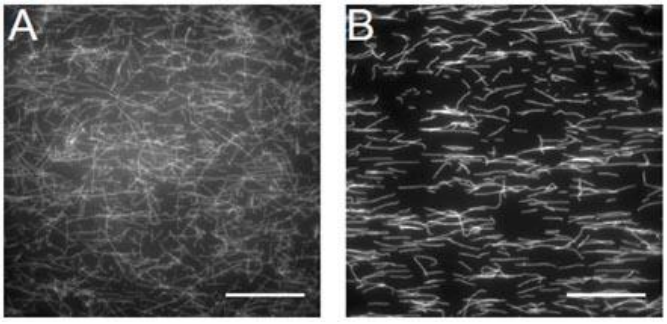

Fig. 2 Isopolar alignment of a microtubule array. (A) Microtubules first diffuse towards a kinesin-coated surface and bind to the substrate with random orientations. (B) Microtubules after shear flow alignment.

Imaging of the fixed MT array was accomplished on an inverted fluorescence microscope equipped with a mercury arc lamp for excitation, 40x air and 100x oil objectives, and a cooled CCD camera. Images recorded before and after shear-flow alignment were later analyzed using ImageJ software.

IV. Preliminary Results

Fabricated MT arrays were analyzed to determine quality based on our design metrics. Filament number density was reduced while the orientation distribution narrowed after flow alignment, suggesting that an optimal flow strength exists to induce maximum alignment without pulling MTs off the surface. Orientation distribution limitations due to random fluctuations in the angles of MT tips agree with theoretical models. The spatial arrangement of filament centers remains randomly distributed although void regions appear to have increased in size. How this change in spatial distribution affects the generated force output remains yet to be determined.

V. Conclusions

A unipolar filament array was constructed based on the microtubule-kinesin motor protein system. Its quality as a linear force transducer was quantified by measuring filament number density, spatial distribution and orientation distribution across the array. These parameters provide a means of extracting useful information from random fluctuations inherent at nanoscale dimensions, thus enabling controlled output from systems characterized by Brownian motion and stochastic behavior.

Acknowledgment

The authors would like to thank the Volkswagen Foundation for their support of this research.

References

[1] P. Schwille, and S. Diez, "Synthetic Biology of Minimal Systems", *Crit. Rev. Biochem. Mol.*, vol. 44(4), pp. 223-242, 2009.

[2] A. Agarwal, and H. Hess, "Biomolecular Motors at the Intersection of Nanotechnology and Polymer Science", *Prog. Polym. Sci.*, vol. 35(1-2), pp. 252-277, February 2010.

[3] H. Hess, J. Clemmens, D. Qin, J. Howard, and V. Vogel, "Light-Controlled Molecular Shuttles Made from Motor Proteins Carrying Cargo on Engineered Surfaces", *Nano. Lett.*, vol. 1(5), pp. 235-239, 2001.

[4] T. Brown, and W. Hancock, "A Polarized Microtubule Array for Kinesin-Powered Nanoscale Assembly and Force Generation", *Nano. Lett.*, vol. 2(10), pp. 1131-1135, 2002.

[5] L. Limberis, J. Magda, and R. Stewart, "Polarized Alignment and Surface Immobilization of Microtubules for Kinesin-Powered Nanodevices", *Nano. Lett.*, vol. 1(5), pp. 277-280, 2001.

[6] L. Limberis, and R. Stewart, "Toward Kinesin-Powered Microdevices", *Nanotechnology*, vol. 11(2), pp. 47-51, 2000.

[7] D.L. Coy, M. Wagenbach, and J. Howard, "Kinesin Takes One 8-nm Step for Each ATP that it Hydrolyzes", *J. Biol. Chem.*, vol. 274(6), pp. 3667-3671, 1999.

Generating long material gradients by convection and alternating flow in a microchannel*

M. J. Hancock, Y. Du, J. He, J. L. Villa-Uribe, B. Wang, D. M. Cropek, A. Khademhosseini
Dept. of Medicine, Brigham & Women's Hospital, 65 Landsdowne Street, Cambridge, MA 02139

Abstract— **Natural materials exhibit anisotropy with variations in soluble factors, cell distribution, and matrix properties. The ability to recreate the heterogeneity of the natural materials is a major challenge for investigating cell-material interactions and for developing biomimetic materials. Here we present a generic fluidic approach using convection and alternating flow to rapidly generate multi-centimeter gradients of biomolecules, polymers, beads and cells and cross-gradients of two species in a microchannel. A poly(ethylene-glycol) hydrogel gradient and a porous collagen gradient were generated with continuous variations in material properties. A composite material with a gelatin/hyaluronic acid cross-gradient was generated that exhibited a continuous gradient in cell attachment. This simple yet generic fluidic platform should prove useful for creating anisotropic biomimetic materials and high-throughput platforms for investigating cell-microenvironment interaction.**

I. Introduction

Anisotropic materials are highly important for many natural and engineered systems. Examples of anisotropic materials in nature include marbles, tree trunks and squid beaks. Examples of engineered anisotropic materials include the birefringent crystals of prisms, the metal wood head of golf clubs and the aluminum alloys used in aircraft and rockets. Spatial anisotropy in materials is especially prominent in cellular microenvironments in vivo where heterogeneous distributions of cells and molecules exist within spatially varying extracellular matrices (ECM). Creating chemical and material gradients to mimic the heterogeneity of cellular environments is important for investigating cell-matrix interaction [1] and for developing biomimetic materials for tissue engineering [2].

Various mechanisms can generate molecular gradients including diffusion [3], convection [4-6], differential mixing [1, 7], and dip coating with electrostatics [8]. Convection-based approaches are relatively simple, rapid, and allow the gradients to be produced in situ without additional mixing devices. Here we present a generic microchannel gradient platform employing convection and either molecular diffusion or gravity to rapidly (seconds to minutes) generate long (cm) material gradients of molecules, polymers, particles or cells. By using a syringe pump to drive fast alternating flows which continually lengthen the gradient, we have created centimeter scale concentration gradients of cells and microbeads and 'cross-gradients' of two hydrogels or two types of microbeads by using alternating flows to superpose gradients of two species.

Shear-driven or convective stretching is the primary mechanism driving gradient generation in the present work. In short, a particle in the center of the channel moves faster than one at the wall and the two spread apart at a rate proportional to the maximum channel velocity. A gradient so forms in the laterally averaged concentration profile. Ironically, diffusion acts to suppress hydrodynamic stretching by reducing the mean variation in particle speeds: slowly moving particles near the wall diffuse toward the center and accelerate, while fast moving particles near the center diffuse toward the wall and decelerate. The combined process of convection and diffusion is known as dispersion [9]. For dilute suspensions of micron sized and larger particles moving in viscous flows, diffusion is negligible. However, negatively buoyant particles settle under gravity to the channel bottom, whereupon all particles experience the same low velocity and spreading ceases. Thus, high flow rates improve stretching at all scales: for molecules, high flow rates dominate diffusion which acts to suppress hydrodynamic stretching; for microparticles such as microbeads and cells, high flow are imperative to spread the particles before they settle. The latter may explain why centimeter scale gradients of micron sized particles have not been previously generated by convection in microchannels.

II. Results

A. Gradients of biomolecules, beads, cells

All gradients were generated in a similar manner. A straight rectangular channel with inlet and outlet ports was prefilled with a solution A. Solution B was introduced at either port and pumped into the channel. A gradient in the relative concentrations of solutions A and B was so produced. The flow was halted once solution B reached the opposite end of the channel. For diffusible species, subsequent backward and forward flow segments lengthened the gradient [5]. For example, a 3cm gradient of the biomolecule fluorescein isothiocyanate-dextran (FITC-dextran) in phosphate buffer solution (PBS) was created with solution A as PBS, solution B as FITC-dextran in PBS, and with four cycles of alternating flow [5]. A single flow segment required only seconds to create 2-3cm gradients of 2, 5, and 10μm microbeads (Fig. 1a) and HUVEC cells [5].

* Research supported by NIH, NSF CAREER, US Army ERDC, Institute for Soldier Nanotechnology

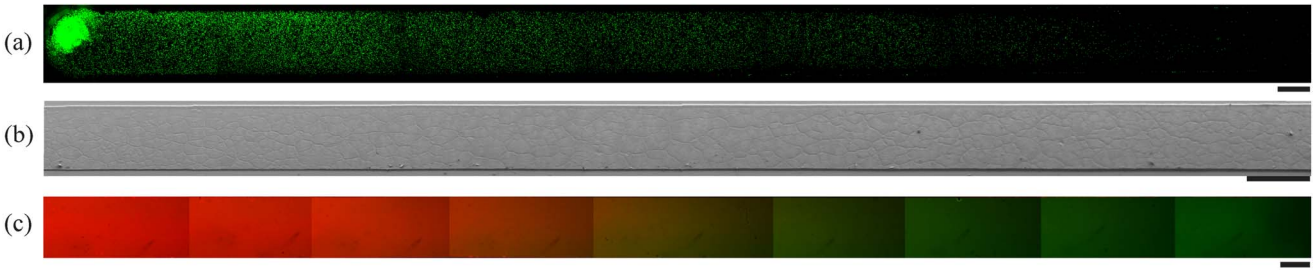

Fig. 1. Gradients of (a) 5μm beads, (b) air-dried PEG-DA thickness, and (c) a cross-gradient of FITC-dextran and rhodamine dextran. Scale bars 1mm.

The dimensionless Péclet number $Pe = UH/D$ quantifies the relative magnitudes of the rates of transport by convection and diffusion, where U is the axial flow speed, H the channel height, and D the molecular diffusivity. In our experiments, Pe ranged from approximately 400 to 4000. Gradients of FITC-dextran were produced in PBS using different flow rates. Quantification of time-lapse sequences of fluorescent images showed that gradients grew faster and longer with higher flow rates [5]. Accompanying numerical simulations of gradient length showed a similar trend: higher Péclet numbers were associated with faster gradient growth rates and longer gradients; channel geometry had a secondary effect [5].

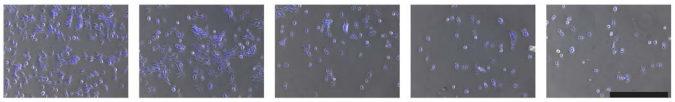

Fig. 2. Gelatin-HA cross-gradient exhibits a gradient in cell attachment. Superposed phase/fluorescent microscope images of DAPI stained cells. Images taken every ~0.5cm along channel. Gelatin/HA concentrations decrease/increase from left to right. Scale bar 500μm.

B. Hydrogel gradients

Hydrogel gradients were produced by making gradients in the pre-cursor solution, crosslinking, drying, sputter-coating and imaging with SEM. A 3cm Poly(ethylene glycol-diacrylate) (PEG-DA) hydrogel gradient was produced with solution A as 5%wt PEG-DA in PBS and solution B as 40%wt PEG-DA and 1%wt photoinitiator in PBS. The pre-cursor concentration gradient was photocrosslinked and air-dried. The resulting SEM image shows a thickness gradient (Fig. 1b, for full 3cm range see [5]). A fibril density gradient in collagen was produced with solution A containing 0.5 mg/ml of collagen and solution B containing 3.8 mg/ml of collagen. The collagen gradient was crosslinked by incubation at 37°C and then freeze-dried [5]. We have previously used a similar protocol with a passive pump to generate a toxicity gradient, a PEG-DA porosity gradient and an Arg-Gly-Asp-Ser (RGDS) gradient in PEG-DA hydrogel exhibiting a cell attachment gradient [5, 10].

C. Cross-gradients of biomolecules, beads, and hydrogels

A cross-gradient of FITC-dextran and Rhodamine-B isothiocyanate-dextran (rhodamine-dextran) was generated by taking solution A as 1 wt% FITC-dextran in PBS and solution B as 1wt% rhodamine dextran in PBS. After three cycles of alternating flow, the cross-gradient was allowed to stand for 30s and then imaged by fluorescent microscope (Fig. 1c). A similar protocol generated a cross-gradient in gelatin and hyaluronic acid (HA), which exhibited a cell attachment gradient (Fig. 2). Smooth muscle cells were seeded uniformly on the composite gel, incubated for 24h at 37°C, and then washed, leaving only attached cells [5]. We have also generated a cross-gradient of two types of microbeads [5].

III. Conclusions

Convection and alternating flow offer a rapid method of generating centimeter length gradients in the relative concentrations of any two solutions in a microchannel. The same simple protocol generated gradients of biomolecules, gels, microbeads and cells, as well as materials with gradients in their ability to regulate cellular response. Anisotropic cross-gradient materials were generated by using solutions containing different species. Our simple, versatile gradient platform should be accessible to a broad range of experimenters in the materials science and biomedical fields.

Acknowledgement

We thank Drs. Jaesool Shim, Jason Nichol, Lianyong Wang, and Ian Wheeldon for scientific and technical support.

References

[1] S. A. DeLong, J. J. Moon, and J. L. West, "Covalently immobilized gradients of bFGF on hydrogel scaffolds for directed cell migration," *Biomaterials*, vol. 26, pp. 3227-3234, 2005.

[2] E. S. Place, N. D. Evans, and M. M. Stevens, "Complexity in biomaterials for tissue engineering," *Nat. Mater.*, vol. 8, pp. 457-70, 2009.

[3] V. V. Abhyankar, M. A. Lokuta, A. Huttenlocher, and D. J. Beebe, "Characterization of a membrane-based gradient generator for use in cell-signaling studies," *Lab Chip*, vol. 6, pp. 389, 2006.

[4] Y. Du, et al., "Rapid generation of spatially and temporally controllable long-range concentration gradients in a microfluidic device," *Lab Chip*, vol. 9, pp. 761-767, 2009.

[5] Y. Du, et al., "Convection-driven generation of long-range material gradients," *Biomaterials*, vol. 31, pp. 2686–2694, 2010.

[6] J. Goulpeau, B. Lonetti, D. Trouchet, A. Ajdari, and P. Tabeling, "Building up longitudinal concentration gradients in shallow microchannels," *Lab Chip*, vol. 7, pp. 1154-1161, 2007.

[7] S. K. W. Dertinger, D. T. Chiu, N. L. Jeon, and G. M. Whitesides, "Generation of gradients having complex shapes using microfluidic networks," *Anal. Chem.*, vol. 73, pp. 1240-1246, 2001.

[8] T. P. Kunzler, C. Huwiler, T. Drobek, J. Vörös, and N. D. Spencer, "Systematic study of osteoblast response to nanotopography by means of nanoparticle-density gradients," *Biomaterials*, vol. 28, pp. 5000-5006, 2007.

[9] G. I. Taylor, "Dispersion of soluble matter in solvent flowing slowly through a tube," *Proc. R. Soc. London, A*, vol. 219, pp. 186-203, 1953.

[10] J. He, et al., "Rapid Generation of Biologically Relevant Hydrogels Containing Long-Range Chemical Gradients," *Adv. Funct. Mater*, vol. 20, pp. 131-137, 2010.

VASCULATURE FORMATION USING THREE-DIMENSIONAL CELL PRINTING TECHNOLOGY

Vivian Lee[1], Wonhye Lee[3], Seung-Schik Yoo[2], Guohao Dai[1]

[1]Department of Biomedical Engineering, Rensselaer Polytechnic Institute Troy, New York 12180, USA
[2]Department of Radiology, Brigham and Women's Hospital, Harvard Medical School, Boston, MA 02115, USA
[3]Department of Bio and Brain Engineering, KAIST, Daejeon 305-701, Republic of Korea

***Abstract*—Vascularization for adequate supplies of oxygen and nutrients is one of the challenges in tissue engineering. We report the three-dimensional cell printing technology to construct vascular structure in hydrogel scaffold which consist of endothelial cells and collagen scaffold. We constructed multi-layered, inter-connected channels within collagen hydrogel through layer-by-layer approach. Collagen hydrogel precursor was printed and cross-linked with a nebulized $NaHCO_3$. Heated gelatin hydrogel was printed within the collagen scaffold as a sacrificial material, liquefied and washed out to fabricate channels after complete gelation of collagen scaffold. The channels was perfused by syringe pump showing ability to resist 200mmHg of trans-luminal pressure. Endothelial cells which form inner lining of the vascular system was printed within collagen precursor in tubular pattern. The capability of three-dimensional cell printing technology in vasculature formation without multiple complicated processes has a potential in vascular tissue engineering. The simplicity of the technology allows it to readily incorporate other types of cells or scaffold materials to construct complex tissue structure in the future.**

I. INTRODUCTION

One of the major challenges in tissue engineering is vascularization which provides adequate supplies of oxygen and nutrients to cells within thick tissue-engineered constructs. Due to diffusion limit of oxygen and nutrients, thicker tissues have diffusion problems and cannot survive/proliferate well. Although fabrications of relatively thin tissues such as skin and bladder, and cartilage tissues are reported, obstacles in vascularization still exist for thick and complex tissue construct such as kidney, lung and heart [1]. Overcoming this problem is a critical step to the clinical applications of tissue engineering [2].

Among many enabling technologies for tissue engineering, the three-dimensional on-demand freeform fabrication can be applied for engineering vasculature in three-dimensional structure [3, 4]. Through layer-by-layer approach, cell-hydrogel or cell-extracellular matrix composite can be generated in 3-dimensional. After one layer of scaffold material is printed, cross-linking procedure such as applying chemical cross-linker or UV light is performed to make a firm scaffold layer. Several other works are conducted in similar ways to construct desired three-dimensional structures [4, 5].

To construct 3-D structure for vascular perfusion, incorporate the vascular endothelial cells into the structure is necessary to achieve the desired functions. Endothelial cells form the inner lining of the whole vascular system, and have features such as regulating permeability and forming lumens. Other important characteristics include remodeling of vascular networks (i.e. angiogenesis), thus allows tissue growth and regeneration. Recently, endothelial cell cultured in hydrogel through 3-D fabrication has been reported [3, 6]. However, vasculature formation with endothelial cell lining the fluidic channel which can provide proper perfusion of oxygen and nutrients needs to be tested.

In this study, we report the 3-D cell printing technology and the method to construct vascular structures consist of endothelial cells and hydrogels using our 3-D cell printing system, and start to test its functional integration and potential applications for vascular perfusion of tissue construct.

II. MATERIALS AND METHODS

A. Overview of 3-D cell printing system

The three-dimensional cell printing system has been developed based on 3-D solid free-form fabrication technology [4]. The system consists of a dispenser array containing 8 independently-controlled electromechanical microvalves and a 3-dimensional robotic stage (X, Y, Z axes) (Fig. 1). The system has an attachable temperature-controlled unit for printing thermo-sensitive materials. The liquid materials are dispensed by air pressure during the gate opening of the microvalve. The volume of dispensing droplet can be manipulated by controlling valve opening time and air pressure. In addition to hardware design, we developed software interface which consists of two separate computer

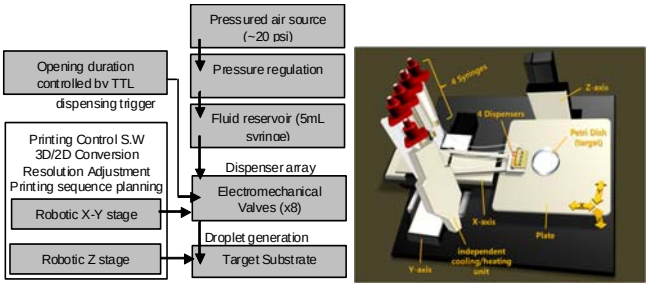

Fig. 1. Schematics and picture of the 3-D cell printing system

programs: (a) image digitizing software which convert image files to the printing sequences, (b) machine control software which actually send signals to cell printer.

B. Materials and Cell Preparation

Human umbilical vein endothelial cell (HUVEC) were cultured in 0.1% gelatin treated flask containing EGM-2 media (Lonza). For printing, HUVECs (passage 3-4) were harvested using Trypsin-EDTA solution and then, desired cell suspension density was tuned by dilution of the harvested cells in the media. As a scaffold material, chemically-crosslinkable collagen hydrogel precursor (rat tail, type I) was used. Thermo-reversible gelatin (7%) was used as a sacrificial material. $NaHCO_3$ in distilled water (0.8M) was used as a cross-linking material for the collagen hydrogel precursor.

C. Construction of hydrogel with seeded cells and channel

To construct desired shape in three-dimensional space, layer-by-layer approach was introduced to the printer system. After printing of one layer, nebulized $NaHCO_3$ was applied onto the layer for collagen gelation. It also acts as an adherent between formerly printed layer and newly printed layer. For each layer, cells and heated gelatin (40℃) were also printed in desired patterns. When the printing was completed, the engineered structure was placed in an incubator (37℃) for 30 minutes to complete the collagen gelation process and liquidify the gelatin scaffold.

III. Result

A. Construction of collagen scaffold with embedding multi-layered gelatin patterns

To demonstrate the feasibility of our method, we constructed various types of fluid channels. Fig. 2b shows four types of gelatin patterns in collagen structure. The patterns include multi-layered and interconnected gelatin channels shown in red and blue color. The minimum width of channel at 40℃ is about 400 μm (Fig. 2a).

B. Perfusion of printed channel within collagen scaffold

After printed gelatin melted away, the collagen channel was connected to a syringe pump and flow was started. The strength of the channel was tested and demonstrated to be able to resist 200mmHg of trans-luminal pressure.

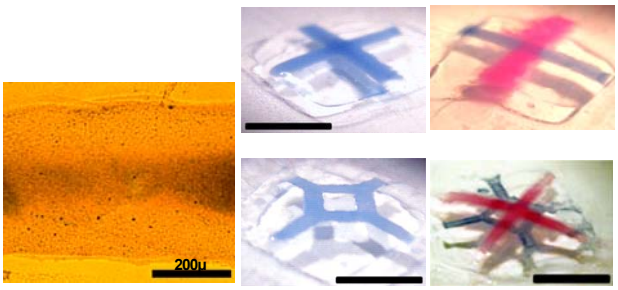

Fig. 2. (a) Image of the printed channel. (b) Multi-layered interconnected gelatin channels in collagen scaffold.

C. Vasculature patterning of HUVEC

HUVECs were printed on prepared collagen layer with various cell suspension resolutions and the cell viability of each condition was tested. The printed cells presented high viability in resolution 200~300 μm. Then we printed tubular pattern of HUVECs on collagen layer through layer-by-layer approach. The result structure was cultured in culture media for three days. HUVECs proliferated in collagen scaffold and showed integration within the scaffold.

IV. Discussion

In this study, we developed a novel 3-D cell printing technology, which provide the capability of on-demand freeform fabrication to fabricate vasculature within the hydrogel scaffold. Through layer-by-layer approach using gelatin as a sacrificial material, we constructed a collagen structure with channel and seeded endothelial cells.

Our cell printing system successfully printed both chemically-crosslinkable and thermo-reversible gel. It is also capable of dispensing endothelial cells in desired pattern with high cell viability. The printing time is about 2-5 min/layers and repeatable printing platform allows our printing system to be a rapid and high-throughput method for channel fabrication. However, compare to soft-lithographic methods, the resulted channel is limited on its resolution and size. To overcome this limitation, dispensers capable of printing smaller volume of droplets or other sacrificial materials with lower viscosity should be tested in the future.

Detail of mechanical properties of the collagen scaffold was not shown. However, we constructed 1-2 mm thickness of collagen scaffold which maintains its structure when immersed in culture media with microfluidic flow and resists 200mmHg of trans-luminal pressure. This showed that the scaffold structure has the integrity for thick tissue culture and perfusion.

We presented a capability of cell printing technology in vasculature formation without multiple complicated processes. The simplicity of the technology allows it to readily incorporate other types of cells or scaffold materials to construct complex tissue structure in the future.

References

[1] Jain, R.K., Au, P., Tam, J., Duda, D.G., and Fukumura, D. 2005. Engineering vascularized tissue. *Nat Biotechnol* 23:821-823.

[2] Borenstein, J.T., Weinberg, E.J., Orrick, B.K., Sundback, C., Kaazempur-Mofrad, M.R., and Vacanti, J.P. 2007. Microfabrication of three-dimensional engineered scaffolds. *Tissue Eng* 13:1837-1844.

[3] Cui, X., and Boland, T. 2009. Human microvasculature fabrication using thermal inkjet printing technology. *Biomaterials* 30:6221-6227.

[4] Lee, W., Debasitis, J.C., Lee, V.K., Lee, J.H., Fischer, K., Edminster, K., Park, J.K., and Yoo, S.S. 2009. Multi-layered culture of human skin fibroblasts and keratinocytes through three-dimensional freeform fabrication. *Biomaterials* 30:1587-1595.

[5] Lee, W., Lee, V., Polio, S., Keegan, P., Lee, J.H., Fischer, K., Park, J.K., and Yoo, S.S. 2009. On-demand three-dimensional freeform fabrication of multi-layered hydrogel scaffold with fluidic channels. *Biotechnol Bioeng.*

[6] McGuigan, A.P., Leung, B., and Sefton, M.V. 2006. Fabrication of cell-containing gel modules to assemble modular tissue-engineered constructs [corrected]. *Nat Protoc* 1:2963-2969.

Culturing Mouse Embryonic Stem Cells With Microcarriers in Rotary Cell Culture System

Xiuli Wang[a,b], Guofeng Wei[c], Xiaojun Ma[a]
[a]Dalian Institute of Physical Chemistry, Chinese Academy of Sciences, 457 Zhongshan Road, Dalian, P.R.China 116023
[b]Tufts University, 4 Colby Street, Medford, MA 02155
[c]The Second Affiliated Hosptial of Dalian Medical University, 467 Zhongshan Road, Dalian, P.R. China 116027

***Abstract*-Embryonic stem cells (ESCs) hold promise either as an *in vitro* model recapitulating early embryonic development or as a renewable source of therapeutically useful cells. However, 2D culture system, which is still generally utilized in ESCs differentiation strategies, has greatly impeded our learning more information about ESCs proliferation/differentiation *in situ*. Here, a high aspect ratio vessel (HARV) was adopted to support mouse ESC culture due to its promising role in allowing more complex 3D tissue formation in vitro. An increased proliferation of ESCs in HARV was observed, in keeping with their enhanced metabolic activity. Moreover, supplement of the microcarriers significantly promoted ESCs assembling into macroscopic, tissue-like organoids during the culture. The ESCs lost their "stemness" property gradually as evidenced by their decreased expression level of undifferentiating markers over time. No significant difference of the time course of ESC differentiation was observed between the HARV and the static culture. However, an enhanced capability of their mesoderm and endoderm lineages differentiation was exhibited by the ESCs in HARV, in comparison with the static culture. We conclude that this HARV-ESC culture system might not only provide more information for the developmental biology *in situ* but also be directly used for tissue engineering research.**

INTRODUCTION

Embryonic stem cells (ESCs) represent a promising source for cell transplantation because of their unique capability to give rise to different somatic cell lineages. Differentiation of ESC can be initiated either in 2D culture on a differentiation-inducing layer or by growing them in suspension where they form embryoid bodies (EBs) [1,2]. However, it has been difficult for all the current protocols to promote cell growth into higher-order structure, which is important because it might not only provide more information for the developmental biology *in situ* but also be directly used for tissue engineering applications.

A rotating wall vessel (RWV) bioreactor developed by NASA (U.S) represents a promising system for allowing formation of complex 3D tissues *in vitro*. It produces a microgravity-like environment in which cells undergo free-fall as they rotate and are subjected to extremely low fluid shear, high oxygenation of cultures, and high mass transfer. These properties allow cells cultured under this microenvironment to aggregate and grow into relatively large masses, displaying differentiation markers similar to those found in mammalian tissues [3,4]. We hypothesized that combining the appropriated physical support by the microcarrier beads incorporation; the unique culture microenvironment in the RWV bioreactor could possibly enhance the proliferation and differentiation of ESCs, generating more tissue-like 3D constructs for tissue engineering application. Here, homotypic cultures of mouse ESCs were cultivated in one particular type of RWV bioreactor, termed the high aspect ratio vessel (HARV). Their growth profile and phenotype characteristics were evaluated by morphological detection, protein and gene expression analysis. The advantages and future implementation of the RWV system in stem cell differentiation were also discussed.

MATERIALS AND METHODS

ESCs were seeded in a 55-ml HARV filled with differentiation medium. Cytodex 3 microcarrier beads were incorporated at a density of 5 mg/ml (~10 cells/microcarrier). The vessel loaded with mESC and microcarriers was placed on its rotary base and the initial rotation rate was approximately 8 rpm. Cultures with a similar seeding density under the static condition served as control. Cell proliferation was detected by crystal violet staining. Metabolic activity of the mESC was assayed by glucose/lactate concentration in the medium. SEM, TEM and immunostaining as well as real time RT-PCR were employed to characterize their morphology and phenotype characteristics.

RESULTS AND DISCUSSION

Proliferation of mESCs in the HARV was evaluated during 10 days of culture. A steady increase of the mESC concentration was observed during 8-day cultivation in HARV. The progress of cell proliferation in the bioreactor was also monitored by a measurement of glucose/lactic acid level in the culture medium. As shown in Fig.1b,c, the glucose utilization increased after day one, accompanied by an increase in media lactate in either HARV or the static cultures. The mean values for glucose utilized and lactate produced by the HARV culture were less than the static culture in the 2-4d period of cultivation.

H&E staining exhibited a less necrosis in the aggregates formed in the HARV in comparison with the static culture, indicating a better mass transfer under the unique culture condition. SEM revealed that the cells in the HARV began to associate with each other over time and "bridges" were built

between the adjacent cell-loaded beads, allowing larger ECM-rich, more tissue-like structures generation. However, only smaller aggregates with less ECM secretion were observed in the static culture. More importantly, abundant tight junctions were formed among the HARV cultures; further supporting the fact that the microenvironment provided by HARV could contribute to more integrated, tissue-like structure formation by the differentiated mESC (Fig.2).

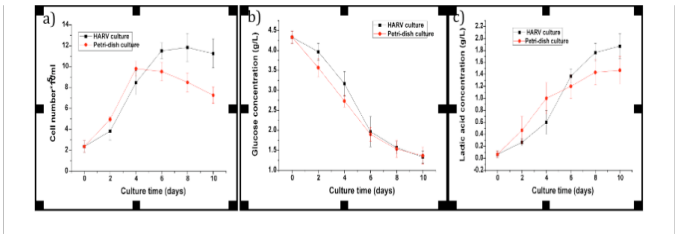

Fig.1 The growth kinetics and status of mESCs grown in the HARV (■) or in the static condition (◆). Much higher densities were reached in HARV compared with the static culture (A). Glucose concentration (B) and lactate production (C) were similar and corresponded to the cell numbers in each culture system.

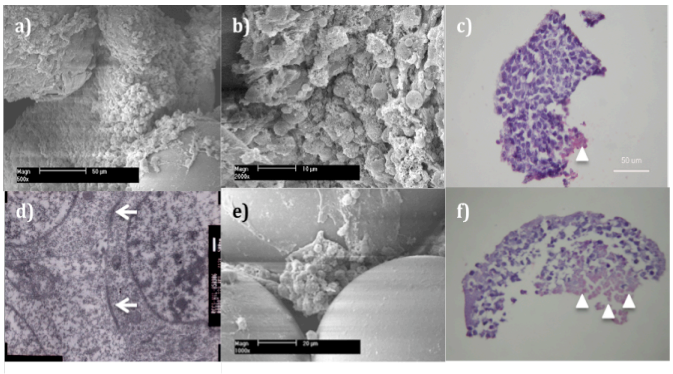

Fig. 2. Growth profile of mESCs in the HARV (a-d) and the static culture condition (e,f). Arrow notes tight junction, arrowhead notes necrosis area.

Two critical markers for the undifferentiated mESCs, AP and SSEA-1 were employed to characterize the phenotype of the mESCs in the HARV [5]. The results showed that both AP and SSEA-1 expression in the HARV cultures decreased gradually over time, predicting a loss of their undifferentiated phenotype during the process. No significant difference was observed between the HARV and the static cultures, indicating that the dynamic culture by HARV produce no effect on the time-course of ESC differentiation *in vitro* (Fig.3). However, an enhanced mesoderm and endoderm lineages differentiation capability was observed in the differentiated ESCs in the HARV, as evidenced by the significantly increased brachy, CD31 (mesoderm), and α-fetoprotein as well as gata4 (endoderm) expression level. This might be explained by the unique microenvironment produced by the RWV system, which facilitates ESC differentiation into specific lineages. This culture system provides an ideal model to study controlled differentiation of ESCs into different cell lineages.

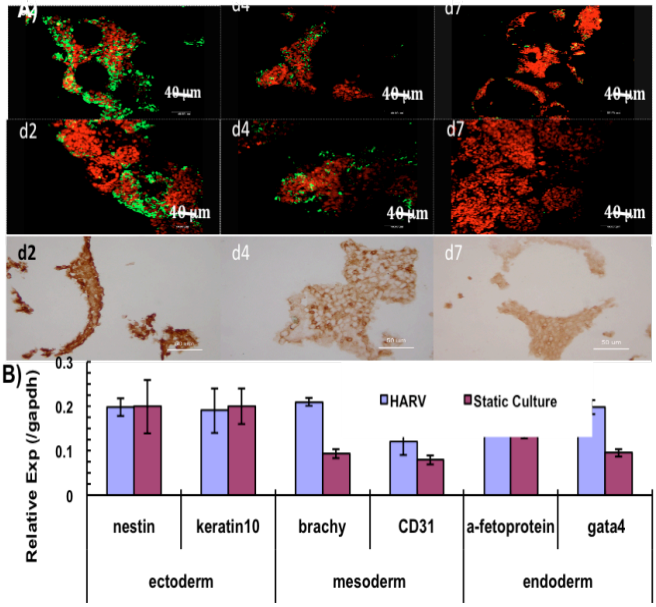

Fig. 3. Expression of SSEA-1 (top row- HARV, middle row-Static culture) and AP (bottom row) in the HARV and the static culture. B) Gene transcript expression level of mESC cultured in the HARV and the static condition.

CONCLUSIONS

A feasibility of culturing mESCs in the RWV bioreactor with microcarrier beads was described here, and our data indicate that HARV-microcarrier culture system supports mESC proliferation, differentiation and facilitates more tissue-like 3D constructs generation. Furthermore, mESCs cultured in HARV displayed an enhanced mesoderm and endoderm lineages differentiation capability. We conclude that this HARV-ESC-microcarrier culture system might not only provide more information for the developmental biology *in situ* but also be directly used for tissue engineering research.

ACKNOWLEDGEMENT

This work was supported by the National Natural Science Foundation (20236040) and National High Technology Research and Developent Programme of China (2003AA205111).

REFERENCES

[1] E.A. Mayhall, N. Paffett-Lugassy, L.I. Zon, "The clinical potential of stem cells." Curr Opin Cell Biol. 2004, vol.16, pp.713-720.

[2] J.A. Odorico, D.H. Kaufman, J.A Thomson, "Multilineage differentiation from human embryonic stem cell lines." Stem Cell. 2000, vol.19, pp.193-204.

[3] K. Dutt, S. Harris-Hooker, D. Ellerson, D. Layne, R. Kumar, R. Hunt, "Generation of 3D retina-like structure from a human retinal cell line in a NASA bioreactor." Cell Transplant. 2003, vol.12, pp.717-731.

[4] J.L. Becker , T.L. Prewett, G.F. Spaulding, T.J. Goodwin, "Three-dimensional growth and differentiation of morphologic and embryologic considerations." J Cell Biochem. 1993, vol.51, pp.29-37.

[5] X.L. Wang, W. Wang, J. Ma, X. Guo, X.J. Yu, X.J. Ma, "Proliferation and differentiation of mouse embryonic stem cells in APA microcapsule." Biotechnol Prog, 2006, vol.22, pp.791-800.

Multivalent Polypeptides for Tunable Cell Adhesion

Benjamin W. Lee, Rajib Schubert, Yuk Kee Cheung, Federico Zannier, Qian Wei, Daniele Sacchi, and Samuel K. Sia
Columbia University, 1210 Amsterdam Avenue, New York, NY 10027

***Abstract*—Cell adhesion to surfaces has applications in biomaterials science, surface chemistry, and micropatterning tehcnologies. Control of this process is currently achieved using a limited set of molecules, including fibronectin and its derived peptide RGD. Here, we use recombinant strategies to create multivalent, monodisperse polypeptides containing up to 80 repeats of RGD. By varying the number of repeats, we are able to tune the adhesion of cells to surfaces. Cells on these modified surfaces further showed strong resistance to cell delamination under fluid shear forces in a microfluidic channel [1].**

I. Introduction

Studies requiring the adhesion of cells to surfaces are often achieved with fibronectin or peptides with its derived cell adhesion motif RGD, both of which bind integrins with high affinity [2]. Previous studies have altered binding strength by changing the presentation of the RGD using cyclic molecules, and nanoclusters [2, 3]. However, these methods often involve complex synthetic strategies and do not allow for the synthesis of a monodisperse species of RGD variants

In this study, we aim to synthesize polypeptides with large and programmable number of repeats of RGD. Multivalent interactions, or the presentation of multiple copies of a receptor-lingand interaction, may offer a strategy to tune the adhesion of cells to surfaces [4]. Previous recombinant approaches generally do not control for the number or precision of the number of repeats [5, 6]. Alternatively, recursive directional ligation offers a recombinant strategy that uses interrupted palindromes to generate monodisperse repetitive polypeptides [7]. This has not been demonstrated with cell adhesive peptides. We further hypothesize that these peptides can result in precise control over the adhesion strength of cells to surfaces.

II. Materials and Methods

We sought to repeat up to 80 times the RGD sequence (Fig. 1a). To do this, we first cloned the sequence that codes for ten repeats of the peptide sequence GSGSGSGRGDS into a cloning vector containing BamHI and BglII restriction sites. We adapted a cloning technique [7] to use these two restriction enzymes to generate compatible overhangs and generate vectors with double the valency of the starting insert (Fig. 1b). The resultant vector can subsequently be used to generate inserts with increasingly large number of repeats. By controlling the number of repeats in the insert and the vector, any new insert containing a monodisperse and arbitrary valency can be obtained.

We expressed the cloned plasmids in BLR-(DE3)-pLysS *E. Coli* and purified them via His-bind chromatography and ion-exchange FPLC (10-12 mg/L culture). We confirmed the presence and molecular weight of our peptides using SDS-PAGE and mass spectroscopy (MALDI-TOF) (Fig. 2).

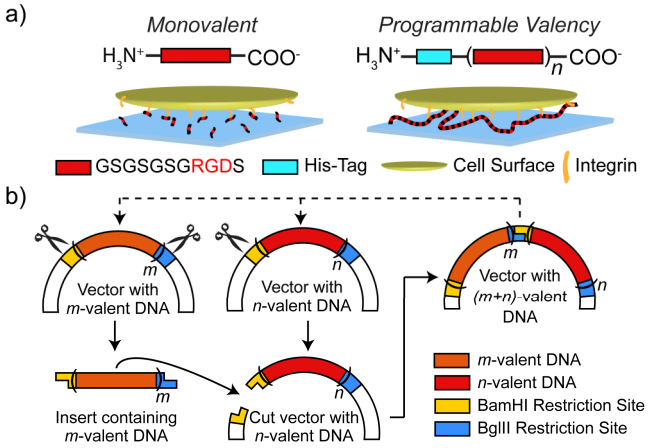

Fig. 1. Schematic diagram of cell-adhesion polypeptide and synthetic strategy. (a) Schematic of polypeptides of programmable valency. (b) Synthesis of polypeptides using recursive directional ligation.

To assay the cell adhesive properties of our synthesized peptides, they were chemically functionalized onto glass using a crosslinker system (Fig. 3a). The polypeptide reacted with NHS-PEO_{12}-Maleimide (Pierce Scientific) in solution (1 mg/mL polypeptide with 2:1 polypeptide to crosslinker ratio), and was then introduced to a microfluidic channel to react with glass silanized with 5% (3-mercaptopropyl)-trimethoxysilane in toluene (Aldrich). Microfluidic channels (400µm x 200µm x 5 mm) were made using conventional soft-lithography techniques, where a precursor of polydimethylsiloxane (PDMS) was cured against a silicon master containing the features of these channels.

After blocking for nonspecific binding, 3T3 fibroblasts (used at 80% confluence, dyed with 5 µM CellTracker Green CMFDA dye (Invitrogen), $2x10^6$ cells/mL) were seeded for 2 hours and visualized under the microscope (Fig. 3c). Cells were subjected to a shear stress of 8.5 dynes/cm^2 (100 µL/min) for 10 minutes to test resistance to delamination.

III. Results

Vectors containing 20, 30, 40, and 80 repeats of RGD were cloned and expressed. Digestion of the four vectors with BamHI and BglII yielded DNA fragments of the expected sizes (Fig. 2a). SDS-PAGE and MALDI-TOF Mass Spectroscopy reveal monodisperse species of peptides of the expected molecular weight (Fig. 2b).

Whereas the monovalent RGD peptides did not adhere cells as readily as fibronectin, multimeric polypeptides showed binding similar to that of passively absorbed fibronectin (Figure 3d). Additionally, polypeptides of higher valencies (40- and 80-valent polypeptides) resisted fluid flow when subjected to a 100 µL/min flow rate (approximate shear stress of 8.5 dynes/cm^2), approaching the level of cellular delamination observed for fibronectin (Figure 3e). The level of cellular delamination under shear was tunable depending on the number of repeats of the cell-adhesion sequence, as 40- and 80-valent polypeptides adhered cells significantly more strongly than monovalent and 20-valent polypeptides under fluid flow (Figure 3e).

IV. Discussion

Our study demonstrates a recombinant method that allows the synthesis of monodisperse cell-adhesion polypeptides without the use of prestructured scaffolding agents. Also, since long polypeptides of this type are different in three-dimensional conformation from molecules such as highly rigid dendrimers, our polypeptides may exhibit different properties *in vivo*. Indeed, this study extends the capability of proteins to be used as monodisperse functionalized polymers.

Additionally, our synthesized polypeptides exhibit enhanced binding (both statically and under shear) compared to the commonly used RGD monomer. Importantly, the level of adhesion offers an alternative class of cell-adhesion molecules that exhibit high, and now tunable, binding strengths, compared to fibronectin. The ability to tune precisely the cell-adhesion strength may be of interest to researchers who are interested in altering the strength of interactions between cells and materials in a well-defined manner, in order to study interactions between integrins and cell-adhesion molecules in a quantitative manner, develop new micropatterning technologies, or construct biomaterials with tunable biocompatibility profiles (such as cellular delamination due to shear stress in implanted materials).

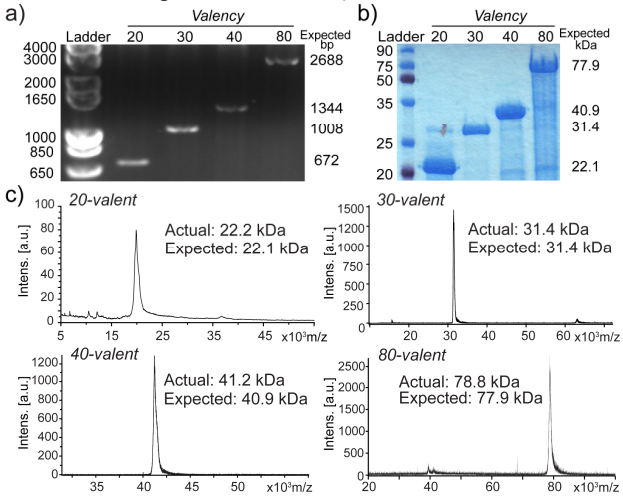

Fig. 2. Confirmation of cloned DNA and purified polypeptides. (a) Agarose gel electrophoresis (with ethidium bromide staining) of inserts from four recombinant vectors digested with BamHI and BglII. (b) SDS-PAGE (with Coomassie Blue staining) of the four expressed and purified polypeptides. (c) MALDI-TOF of the four synthesized polypeptides.

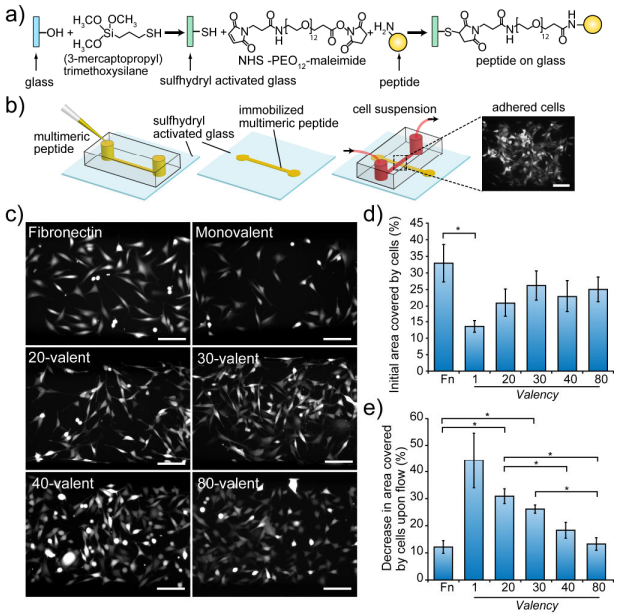

Fig. 3. Adhesion of cells to surfaces derivatized by multivalent cell-adhesion polypeptides. (a) Crosslinking chemistry used to covalently attach polypeptides to glass slides. (b) Diagram of flow experiment and micrograph of 3T3 fibroblasts adhering selectively to a region of glass derivatized by 40-valent polypeptide. Scale bar: 100 µm. (c) Micrographs of 3T3 fibroblasts seeded on glass derivitized with various polypeptides as compared with passively absorbed fibronectin. Scale bars: 100 µm. (d) Graph showing the fraction of the total area covered by cells after incubation for 2h. (e) Graph showing the fraction of cells sheared off during flow. Results are means ± SEM for n≥5. Statistical significance was determined by ANOVA (*p<0.05).

Acknowledgements

We thank the American Heart Association (Scientist Development Grant) and NSF (CAREER) for financial support. We also acknowledge financial support from the NSF East Asian and Pacific Summer Institutes (R.C.). We are grateful to Dr. Rachel Cheng and Crystal Wang of Academica Sinica for helping with the mass spectra data collection.

References

[1] Lee, B.W., Schubert, R., Cheung, Y.K., Zannier, F., Wei, Q., Sacchi, D., and Sia, S.K.: 'Strongly Binding Cell-Adhesive Polypeptides of Programmable Valencies', Angew Chem Int Ed Engl *(in press)* DOI: 10.1002/anie.200906482

[2] Hersel, U., Dahmen, C., and Kessler, H.: 'RGD modified polymers: biomaterials for stimulated cell adhesion and beyond', Biomaterials, 2003, 24, (24), pp. 4385-4415

[3] Montet, X., Funovics, M., Montet-Abou, K., Weissleder, R., and Josephson, L.: 'Multivalent effects of RGD peptides obtained by nanoparticle display', J Med Chem, 2006, 49, (20), pp. 6087-6093

[4] Mammen, M., Choi, S.-K., and Whitesides, G.M.: 'Polyvalent Interactions in Biological Systems: Implications for Design and Use of Multivalent Ligands and Inhibitors', Angew Chem Int Ed, 1998, 37, pp. 2754-2794

[5] Haider, M., Leung, V., Ferrari, F., Crissman, J., Powell, J., Cappello, J., and Ghandehari, H.: 'Molecular engineering of silk-elastinlike polymers for matrix-mediated gene delivery: biosynthesis and characterization', Mol Pharm, 2005, 2, (2), pp. 139-150

[6] Kurihara, H., Shinkai, M., and Nagamune, T.: 'Microbial expression of proteins containing long repetitive Arg-Gly-Asp cell adhesive motifs created by overlap elongation PCR', Biochem Biophys Res Commun, 2004, 321, (4), pp. 988-993

[7] Meyer, D.E., and Chilkoti, A.: 'Genetically encoded synthesis of protein-based polymers with precisely specified molecular weight and sequence by recursive directional ligation: examples from the elastin-like polypeptide system', Biomacromolecules, 2002, 3, (2), pp. 357-367

Reversible Switching of 3D Microenvironments in Extracellular Matrices and Effects on Collagen Fibers and Cell Morphology

By Brian M. Gillette, Jacob A. Jensen, Meixin Wang, Jason Tchao, and Samuel K. Sia

Department of Biomedical Engineering
Columbia University
351 Engineering Terrace
500 W 120th Street
New York, NY 10027

The local three-dimensional (3D) microenvironment of a cell is known to affect it during various processes such as tissue morphogenesis, wound healing and cancer progression.[1,2] However, the structural properties of the 3D microenvironment's extracellular matrix (ECM) does not usually change after the initial properties are set.[3-5] This abstract summarizes a method to dynamically and reversibly modify 3D ECM structure that alters its properties such as solute transport rate, cell spreading and mobility.[6]

The method utilizes a two-component ECM[7-9], in which one component provides stability and structure while the other component gels or dissolves (Fig. 1A). We used collagen I (a fibrous and cell-adhesive matrix with micropores) and alginate (a polysaccharide that lacks cell adhesion sites and is nonporous) respectively for this setup, which we hypothesized would allow us to reversibly switch between separate states of the alginate while still in a solid and naturally derived collagen ECM. We can control the state of the alginate, and thus the structure of the two-component 3D ECM, by adding or removing divalent cations, such as Ca^{2+},[10] which would crosslink and uncrosslink the alginate.

We pipetted a collagen-alginate mix into a well, which was then covered with an aluminum oxide or cellulose membrane that was permeable to small molecules but not to alginate polymer chains (Fig. 1B). To form the gel mixture, we first allowed the collagen component to gel. Then by pipetting different solutions on top of the membrane that could diffuse through to the collagen-alginate, we were able to switch back and forth multiple times between the alginate's crosslinked and uncrosslinked states by adding $CaCl_2$ and sodium citrate, a chelator of Ca^{2+}, respectively.

To test whether changes in the alginate state affect transport in the gels, we examined its diffusivity in the two-component matrices using fluorescence recovery after photobleaching (FRAP) of fluorescein isothiocyante (FITC)-tagged dextrans of 3, 70 and 500 kD. We bleached a line through the center of the samples and fit fluorescence recovery curves orthogonal to the bleached line. Pure collagen did not substantially restrict dextran diffusion (92 – 96% of the measured diffusion coefficient in water), whereas pure alginate hindered the diffusion of 70 and 500 kD dextrans. Crosslinking the alginate increased the diffusion coefficients of all three dextrans, with significant ($p < .05$) differences in the coefficient between crosslinked and uncrosslinked states for 70 and 500 kD dextrans. After crosslinking and uncrosslinking, the coefficients returned to baseline values, which corresponded to the original state before crosslinking (non-crosslinked) for all three dextrans. This suggested that the transport rates in the gels could indeed be reversibly switched by adding the appropriate calcium or citrate solution.

Changing the state of the modulatory ECM component, the alginate, could also affect the structural component, collagen. To investigate if collagen fiber structure was altered by alginate crosslinking, we looked at the collagen fiber network using confocal reflectance microscopy on collagen-alginate gels which were not fixed and did not have cells, since these two conditions would also affect fiber morphology. We then performed image segmentation to calculate collagen mesh size, which showed that the fibers had similar mesh sizes regardless of the alginate state. However, the fibers were more bundled (larger, thicker, and more sparsely distributed) and had a mesh size of approximately 30 μm in crosslinked and uncrosslinked alginate, compared to fibers and collagen mesh size of 15 μm in pure collagen. The effect of alginate on collagen fibrillogenesis is similar to that of glycosaminoglycans such as heparin.[11,12]

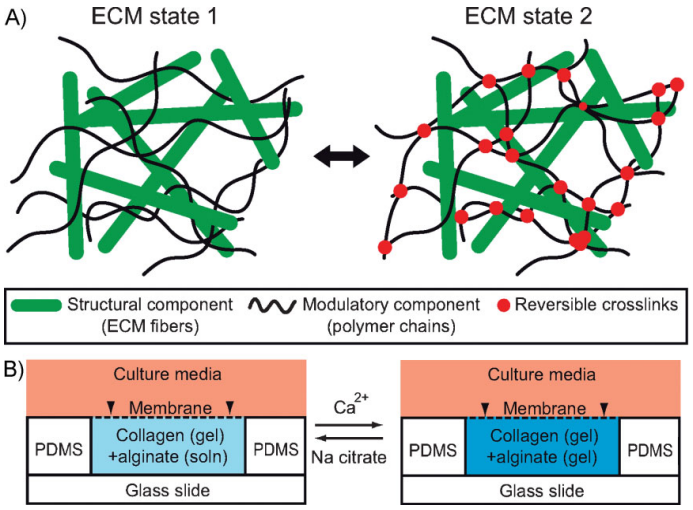

Figure 1. Schematic diagram of switching of 3D microenvironment. A) A two-component ECM in which one material serves as a structural scaffold (ECM fibers), and the other component acts as a modulatory component (polymer chains) that can be reversibly crosslinked. B) Schematic diagram of setup used to dynamically switch the crosslinking state of alginate in collagen-alginate composite gels.

We also wanted to influence not only collagen fibrillogenesis, but also cell morphology, by repeatedly switching the alginate crosslinking state, since an important function of 3D ECM is adjusting cell adhesion and spreading through its matrix pore size.[13,14] First, we examined the spreading and migration of 10T½ fibroblasts inside single- and two-component matrices. We instigated four rounds of changes in ECM structure, using Ca^{2+}-mediated crosslinking of alginate. This method is widely used in tissue engineering, and previous studies have shown that Ca^{2+} crosslinking and citrate uncrosslinking of alginate are well tolerated by various cell types.[15-19] We used brightfield microscopy to observe cell

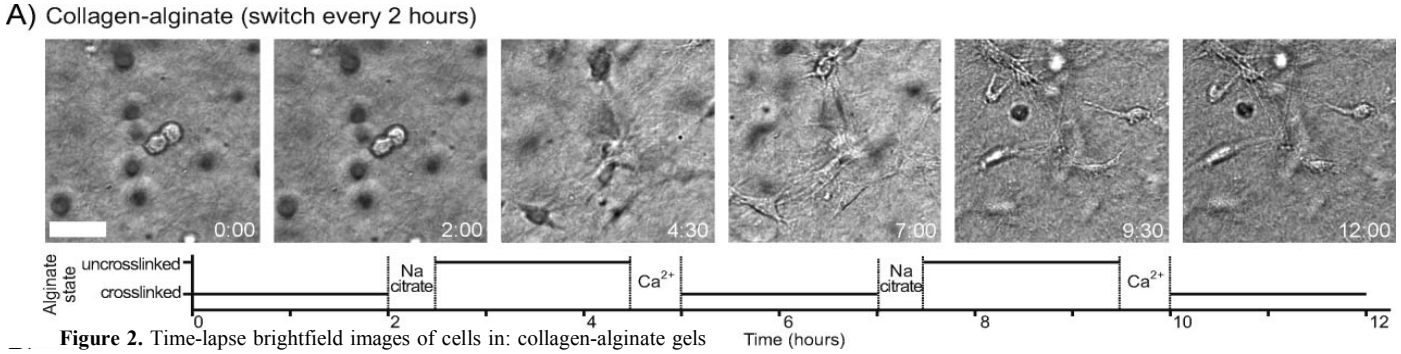

Figure 2. Time-lapse brightfield images of cells in: collagen-alginate gels undergoing dynamic switching of alginate crosslinks every 2 hours

migration and spreading over the 12 hour period, during which the four rounds of changes were made approximately every 2 hours (Fig. 2A). As expected, cell spreading and migration were restricted when the alginate was crosslinked but not when the crosslinks were removed. Most cells remained spread out after adding Na-citrate; after recrosslinking, cells also remained spread but were immobilized, though some cells moved in place. Cell area was also shown to be constant in crosslinked alginate ECM, but continually increased in pure collagen. Cell area increased overall when switching the alginate state every 2 hours. Thus, the cells that spread did not return to their compact, rounded shape upon recrosslinking of the alginate. Quantitative analysis of other cell morphology parameters corroborated the increase in cell spreading as well as elongation. Through switching alginate states multiple times, we found that crosslinked alginate inhibited cell mobility but that mobility could be restored when uncrosslinked. When gels were kept uncrosslinked for more than 2 hours, extensive gel contraction past 4 hours prevented further data collection, though the initial data trends followed that of the continuously switched gels.

Next, we used confocal microscopy to visualize the encapsulated fibroblasts' cytoskeleton, which was fixed and stained with Alexafluor-488 phalloidin to label the actin. We also used confocal fluorescence imaging to visualize collage fibers.[20] In pure alginate, cells remained round with diffuse actin staining; in collagen, cells spread and exhibited an interspersed, fibrillar pattern in cellular processes. In crosslinked alginate, cells also remained rounded (since we crosslinked it immediately after collagen gelling but before cell spreading) with diffuse actin staining. Upon uncrosslinking, the cells spread similarly as in pure collagen, with the collagen fibers becoming compact and aligned between cells. Upon recrosslinking, the cells remained spread and the actin staining did not perceptibly change, which suggests that recrosslinking does not affect cell adhesion sites.

In native tissues, changes in 3D microenvironments are associated with changes in cell growth, migration and differentiation. Using collagen I and alginate in the described two-component system provides a robust method to reversibly switch the 3D microenvironment, utilizing a widely used ECM system (Ca^{2+}-mediated crosslinking) in tissue engineering.[15-18] This specific system seems to be best suited for studies in changes in cell and tissue behavior that occur in at least tens of minutes. More precise control over dynamic ECM modifications can be gained by the addition of photoactivated calcium chelators and photouncaged calcium. The dynamic modification of other interpenetrating network hydrogels can also be performed using this two-component system. Overall, this method will complement current methods to dynamically control interactions between cells and 2D surfaces as well as cells inside 3D synthetic polymers.

[1] W. P. Daley, S. B. Peters, M. Larsen, *J. Cell Sci.* **2008**, 121, 255.
[2] J. I. Lopez, J. K. Mouw, V. M. Weaver, *Oncogene* **2008**, 27, 6981.
[3] P. Tayalia, C. R. Mendonca, T. Baldacchini, D. J. Mooney, E. Mazur, *Adv. Mater.* **2008**, 20, 4494.
[4] L. E. Freed, G. C. Engelmayr, Jr, J. T. Borenstein, F. T. Moutos, F. Guilak, *Adv. Mater.* **2009**, 21, 3410.
[5] M. S. Hahn, J. S. Miller, J. L. West, *Adv. Mater.* **2006**, 18, 2679.
[6] B.M. Gillette, J.A. Jensen, M. Wang, J. Tchao, and S.K. Sia, *Adv. Mater.* **2009**, 21, 1-6.
[7] Y. D. Park, N. Tirelli, J. A. Hubbell, *Biomaterials* **2003**, 24, 893.
[8] A. Batorsky, J. Liao, A. W. Lund, G. E. Plopper, J. P. Stegemann, *Biotechnol. Bioeng.* **2005**, 92, 492.
[9] R. A. Stile, K. E. Healy, *Biomacromolecules* **2002**, 3, 591.
[10] Y. A. Morch, I. Donati, B. L. Strand, *Biomacromolecules* **2006**, 7, 1471.
[11] A. O. Brightman, B. P. Rajwa, J. E. Sturgis, M. E. McCallister, J.P. Robinson, S. L. Voytik-Harbin, *Biopolymers* **2000**, 54, 222.
[12] M. S. Hahn, B. A. Teply, M. M. Stevens, S. M. Zeitels, R. Langer, *Biomaterials* **2006**, 27, 1104.
[13] P. Tayalia, C. R. Mendonca, T. Baldacchini, D. J. Mooney, E. Mazur, *Adv. Mater.* **2008**, 20, 4494.
[14] C. Beadle, M. C. Assanah, P. Monzo, R. Vallee, S. S. Rosenfeld, P. Canoll, *Mol. Biol. Cell* **2008**, 19, 3357.
[15] A. Banerjee, M. Arha, S. Choudhary, R. S. Ashton, S. R. Bhatia, D. V. Schaffer, R. S. Kane, *Biomaterials* **2009**, 30, 4695.
[16] H. Park, S. W. Kang, B. S. Kim, D. J. Mooney, K. Y. Lee, *Macromol. Biosci.* **2009**, 9, 895.
[17] L. Penolazzi, E. Tavanti, R. Vecchiatini, E. Lambertini, F. Vesce, R. Gambari, S. Mazzitelli, F. Mancuso, G. Luca, C. Nastruzzi, R. Piva, *Tissue Eng. Part C* **2009**, DOI: 10.1089/ten.tec.2008.0582.
[18] C. Chu, J. J. Schmidt, K. Carnes, Z. Zhang, H. J. Kong, M. C. Hofmann, *Tissue Eng. Part A* **2009**, 15, 255.
[19] K. Masuda, R. L. Sah, M. J. Hejna, E. J. Thonar, *J. Orthop. Res.* **2003**, 21, 139.
[20] Y-l. Yang, L. J. Kaufman, *Biophys. J.* **2009**, 96, 1566.

Analyte Capture in Microfluidic Heterogeneous Immunoassays

H. Parsa, C. D. Chin, P. Mongkolwisetwara, B. W. Lee, J. J. Wang, and S. K. Sia
Columbia University
1210 Amsterdam Avenue, New York, NY 10027

***Abstract*—Despite the prevalence of microfluidic-based heterogeneous immunoassays, there is incomplete understanding of analyte capture parameters. This study presents computational results and corresponding experimental binding assays of analyte capture. Our results identify: 1) a "reagent-limited" regime, under constraints of finite sample volume and assay time; 2) a critical flow rate; 3) an increase in signal by using a short concentrated plug rather than a long dilute plug; 4) a requirement to eventually reach a reaction-limited operating regime to maximize the capture of analytes [1].**

I. Introduction

Microfluidic technologies have tremendous potential for creating portable health diagnostic devices [2]. Hetereogeneous immunoassays [3], in which analytes from a sample solution bind to capture molecules immobilized on solid surfaces, can leverage efficient mass transfer to point-of-care tests [4]. An improved understanding and optimization of assay parameters, especially under "real-world" constraints (such as limited reagent or sample volume, assay time, and capture area) may benefit point-of-care assays. Previous studies have built general theoretical models; however, it remains unclear what assay parameters under real-world assay conditions should be. In this paper, we use computational analysis and experimental binding assays to study capture dynamics in microfluidic-based heterogeneous immunoassays.

II. Materials and Methods

A. Theoretical background

The processes considered in our computational model are all governed by the following parameters (Fig. 1A):

- geometrical parameters (channel width (w), height (h), binding surface or patch length (L), pre-patch length (L_0))
- reaction constants of the receptor-ligand pair (association constant (k_{on}), dissociation constant (k_{off}))
- microfluidic conditions (pressure (P), flow rate (Q), time of assay (t), surface-bound antibody concentration (C_{so}))
- molecular properties (analyte concentration (C_o), solute diffusivity (D), surface diffusivity (D_s))

B. Numerical Simulation

We used the multi-physics capability of the software COMSOL (COMSOL AB, Stockholm, Sweden) to solve the partial differential equations (PDEs) for convection-diffusion and surface reaction. We solved the convection-diffusion PDE over the entire domain, and simultaneously solved the reaction PDE over the capture zone for C_s based on C derived from the convection-diffusion PDE.

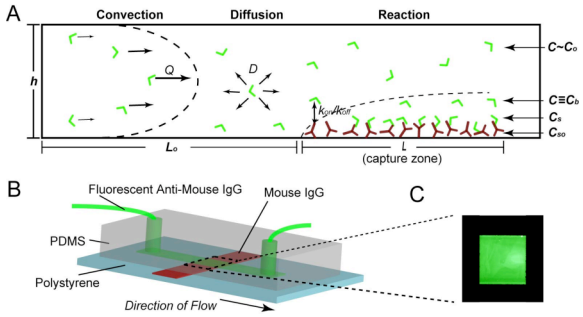

Fig. 1. (A) Major physical processes in our model: 1) Convection; 2) Diffusion; 3) Surface reaction. (B) Schematic of immunoassay. (C) Fluorescence image of captured analytes

C. Heterogeneous Immunoassay

To begin, we physically absorbed a stripe of mouse IgG antibody onto treated polystyrene plates. We then patterned parallel microchannels in an orientation orthogonal to the patterned antibody stripe using PDMS [5]. To perform an assay, we loaded a plug of fluorescence- conjugated goat anti-mouse antibody–our analyte – followed by a long plug of Tween-20/PBS in polyethyelene tubing. We injected the antibody into the microchannel using a syringe pump set at various flow rates. After the analyte passed through the channel, we washed and filled the channel, and measured the fluorescence intensity of captured antibodies using an epifluorescence microscope. We quantified the mean intensities over the capture areas using ImageJ software.

III. Results

A. Basic Description of Theoretical Model

We considered four different concentrations: three for the analyte (C_o in the bulk layer, C in the boundary layer, and C_s for analytes captured on the solid surface) and one for the surface-bound capture molecule (C_{so}). These finite-element simulations demonstrate three different and conflicting trends of amount of captured analytes as a function of Q, and suggest that modeling these immunoassays requires careful consideration of realistic operating conditions.

B. *Physical Regimes of Analyte-Capture Process*

We found that a "*reagent-limited regime*" exists at high flow rates and only under a finite volume and time constraint. Here, the capture of analytes is limited by the availability of reagents.

C. *Simulation under Real-World Constraints*

The simulations under the constraint of finite sample volume show that the captured analyte C_s plateaus at low Q and decreases at high Q (Fig. 2A). For low C_{so}, the assay can be run at a higher Q and still saturate the surface; for high C_{so}, Q needs to be lowered. Q^* is the maximum flow rate that saturates the surface and achieves the maximum signal in the shortest time. Below Q^*, one does not gain appreciable signal while slowing down the assay, and above Q^*, the assay will not reach the maximum signal but will run faster.

D. *Effect of Dilution in Larger Plug Volume: Fixed Amount*

In many diagnostic assays, a sample is often diluted 6]. Under real-world conditions, C changes significantly depending on sample volume and assay time. The finite-element results reveal that the short concentrated plug results in more captured analytes than a long dilute plug (Fig. 2C).

E. *Experimental Microfluidic Binding Assays*

We performed these experiments with the same parameters as those of the simulations. Overall, the results are consistent with the predictions of sample dilutions from finite-element modeling results. In the experiments with finite assay time, cases of dilute samples which did not pass completely through the channel at the set flow rate showed a decrease in signal compared to dilute samples which passed completely through at the set flow rate, consistent with the simulations.

F. *Physical Regimes and Saturation of Binding*

In the C_s vs. Q graph (Fig. 2A), we noted that for each flow rate Q, there exists a maximum C_{so} value for which the assay can reach saturation of binding. The graph reveals that a lower flow rate can result in the saturation of a more concentrated layer of surface-bound capture molecules. These finite-element simulations, which point to the minimum percentage of time in reaction-limited regime to achieve a saturated signal, suggest that assays can be in transport-limited regime for a significant percentage of duration of time.

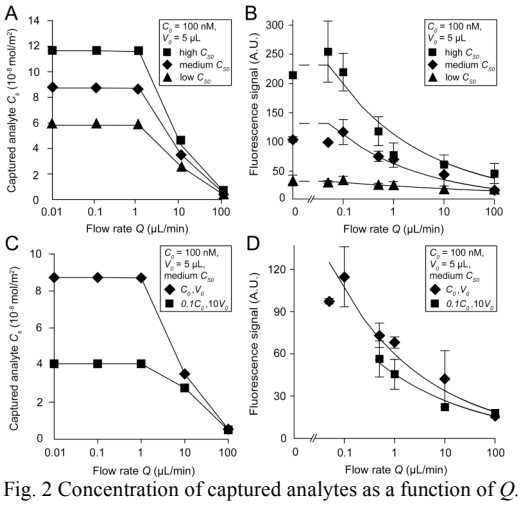

Fig. 2 Concentration of captured analytes as a function of Q.

IV. Discussion

In this study, we found that simulations under real-world constraints led to different results than simulations under idealized conditions. We noted that attempts to simultaneously apply all microfluidic advantages can obscure the desired optimal assay parameters. In this study, we focused on finite sample availability and finite assay time as the relevant constraints imposed by real-world conditions of operating microfluidic immunoassays.

Limitations of this study include: 1) The theoretical model does not capture all phenomena, and is not modeled in three dimensions; 2) The study focuses on pressure-driven flow, although some of the results may be relevant for microfluidic heterogeneous immunoassays using electrokinetic flow or for other heterogeneous assays such as surface plasmon resonance; 3) The amount and binding activity of passively adsorbed capture antibodies were not directly verified; 4) Non-specific binding was not explicitly taken into account.

V. Conclusion

The finite-element and experimental results were consistent and revealed trends that are not necessarily intuitive. For the operator of microfluidic-based heterogeneous immunoassays, some conclusions from this study include: 1) Which flow rate? One should operate at or above the critical flow rate Q^* needed to maximize the signal. Above Q^*, the user can make an informed choice in trading signal *vs.* time; 2) What sample concentration? To achieve maximum signal, one should use a short concentrated plug rather than a long dilute plug; 3) Which operating regime? To maximize analyte capture, the assay must eventually reach the reaction-limited regime, but it does not need to be in a reaction-limited regime for the entire duration of the assay. To reach the reaction-limited regime, one should operate the assay at a high flow rate only to the extent that the sample is available for the duration of the assay.

Acknowledgement

We acknowledge financial support from the Wallace H. Coulter Foundation (Early Career Award), and a Frank H. Buck Scholarship (to C.D.C.).

References

[1] H. Parsa, et.al, *Lab on a Chip*, **8**, 2062-2070 (2008).
[2] C. D. Chin, V. Linder and S. K. Sia, *Lab Chip*, 2007.
[3] D. Wild, *The Immunoassay Handbook*, Elsevier Science, 2005.
[4] J. D. Trobe and G. J. Kost, *Principles & Practice of Point-of-care Testing*, Lippincott Williams & Wilkins, 2002.
[5] E. Delamarche, D. Juncker and H. Schmid, *Adv Mat*, 2005, **17**, 2911-2933.
[6] A. J. de Mello and N. Beard, *Lab Chip*, 2003, **3**, 11N-19N.

Synthesis, Characterization and Applications of Tether Supported Biomembrane-Microsphere Assemblies

Bin He, Department of Chemical Engineering,
The City College and Graduate Center of City University of New York, New York, NY
M. Lane Gilchrist, Department of Chemical Engineering,
The City College and Graduate Center of the City University of New York, New York, NY

Abstract - **Our objective is to develop a highly miniaturized, solid-phase platform for assaying the function and inhibition of integral membrane proteins (IMPs).**

To functionalize materials with active membrane proteins, the challenge is to build stabilized, supported biomembranes in which the substrate to biomembrane spacing can be controlled to accommodate larger membrane protein. The silica microsphere (5 micron) surface was functionalized with DiNHS-PEG in order to make a tethering bridge designed to yield spacing. Confocal fluorescence microscopy was utilized to analyze the silica surface at different stages of surface modification and examine the passivation of the substrate to the formation of lipid bilayers. The lateral mobility and fluidity of the supported membranes was analyzed using fluorescence recovery after photobleaching (FRAP). Fluorescence Activated Cell Sorting (FACS) was used as a quality control step to purify the lipid tethered microsphere complexes.

These structures have been employed as a route to functionally immobilize the yeast drug efflux pump PDR5, an important anti-fungal drug target. Another intention is to develop a new platform to present molecules to stem cells within a biomimetic architecture: as laterally-mobile molecules embedded in the context of a tailored biomembrane.

Keywords - **membrane proteins, lipid bilayers, biomembranes, FACS flow cytometry, FRAP**

I. Introduction

Membrane proteins make up ~30% of the genome of a typical eukaryotic cell, yet due largely to a strict requirement of a highly mobile, native-like biomembrane microenvironment, these molecules have not been widely built into functional materials [1]. Membrane protein structure is often highly complex, typified by large, multi-subunit complexes that not only span the lipid bilayer but also contain large (>2 nm) cytoplasmic and extracellular domains that protrude from the membrane. Our current studies are focused on the implementation of a biomimetic approach to create solid-supported biomembranes interfaced with micro- and nanostructures.

Membrane proteins can be reconstituted in a functionally active in liposomes, forming proteoliposomes. However, proteoliposomes are not stable under various processing conditions (e.g., shear stress, temperature etc.), limiting their use the construction of biomembrane assemblies for drug screening applications. Lipid membranes supported by solid surfaces of various topologies present a mechanism for enhancing stability under challenging flow and processing conditions. Supported lipid membranes that contain tethering to the substrate, due to an inherent supported structure, can have higher stability compared to proteoliposomes. These materials provide a better choice for the reconstitution of membrane proteins for the development of novel materials.

II. Materials and Methodology

Materials

1-palmitoyl-2-oleoyl-sn-glycero-3-phosphatidylcholine (POPC), (Egg, Chicken) 99%, 1,2-Distearoyl-sn-Glycero-3-Phosphoethanolamine-N-[Amino(Polyethylene Glycol)$_{2000}$] (Ammonium Salt) NH_2-PEG-DSPE, 1,2-Distearoyl-sn-Glycero-3-Phosphoethanolamine-N-[Biotinyl(Polyethylene Glycol)$_{2000}$] (Biotin-PEG-DSPE) were purchased from Avanti Polar Lipids (Alabaster, AL)

p- Aminophenyl trimethoxy-Silane 90% was obtained from Gwlest. Inc. No-Weigh NHS-PEO_4-Biotin was from PIERCE. Hydroxylamine. Deionized (DI) water. Quantum dots with emission maximums at 565nm, and 705nm. Phosphate Buffer (PBS pH 10), Tris-buffered Silane (TBS pH 7), 2-(4,4-difluoro-5,7-dimethyl-4-bora-3a,4a-diaza-s-indacene-3-pentanoyl)-1-hexadecanoyl-sn-glycero-3-phosphate, diammonium salt (BODIPY® FL C5-HPA) were purchased from Invitrogen.

Methodoloy:

Liposome Formulation: These formulations were mixed using chloroform and dried overnight under vacuum, forming a thin film in approximately 1 mg per vial. 1) POPC/ Cholesterol /BODIPY-FL C_5-HPA in 0.66: 0.33: 0.01 in molar proportions 2) POPC/ Cholesterol/ NH_2-PEG-DSPE/ Biotin-PEG-DSPE/ BODIPY 530/550 in 0.61: 0.31: 0.03: 0.03: 0.01 in smolar proportions

Surface Modification: We first use Di NHS PEG crosslinking to activate amine-terminated surfaces with NHS. These surfaces are used to conjugate the amine-PEG DSPE lipids that anchor the biomembrane. we also have introduced membrane-lipid anchor-based bilayer. After the silica surface is modified by Di NHS PEG, we use both Biotin-PEG-PE and Amine-PEG-PE to form the lipid bilayer. After biotinylation of the amine surface with NHS-PEO4-Biotin, we can bridge with streptavidin to form a tethered bilayer. The tether linkage is PEO_4-Biotin: Streptavidin:Biotin-PEG-PE. We can use various fluorophore-labeled forms of streptavidin to aid in labeling sets of microspheres in barcoding schemes.

Confocal microscpy fluorescence recovery after photobleaching FRAP and Fluorescent activated cell sorting FACS were used to characterize these assemblies.

II Result and discussion

Axelrod et al. [2] developed the technique of fluorescence recovery after photobleaching (FRAP) when study the diffusive characteristics of biological molecules in living cells.

The method relies on the ability to incorporate a fluorescent label into specific protein or lipid components. When a small spot of excitation beam focuses on a region of interest area in the cell, it bleaches both the fluorescent molecules in the interested area and the molecules in an attenuated form. The analysis of FRAP provides the diffusion coefficient of the fluorescent molecule because of the diffusion of the unbleached molecules into the illuminated region. Klonis et al. [3] gives the function of FRAP. A simulated recovery curve illustrating relevant parameters of a FRAP data shows in Fig.1.

F(t) = Fluorescence intensity of the bleached spot at time t after bleaching

F_p = Prebleach intensity

F_o = Intensity immediately after bleaching

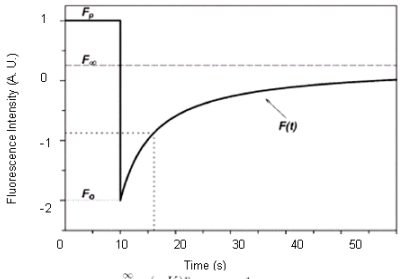

Fig. 1. A simulated recovery curve illustrating relevant parameters of a FRAP data

$$F(t) = \alpha F_p \sum_{n=0}^{\infty} [(\frac{(-K)^n}{n!}) \frac{1}{(1+n(1+\frac{2t}{\tau_D}))}] + (1-\alpha)F_o$$

$$\alpha = \frac{F_\infty - F_o}{F_p - F_o} \qquad D = \omega 2 / 4\tau_D$$

We analyze the membrane fluidity of untethered lipids and tethered ones via FRAP. The untethered lipid has a diffusion coefficient 0.09 and mobile fraction over 75%, while as to the PEG-tethered lipid, the diffusion coefficient is down to 0.032, and mobile fraction is only 66%.As we might expect, PEG DSPE adds immobile lipid obstacles to diffusion in this system. Usually the reasonable mobile fraction is over 50% for fluid bilayers, as shown in Table 1.

Table 1. FRAP data of untethered and lipid-tethered microsphere

Type of Support	Number of data sets	Diffusion coefficient (μm^2/sec)	Mobile fraction (%)
Untethered	15	0.09 ± 0.012	75.1 ± 6.1
Lipid-tethered	15	0.032 ± 0.006	66.2 ± 4.9

The modern flow cytometer analyzes and sorts cells or particles at rates up to 50,000 per second. It can perform homgeneous analysis of molecular assemblies or ligand binding by discriminating of fluorescence of molecules. Detection of fluorescence in flow cytometry can distinguish a range of cell characteristics such as protein expression, intracellular ions, surface markers et al. Cell sorters can produce highly purified, viable cell or particle populations for future analysis, as shown in Fig. 2.

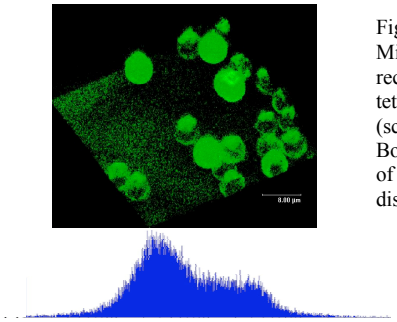

Fig. 2. Top: Confocal Microscopy 3D reconstruction of 5 µm tethered microspheres (scale bar: 5 µm)
Bottom: FACS histogram of fluorescent intensity distribution

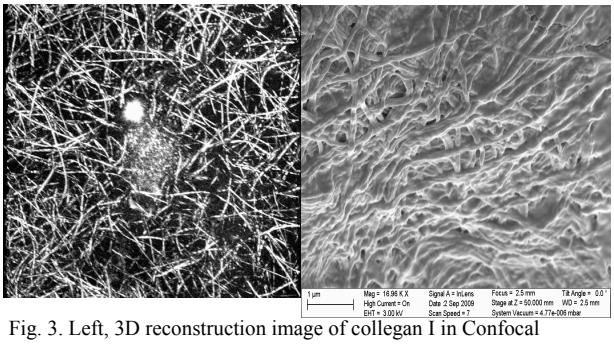

Fig. 3. Left, 3D reconstruction image of collegan I in Confocal microscopy reflaction mode;
Right, SEM image of gross apperence of collegan I

One of the applications of these tether supported biomembrane microsphere assemblies is creating 3D scaffold , which is a viable biomimetic means to present ligands/bound factors to stem cell and mimic cellular communication in the stem cell niche. Our intention is to develop a new platform to present molecules to stem cells within a biomimetic architecture: as laterally-mobile molecules embedded in the context of a tailored biomembrane. We use SEM to look at the collagen fibril morphology after fixation. Here is the SEM image showing the gross appearance of proteolipo beads in collagen matrix compare to the cofocal image, we could study it without fixation. These two Techniques could complement each other, as shown in Fig. 3.

REFERENCES

[1] Ollivon M, Lesieur S, Grabielle-Madelmont C, Paternostre M. Vesicle reconstitution from lipid-detergent mixed micelles. Biochimica et biophysica acta, 2000. 1508(1-2): 34-50.

[2] Axelrod D, Koppel DE, Schlessinger J, Elson E, Webb WW., Mobility measurement by analysis of fluorescence photobleaching recovery kinetics. Biophysical journal, 1976. 16(9): 1055-1069.

[3] Klonis N, Rug M, Harper I, Wickham M, Cowman A, Tilley L., Fluorescence photobleaching analysis for the study of cellular dynamics. Eur Biophys J, 2002. 31(1): 36-51.

Encapsulation within Nanofibers Confers Stability to the Protective Antigen Protein

K.E. Knockenhauer, K.M. Sawicka, S.R. Simon
Stony Brook University
Basic Science Tower 9-146
Stony Brook, NY 11794-8691

***Abstract*—The current vaccination paradigm for the prevention of anthrax is insufficient to deal with a potential, widespread epidemic. To solve this issue, we propose a self-administrable vaccine patch capable of delivering the antigen of interest into the skin. This patch is comprised of solid-state nanofibers containing encapsulated protective antigen (PA), a binding protein secreted by *Bacillus anthracis*. Polyvinylpyrrolidone (PVP) nanofibers, produced by the electrospinning technique, are utilized as our transdermal delivery vector because the high surface area to volume ratio that they afford maximizes contact with the skin; in turn increasing local concentration gradients of reversibly packaged PA when the hygroscopic PVP is solubilized via transepidermal water loss. Previous studies have confirmed the retention of PA immunoreactivity and functionality after the voltage-intensive electrospinning process. The study described here aimed to compare the retention of PA functionality within the nanofibers to PA in solution over a several month period; since it is theorized that encapsulation within nanofibers may confer protein stability. The functionality of encapsulated PA was retained whereas PA in solution was inactive after a 32 week incubation at 4°C; suggesting that encapsulation within nanofibers confers stability to the PA protein.**

I. Introduction

The FDA-approved vaccine, containing PA in solution, is delivered through an intramuscular injection and requires trained medical personnel to administer [1]; making the rapid inoculation of large populations difficult. We propose delivery of PA into the skin, via hydration of the stratum corneum; causing reversible and microscopic changes in structure that will allow antigen penetration [2]. PA is an 82.7 kDa binding protein that facilitates the entry of lethal factor (LF), a Zn^{2+}-dependent metalloprotease, into cells. LF cleaves members of the MAPK kinase family, preventing the up regulation of interleukin-6 (IL-6) proinflammatory cytokine production in the presence of an immunostimulant such as lipopolysaccharide (LPS) [3]. This molecular function was the basis of our *in vitro*, functionality assay; where PA function was confirmed by the down regulation of IL-6 in LPS-stimulated Mono Mac 6 (MM6) cells, a human monocytic cell line. The question of PA stability was paramount during our studies, as it is a relatively mechanically-labile and heat-labile protein; reportedly unstable after several hours storage at 4°C [4]. It was hypothesized that immobilizing PA within nanofibers may actually confer stability to the protein; so the functionality of PA stored within nanofibers was compared directly to that of PA stored in solution over a 32 week period.

II. Materials and Methods

A. Electrospinning

Electrospinning is a process by which the surface tension of a liquid polymer droplet, formed at the tip of a needle, is broken using an electric field; creating a charged, whipping jet that deposits solid nanofibers onto the grounded collecting surface due to solvent evaporation midflight. The collecting surface is lined with 4 mm x 4 mm silicon wafer substrates. Proteins can be incorporated into the fibers by solubilizing the protein of interest in the liquid polymer solution prior to electrospinning; in this case, a 30% PA, 70% PVP solution by volume. PA (List Biological Laboratories, Inc., Campbell, CA) was initially reconstituted in 0.1% Bovine Serum Albumin (BSA) H_2O at a concentration of 1.25 µg/µL. 1.3 x 10^6 g/mol PVP (Sigma Aldrich, St. Louis, MO) was reconstituted in a solvent mixture of 75% 0.1% BSA H_2O, 25% ethanol and PA was added to achieve a PA concentration of 0.375 µg/µL. The parameters used for electrospinning are listed in Table 1.

Table 1. Electrospinning Parameters

Volume	Flow Rate	Voltage	Distance from Needle to Collector
420 µL	10 µL/min	13 kV	10 cm

A 2cc Popper and Sons syringe with a 22G, 1½" blunt end stainless steel needle (Popper and Sons, Inc., New Hyde Park, NY) was utilized for this technique.

B. Sample Storage

After electrospinning, the coated silicon wafers were immediately placed into 4°C for the appropriate incubation time. The stock PA solution was stored in 20 µL aliquots of 25 ng/µL (500 ng of PA). The approximate mass of PA on each wafer was 250 ng as only 80% of the electrospinning

This work is supported by HHMI grant #52005887,
NSF AGEP grant HRD0450106, and
NIH grant GM008655.

solution deposits onto the collecting surface and each wafer is 0.2% of the total surface area of the collecting surface.

C. *Functionality Assay*

The functionality of PA encapsulated in nanofibers and in solution was determined at the following time points after electrospinning: week 0, week 1, week 2, week 4, week 8, and week 32. At each time point, 2 solution tubes and 4 wafers were removed from the storage condition and samples were diluted to 1 ng/µL using RPMI 1640 GRO media and incubated at 37°C for 1 hour. This dissolution step was conducted twice per time point (n=2). 150 µL of non-adherent MM6 cells (DSMZ, Braunschweig, Germany) at 1.33 x 10^6 cells/mL were plated to each well on a 96 well plate and allowed to equilibrate for 1 hour at 37°C. 50 µL of PA sample, either stock, solution, or electrospun solution, were added to each well (except the negative control, where 50 µL of media were added). As shown in Fig. 1, each sample set consisted of four wells, run in duplicate with the following conditions: 2 wells were not treated further, 2 were dosed with 10 µL of 10 ng/µL LF (List Biological Laboratories, Inc.), 2 were treated with 10 µL of 5 ng/µL LPS (List Biological Laboratories, Inc.), and 2 were dosed with 10 µL of both LF and LPS. The plate was then incubated for 24 hours at 37°C; the cell-culture supernatant was harvested and IL-6 concentration was assayed in each sample using an IL-6 ELISA (Invitrogen, Carlsbad, CA).

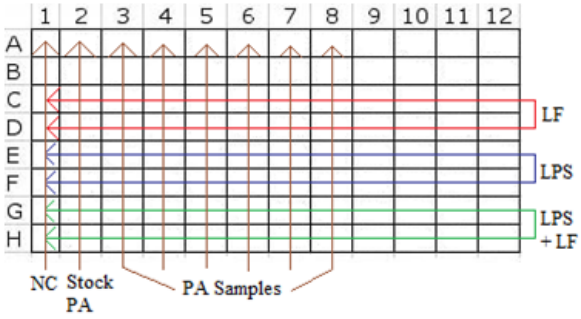

Fig. 1. Plate Map showing cell dosing scheme.

III. Results and Discussion

The IL-6 concentration values for each sample were normalized to the concentration of IL-6 up regulation due to LPS stimulation in each sample and are reported as a percentage of LPS-induced up regulation in Fig. 2. As expected, the 'No PA' negative control showed no significant difference in IL-6 up regulation in cells treated with LPS and cells treated with LPS and LF, as PA is required for LF function. The 'Stock PA' positive control demonstrated the lack of IL-6 up regulation in the LPS and LF sample indicative of functioning PA. Biological activity was retained in PA stored in nanofibers as well as in solution at the week 0, week 1, week 2, week 4, and week 8 time points. However, by week 8 it is clear that PA stored in nanofibers is retaining function better than PA in solution, as the suppression of IL-6 up regulation in the week 8 solution sample is far less than that in the week 8 nanofiber sample. By week 32, PA stored in solution is fully inactive, as there is no suppression of IL-6 up regulation, and PA stored in nanofibers is functioning comparable to the positive control.

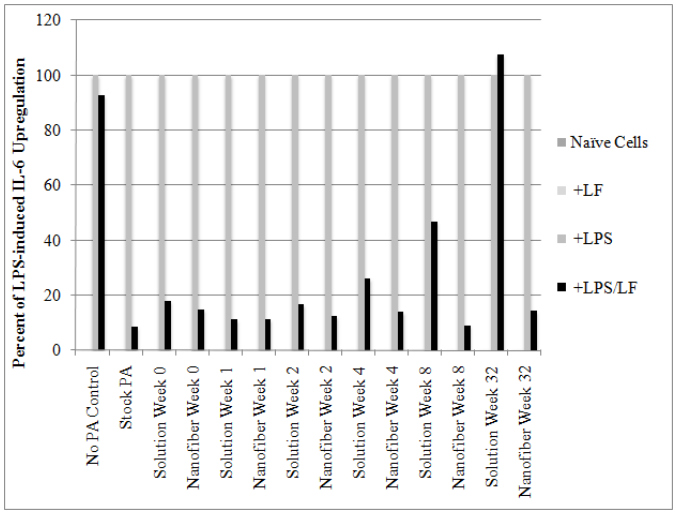

Fig. 2. Normalized IL-6 concentration data from ELISA.

IV. Conclusion

The data presented here suggests that encapsulation of PA within nanofibers confers stability to the protein and helps retain functionality significantly better than storage in solution. The next study will compare retention of these properties in our nanofibers to PA in solution containing the preservatives present in the current vaccine; namely, formaldehyde. A future study will aim to deliver encapsulated PA through an *in vitro*, human foreskin tissue model.

References

[1] S. C. Taft and A. A. Weiss. "Neutralizing Activity of Vaccine-Induced Antibodies to Two *Bacillus anthracis* Toxin Components, Lethal Factor and Edema Factor," *Clinical and Vaccine Immunology*, vol. 15, no. 1, pp. 71-75, Jan. 2008.

[2] G.M. Glenn, R.T. Kenney, S.A. Hammond, and L.R. Ellingsworth. "Transcutaneous immunization and immunostimulant strategies," *Immunology and Allergy Clinics of North America*. no. 23, pp. 787-813, 2003.

[3] S. S. Kocer, S. G. Walker, B. Zerler, L. M. Golub, and S. R. Simon. "Metalloproteinase Inhibitors, Nonantimicrobial Chemically Modified Tetracyclines, and Ilomastat Block *Bacillus anthracis* Lethal Factor Activity in Viable Cells," *Infection and Immunity*, vol. 73, no. 11, pp. 7548-7557, Nov. 2005.

[4] List Biological Laboratories, Inc. "Certificate of Analysis Recombinant Anthrax Protective Antigen (PA) Lot # 17111A1B," <http://www.listlabs.com/pdf_download.php?opt=c_of_a&id=102>.

Incorporation and Characterization of Alpha-Helical Peptide-Based Anchors into Bead-Supported Lipid Bilayer Membranes

Lina Zhong, Raymond Tu, Lane Gilchrist
The City University of New York
140th Street @ Convent Ave
New York, NY 10031

INTRODUCTION

Our aim is to design alpha-helical peptide complexes to enhance their stability and biological feasibility for the study of membrane proteins and their interactions. In on-going work, we employ ($K_3A_4L_2A_7L_2A_3K_3$) as anchoring molecules, where conjugation of the peptide with fluoresceine isothiocyanate (FITC) allows one to access a variety of chemistries (such as introducing fluorescent dye, etc.) for orthogonal modification [1].

These peptides partition within NHS-PEG3000-NHS which function as in vitro models for interactions with the membrane, will be incorporated into mimic lipid bilayer membranes (such as DOPC) supported by microbeads. We could control the receptor site densities on lipobeads by varying the mole fraction of different lipids and ligands. Moreover, the secondary structure of peptide within these micelles is characterized with circular dichroism. Lateral fluidity of the fluorescently tagged peptide is analyzed via fluorescence imaging microscopy (Confocal Microscopy) and quantified using fluorescence recovery after photobleaching (FRAP) techniques. Variations in the peptide sequence allow us to rationally investigate the influence of sequence on peptide anchor stability.

MATERIALS AND METHODS

1,2-dioleoyl-*sn*-glycero-3-phosphocholine(DOPC), which purchased from Avanti Corp., fluoresceine isothiocyanate (FITC), molecular weight 389.38g/mol. DiNHS-PEG3000, molecular weight 3000g/mol. Starting designed peptide with symmetrical sequence: $K_3A_4L_2A_7L_2A_3K_3$ [2].

Solid Phase Peptide Synthesis. SPPS using Fmoc chemistry is the frame work for our experiments, which is generally uesd in peptide synthesis. As for our experiments, instead of tranditional Fmoc-lysine(tboc)-OH, we chose Fmoc-lysine(Dde)-OH as the last residue, which enable us to couple fluorescent dye onto the original site of orthogonal protect group DDE.

Circular Dichroism. CD spectroscopy measures differences in the absorption of left-handed polarized light versus right-handed polarized light which is caused by structural asymmetry. The CD spectra can give valuable information about secondary structure of peptides, such as alpha-helix, beta-sheet and random coil [4]. Here we use Olis DSM for circular dichoism analysis.

Liposome Reconstitution. We consititute the peptide-invovled liposomes onto 5 μ m silica beads. Dissolve peptide/DOPC lipid film with PBS buffer, vortex the mixture, and sonicate the dispersion in ice-cold bath. the lipid is strongly agitated by ultrasonication. For parallel experiments, we functionalize the microbeads with Di-NHS-PEG3000 for 15min at room temperature in advance, then incubate the functionalized microbeads and non-functionalized beads with peptide-liposomes for more than 1hr. Finally, we get the mimic lipid bilayers supported by microbeads, with and without polymer cushions.

Confocal Microscopy. We use confocal microscopy as a tool to study the lateral fluidity and spatial distribution of the fluorescently tagged peptide within supported membranes [5]. Here the fluorescence recovery after photobleaching (FRAP) technique is used to characterize the mobility of peptide spanning within a supported membrane. The lateral mobility is determined by the slope of the curve. The steeper the curve

is, the faster the recovery, and the more mobility the molecules have.

RESULTS AND DISCUSSION

As for FITC-labeled peptide, we test the alpha helicity of liposome with (peptide:DOPC) molar ratio 1:10. The ensemble average helicity is 74.6%, the rest is random coils. The result is showed in figure 1. It is still a good candidate for peptide anchors self-assemblying within supported lipid bilayers.

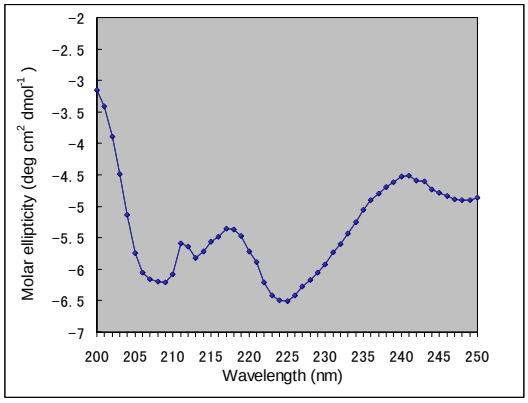

Fig. 1 Circular Dichroism Spectroscopy of FITC labeled peptide, (peptide concentration 0.2mg/ml)

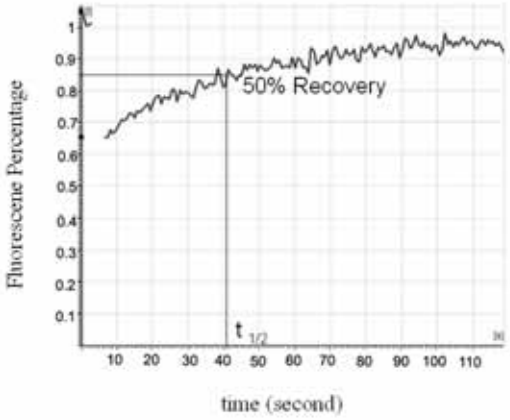

Fig.2 FRAP data of Di-NHS-PEG 3000 cushioned supported liposomoes

Quantified Lateral fluidity of the fluorescently tagged peptide using FRAP techniques:

$$F(t) = \alpha F_p \sum_{n=0}^{\infty} [(\frac{(-K)^n}{n!}) \frac{1}{(1+n(1+\frac{2t}{\tau_D}))}] + (1-\alpha)F_o$$

This equation is developed by Klonis [3] to describe the ammount of fluorescene as a function of time. In general cases, diffusion coefficient can be determined by this formula. $D = \beta \omega^2/4\tau_{1/2}$, where $t_{1/2}$ stands for the half time of recovery. A sort of typical FRAP data are showed in figure.2. We measure the mean value of half time of revocery, and calculate the value of difussion coefficient and liposome coverage respetively. The results are showed in Table.1.

Table. 1 Difussion coefficient and liposome coverage of peptide anchors within tethered and untethered liposomes

n=20	$t_{1/2}$ (s)	D (μ m^2 /s)	α (liposome coverage)
Untethered Sample	20.65	0.01219	94%
Tethered Sample	16.00	0.01574	88%

CONCLUSION

In conclusion, we synthesize the peptide, get the FITC-peptide conjugates, as well as characterized them. The peptide exhibits a high alpha helical content for stable spanning within lipid bilayers. Meanwhile, we construct supported lipid bilayers, measure the liposome coverage and determine the diffusion coefficient via FRAP techniques, which describe the important characteristics of peptide anchors within lipid bilayers.

REFERENCES

[1] Raymond S. Tu. Matthew Tirrell, *Bottom-up of biomimetic assemblies, Advanced Drug Delivery Review* 56(2004)1537-1563

[2] Burkhard Bechinger, Biophysical Journal Volume 81 October 2001, 2251-2256

[3] Nectarios Klonis, Melanie Rug, Ian Harper, Mark Wickham, Alan Cowman, Leann Tilley, Eur Biophys J (2002) 31:36-51

[4] Berova N, Nakanishi K, Woody RW (2000) *Circular dichroism: principles and application.* Wiley-VCH, New York

[5]Tamm, L.K., *Lateral diffusion and fluorescence microscope studies on a monoclonal antibody specifically bound to supported phospholipid bilayers.* Biochemistry, 1988. 27(5): p. 1450-1457

Immobilization of Chondroitin Sulfate for the Fabrication of Biomimetic Brush Structures

S Sarkar, N Ganesh, CL Schauer, E Vresilovic, M Marcolongo.
Drexel University
3141 Chestnut St
Philadelphia, PA 19104

Abstract - **Intervertebral disc (IVD) degeneration is accompanied by a loss of proteoglycans (PGs) in the nucleus pulposus (NP), resulting in a loss of charged chondroitin sulfate (CS) chains, decreasing mechanical function of the disc. PG mimics may be employed to restore NP functionality. Synthesis of CS bottle brush structures requires immobilization of CS at its terminal end. In this study, we have investigated commercially available CS for use in CS bottle brush synthesis. A primary amine (PA) at the terminal end of CS was identified and utilized to conjugate amine-reactive monomers to CS. Conjugation of monomers to CS was confirmed using the fluorescamine assay. Percent PA conjugations of 26%, 80% and 99% were seen for acrolein, acrylic acid and allyl glycidyl ether respectively. CS was also immobilized onto epoxy and aldehyde functionalized surfaces via the CS terminal primary amine. CS attachment was determined by monitoring changes in substrate sulfur content (energy-dispersive X-ray EDAX microanalysis) and surface wettability (contact angle). The modification and immobilization of CS demonstrated here will facilitate the synthesis of CS bottle brush PG mimics.***

I. Introduction

Intervertebral disc (IVD) degeneration occurs with aging, and may be a major cause of back pain. Alterations in the biochemical constituents of the IVD have been shown to coincide with aging and disc degeneration. The most significant biochemical change that takes place in disc degeneration is the loss of proteoglycans (PGs) in the nucleus pulposus (NP), resulting in a loss of the charged glycosaminoglycans (GAGs), primarily chondroitn and keratan sulfates (CSs and KSs), which are covalently attached to the aggrecan core protein.[1]

II. Statement of Purpose

The goal of this project is to develop chondroitin sulfate brush structures and investigate them as a biomimetic replacement for the ubiquitous biomacromolecule, aggrecan for the treatment and prevention of back pain originating from intervertebral disc degeneration. In this study we have developed a strategy for the end functionalization of CS and utilized this method for the immobilization of CS onto glass surface via their terminal end functionality. End-functionalized CS can be used to fabricate molecular bottle brushes via polymerization strategies such as grafting-to and grafting through, as well as brush surfaces.

* **Funding for this work has been provided by the Coulter Foundation.**

III. Background

Aggrecan and other similar PGs comprise 15% wet weight of the NP.[1] It works to resist mechanical force in the NP and provide a hydrostatic tension to the AF via molecular interactions. Aggrecan is composed of a protein core to which GAGs such as chondroitin sulfate (CS) are covalently bound in a dense array. Charged anionic groups on the GAG chains draw water into the disc and electrostatic repulsions generated between closely packed GAG chains resist deformation thereby allowing the tissue to distribute mechanical forces.[2]

IV. Methods

A. Materials.

Chondroitin-4-sulfate from bovine trachea was purchased from Calbiochem (EMD Chemicals, San Diego, CA, USA) as well as Sigma Aldrich (C9819, Sigma Aldrich, St. Louis, MO, USA). Chondroitin-6-sulfate from shark cartilage was purchased from Sigma Aldrich (27042, Sigma Aldrich). All other reagents were purchased from Sigma Aldrich and used as received.

B. Determination of CS primary amine content.

CS from various sources was assayed for their primary amine (PA) content using the fluorescamine assay. Sample fluorescence was measured on an Infinite M200 TECAN spectrophotometer with excitation/emission of 365/490nm and gain of 80. Presence of PAs is indicated by an increase in fluorescence. The number of PA/molecule of CS was calculated from the linear L-serine (one PA/molecule) standard curve assuming a CS MW of 22,000 Daltons.

C. CS-monomer conjugation.

PA reactive monomers, acrolein (via aldehyde, pH 9.4)), allyl glycidyl ether (AGE) (via epoxide, pH 9.4), and acrylic acid (via activated carboxylic, pH 7.4 acid, 2 mM EDC and 5 mM sulfo-NHS in MES buffer (0.05M MES, 0.5M NaCl), pH 6.0 for 15 min) were reacted with CS and subsequently assayed for their PA content using the fluorescamine assay. All monomer-CS solutions were allowed to mix at least 4hrs. The % of PAs in the CS sample conjugated to monomer is indicated by the % decrease in PA content which was calculated as

$$\left[\frac{[PA]\ in\ CS\ without\ monomer - [PA]\ in\ CS\ with\ monomer}{[PA]\ in\ CS\ without\ monomer}\right] * 100\%$$

D. Surface Modification with CS.

Epoxide and aldehyde functionalized glass slides were purchased from Genetix and incubated in CS solution (pH 9.4, 4hrs at room temperature). Slides were subsequently rinsed to remove any adsorbed CS. Un-functionalized glass slides were similarly prepared as control samples. Changes in surface hydrophilicity were measured by contact angle and surface sulfur content by Energy-dispersive X-ray (EDAX) microanalysis using an environmental scanning electron microscope (ESEM, FEI XL30 with EDS).

V. Results

A. CS PA content.

The presence of PAs in CS from various suppliers was investigated. CS-4 from the supplier Calbiochem contained 6.88 +/- 0.51 PAs / CS molecule. CS-4 and CS-6 from Sigma had 3.2+/- 0.29 and 2.82 +/- 0.32 PAs / CS molecule respectively. The repeat CS disaccharide does not contain PAs however PAs may be available at the terminal end of CS as a result of the cleavage that occurs in isolating CS from the PG core [3, 4]. At least one PA detected is expected to be on the terminal end of CS, and as such, this PA will be most available for conjugation allowing for terminal-end functionalization of CS. The high level of PAs / CS seen in the Calbiochem samples may be attributed to deacetylation of the GalN sugar during processing.. CS-4 in particular, is widely utilized in therapeutic settings therefore CS-4 from Sigma was chosen for use in future studies [5].

B. CS-monomer conjugation at the PA site.

When CS was reacted with a functional monomer in solution, the PA signal decreased with increasing monomer concentration, indicating an interaction between the CS PA and the amine reactive functional group in the monomer **(Figure 2)**.

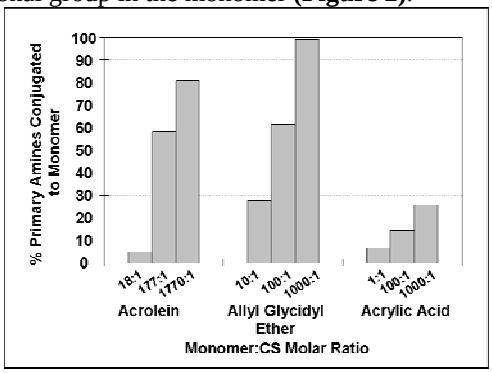

Figure 2: Change in primary amine content, as detected by the fluorescamine assay, with the addition of amine reactive monomers

This gives evidence that the terminal PA of CS will serve as a reasonable site for CS modification for subsequent bottle brush synthesis.

C. CS functionalized surfaces.

Utilizing the terminal PA detected in CS, CS chains were attached to functionalized glass surfaces. From EDAX chemical analysis sulfur was detected on CS immobilized glass slides and normalized to Si content. EDAX data indicates an overall increase in surface sulfur content, and thereby surface CS content on aldehyde and epoxide functionalized slides **(Figure 3)**.

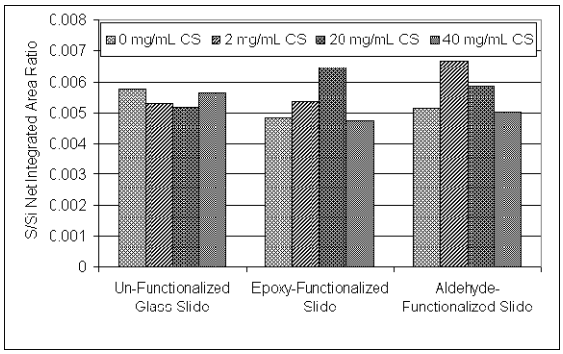

Figure 3: EDAX analysis of functionalized glass surfaces modified with varying concentrations of CS.

Attachment of CS to epoxide surfaces was also observed via contact angle where contact angle on epoxide slides incubated in 2mg/mL CS was 50% of that detected on control epoxide slides (0mg/mL CS) indicating an increase in surface hydrophilicity imparted by covalently bound CS chains.

VI. Conclusions

In this study, we have identified a terminal functional group in commercially available CS that may be used as a handle for the attachment of CS bristles to polymeric backbones or functionalized surfaces. The ability to utilize CS in these structures will allow for the fabrication of a family of biomimetic macromolecules for the replacement of aggrecan in the degenerated NP of the IVD, thereby restoring hydration and mechanical function to the tissue.

Acknowledgements

We would like to acknowledge The Drexel University Materials Characterization Facility, especially Dee Breger for assistance with EDAX analysis.

References

[1] Urban J. P. G. SR. Degeneration of the Intervertebral Disc. Arthritis Res Ther. 2003;5:120-30.

[2] Seog J, Dean D, Plaas AHK, Wong-Palms S, Grodzinsky AJ, Ortiz C. Direct measurement of glycosaminoglycan intermolecular interactions via high-resolution force spectroscopy. Macromolecules. 2002;35(14):5601-15.

[3] Anderson B, Hoffman P, Meyer K. The O-Serine Linkage in Peptides of Chondroitin 4- or 6-Sulfate. Journal of Biological Chemistry. 1965;240(1):156-67.

[4] Volpi N. Chondroitin sulfate: structure, role and pharmacological activity: Academic Press; 2006.

[5] Lauder RM. Chondroitin sulphate: A complex molecule with potential impacts on a wide range of biological systems. Complementary Therapies in Medicine. 2009;17(1):56-62.

Engineering Nanofibers for a Novel Intradermal Vaccination Method for Whooping Cough

Alan Shteyman, K.M. Sawicka, S.R. Simon
Stony Brook University
Basic Science Tower 9-148
Stony Brook, NY 11794-8691

Abstract - **Current delivery systems for vaccines present major logistical problems when large populations need to be vaccinated within a short time period, such as in the case of a pandemic. An efficient and effective method for pandemic vaccination is the driving force of the research performed by our group. The proposed alternative vaccination technique consists of a self-administrable patch made of electrospun nanofibers, where antigens and adjuvants are imbedded during the electrospinning process. This allows large quantities of immunogens to be encapsulated within the nanofibrous mat. This abstract describes the use of the electrospinning technique for the development of a new intradermal delivery system for biologically functional pertussis toxin (PT) to effectively vaccinate against whooping cough. The functional PT was immobilized within highly hygroscopic polyvinyl pyrrolidone (PVP) nanofibers. To establish the efficiency of the technique to immobilize biologically functional PT, prepared patches were incubated with Chinese Hamster Ovary (CHO, K1) cells. The cellular assay measures the degree of clumping of the natively attached CHO cells upon exposure to biologically functional PT. The simultaneous incubation of diluted stock and electrospun PT allowed for a direct comparison of functional PT concentration. This study has reproducibly demonstrated that approximately 80% of the total PT added to the polymer solution was successfully incorporated into the electrospun mat, and maintained biological functionality.**

I. Introduction

The whooping cough inoculation is one of the oldest, currently administered vaccines with an abundance of relevant information. The recent resurgence of the disease within the United States points to the suboptimal efficacy of the available vaccine to protect against new strains of the causative agent Bordetella Pertussis [1]. The traditional vaccine for pertussis consists of inactivated components of the bacterium, and is normally administered as an intramuscular injection mixed with vaccines for Tetanus and Diphtheria [1].

The traditionally employed method of vaccination presents logistical predicaments particularly in pandemic situations. The utility of hypodermic needles requires administration by trained personnel as well as a proper hazardous waste disposal. The proposed vaccine system would overcome the named impediments through the use of a self administrable vaccine patch.

The skin patches would effectively utilize the high population of antigen presenting cells (APCs), such as Langerhans cells, within the human skin to evoke antigen specific protection against pandemic threats. This study examined the efficacy of a nanofibrous patch to encapsulate and retain biologically functional PT under various process conditions for an intradermal whooping cough vaccine.

II. Materials and Methods

A. Electrospinning PT experiments

The electrospinning method used to produce the nanofibrous membranes involves the use of an electric field of 1.5 kV/cm to overcome the surface tension of the PT/PVP solution droplet formed at the tip of the needle to result in jet formation [3]. The likely charged jet undergoes further splitting; the solvent evaporates mid air ensuring a solid nanofibrous membrane collected on the grounded collector.

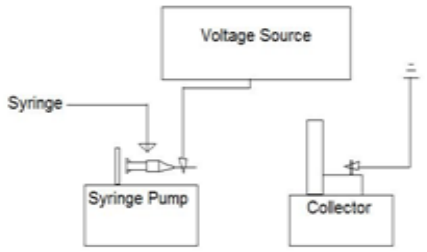

Fig. 1 A diagram of the electrospinning apparatus.

The electrospinning solution consisted of a base solution of 0.05 mM PVP (Sigma Aldrich, St. Louis, MO) in 75% ethanol and 25% phosphate buffered saline (PBS), mixed with 2.5 ng/µL PT (List Biological Laboratories) in PBS at a 7:3 volume ratio was prepared. The voltage was maintained at 15 kV and the distance between the syringe and the collector was 10 cm. Temperature and humidity was kept at ambient conditions. The employed flow rates were 10.0 µL/min, 15.0 µL/min or 20.0 µL/min. The solution flow rate variation has been examined to establish optimal process parameters for PT encapsulation and membrane morphology. To obtain the desired concentration range the collected mats were dissolved in 10.0 ml of PBS and frozen until CHO cell assay was performed.

B. Scanning Electron Microscopy

A representative piece of each PT/PVP membrane was examined with Scanning Electron Microscopy (SEM) to analyze the average nanofiber diameter, and the morphology obtained through the variations of the electrospinning process.

C. CHO Assay

The CHO cell assay consists of CHO-K1 cells grown in media composed of RPMI 1640 with 2.05mM L-Glutamine, 5% Fetal Bovine Serum and 1% Penicillin/Streptomycin. The CHO cells were seeded at a concentration of 2.7×10^4 cells/cm^2 into a 96-well cell culture plate, and incubated for 24 hours to allow the formation of a monolayer of attached CHO cells. Consequently the growth media was dumped, and the cells are dosed with a dilutions of stock solution, as well as serial dilutions of the dissolved electrospun mat. The test of biological functionality of the dosed PT is established through qualitative analysis of the amount of clumping the cells exhibit in response to the PT. The simultaneous incubation of stock and electrospun material allows for estimation of PT concentration within the experimental samples.

III. Results

The SEM examination of the electrospun PT/PVP nanofibrous mats resembled the beads-on-a-string morphology characteristic of aqueous solvents utilized for PT stability. The flow rate variation changed the size of the droplet formed at the tip of the needle affected by the electric field, and therefore effected the formation of "beads" along the fibers.

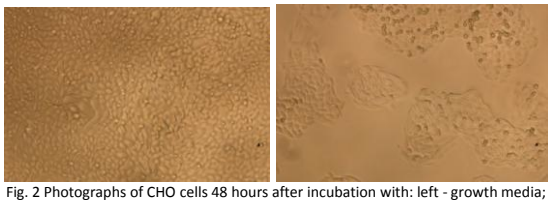

Fig. 2 Photographs of CHO cells 48 hours after incubation with: left - growth media; right - with 0.05 ng PT/ml (rated "3").

The functionality studies have established the successful retention of biological function of PT throughout the electrospinning process. The qualitative analysis of the characteristic clumping observed in the presence of functional PT as depicted in figure 2 was comparable to stock PT controls. The direct comparison to known concentration standards allowed to estimate that approximately 80% of the total toxin added to the electrospinning solution was retained within the electrospun membrane.

IV. Conclusion

The reversible packaging of pertussis toxin within polymeric nanofibers has been explored in this study as an alternative whooping cough vaccine. The variation of process parameters has been shown to have an effect of the obtained morphology and the efficacy of protein incorporation within the matrix. The retention of biological functionality of the protein throughout the process of electrospinning process encourages further exploration of the technique for development of an innovative, self-administrable, intradermal pandemic vaccine.

References

[1] Centers for disease Control, Epidemiology and Prevention of Vaccine-Preventable Diseases, Public Health Foundation, 2009.

[2] S. Babiuk, M. Baca-Estrada, L. A. Babiuk, C. Ewen, M. Foldvari, "Cutaneous vaccinated ation: the skin as an immunologically active tissue and the challenge of antigen delivery," J. Contr. Release. Vol. 66, Issue 2-3, pp. 199-214, 15 May 2000.

[3] C. S. Kong, W. S. YOO, N. G. JO, H. S. KIM, "Electrospinning mechanism for producing nanoscale polymer fibers," J. Macromolecular Sci. Part B: Physics. Vol. 49, pp. 122-131, 2010.

[4] G.M. Glenn, D.N. Taylor, X. Li, S. Frankel, A. Montemarano, and C.R. Alving, "Transcutaneous immunization: A human vaccine delivery strategy using a patch," *Nature Medicine*, vol. 6(12), pp. 1403-6, 2000.

[5] K.M. Sawicka, P. Gouma, "Electrospun composite nanofibers for functional applications," *J. Nanoparticle Research*, vol.8, pp. 769- 781, 2006

Differences in Mechanical Properties between Human and Porcine Aortic Root

Caitlin Martin, Thuy Pham, Wei Sun
Tissue Mechanics Lab
Biomedical Engineering and Mechanical Engineering
University of Connecticut
Storrs, CT

Abstract*— Recently, percutaneous aortic valve (PAV) replacement has been investigated as an endovascular alternative for the treatment of aortic stenosis. Percutaneous valve intervention requires a thorough material characterization of the human aortic root and ascending aorta for successful PAV deployment and function. Recent PAV clinical trials have been conducted on animal models under the assumption that animal tissues are closely related to human (1, 2). However, various adverse effects detected after device implantation such as device fracture, myocardial infarction, peripheral embolism, aortic injury, perivalvular leak and access site injury have been reported (3, 4). We hypothesize that the biomechanical interaction between the device and the host tissue plays an important role that determines the efficacy of the PAV treatment. Thus, there is a need obtaining the mechanical properties of the host tissues for the future analysis of device-tissue interaction. In this study, we characterized the mechanical properties of aged human aortic tissues and compared them to porcine tissues to determine whether animal studies are appropriate for the PAV trials. Our results suggest there are significant differences between porcine and human aortic tissues and the efficacy of animal models for PAV simulation should be further investigated.

I. INTRODUCTION

Aortic stenosis is the most common valvular heart disease and its prevalence is growing with an aging population (*5*). The current treatment, aortic valve replacement and cardiopulmonary bypass, involves open-chest surgery, which holds significant risks for patients with advanced age and/or co-morbidities. Recently, percutaneous aortic valve (PAV) replacement devices have been investigated to provide a less invasive endovascular approach for the treatment of stenosis.

Although the PAV technique holds promise, it remains in its infancy. For, instance, PAV deployment relies on the tissue-stent interaction in order for the device to hold its position for long-term function. Excessive radial force of the stent may cause aortic injury, while insufficient forces will lead to paravalvular leakage or device migration. Therefore, this technique requires a thorough biomechanical characterization of the elastic properties of the human aortic root and ascending aorta.

Recent studies focused on the mechanical properties of the aortic root have been based under the assumption that porcine tissue properties are comparable to human (*1*). The mechanical properties of the human aortic tissues are still largely unknown. The goal of this study is to measure the biaxial mechanical properties of the aged human aortic sinuses and ascending aorta. This data will be used to determine regional differences in mechanical properties within the human aortic root, as well as the relationships between human and porcine tissues. This study may provide insight for the biomechanics involved in the PAV intervention, and for the efficacy of porcine models for predicting successful PAV deployment and function in the aged human.

II. MATERIALS & METHODS

Biaxial test samples from the ascending aorta (22.43±5.00mm) and three aortic sinuses (14.74±2.09mm) were dissected from seven fresh frozen human hearts and five porcine hearts. A summary of the human patient characteristics is listed in Table 1.

Table 1. Human Patient Characteristics

Heart	**1**	**2**	**3**	**4**	**5**	**6**	**7**
Age	88	96	95	98	87	82	95
Sex	F	F	F	F	F	M	M
Cause of Death	Alz	CPA	RA	RA	unk	AP	NC
Primary Disease	CAD	n	n	n	PKD	n	n
Risk Factors							
Diabetes	unk	n	n	y	n	n	n
GERD	y	n	n	n	n	n	n
Pneumonia	n	n	y	n	n	y	n
Dementia	n	n	n	n	y	n	n
Atherosclerosis							
Coronary	y	n	n	n	n	n	n

Alzheimer's = Alz, CA = cardiac arrest, CAD = Coronary artery disease, CPA = Chronic pulmonary aspergillosis, GERD = Gastroesophogeal reflux disease, NC = natural causes (old age), RA = respiratory arrest, PKD = Polycystuc Kidney Disease, ukn =unknown

Planar Biaxial Testing

Biaxial testing was carried out according to the methods presented in Sacks and Sun (*6*). Stress-controlled test protocols were utilized where the ratio of the normal Lagrangian stress components T_{11}:T_{22} was kept constant with T_{12}=T_{21}=0. Twenty continuous cycles of preconditioning were performed to reduce tissue hysteresis. Each sample was tested at the maximum load possible without causing tissue damage. At the maximum load seven consecutive stress protocols at ratios T_{11}:T_{22}=0.75:1, 0.5:1, 0.3:1, 1:1, 1:0.75, 1:0.5, 1:0.3 were conducted.

Data Analysis

In order to compare the mechanical properties of human to porcine tissue, the stiffness of each specimen was measured as the secant modulus between 0 and 60kPa for

circumferential and longitudinal anatomical directions. Due to small sample size, human tissue stiffness was further compared to porcine tissue stiffness determined from the biaxial data published by Gundiah *et al.* in (*7*).

Statistical Analysis

Independent Student's t-tests were utilized to compare the mean stiffness of human ascending aorta and aortic sinus specimens to the stiffness of the corresponding porcine tissue in both the circumferential and longitudinal directions. A p-value <0.05 was considered to be statistically significant.

III. RESULTS/DISCUSSION

Mechanical Testing

In our experiment, we observed distinct differences in the stress-strain relationships between the human and porcine tissues, which are shown in Fig. 1. All human specimens were much stiffer than the corresponding porcine tissues. At 60kPa the strain range of the porcine aortic sinus is 0.310±0.127 which is over 3.5 times greater than the human aortic sinus strain range of 0.088±0.0382. At 60kPa the porcine ascending aorta strain range of 0.435±0.233 is also greater than that of the human tissue (0.095±0.0354) by over 4 times.

There were also marked differences in the shapes of the stress-strain response curves, also see Fig. 1. The human tissues exhibited a pronounced 'toe-region' characteristic of soft biological tissues, while the porcine tissues behave nearly linearly at low stress ranges.

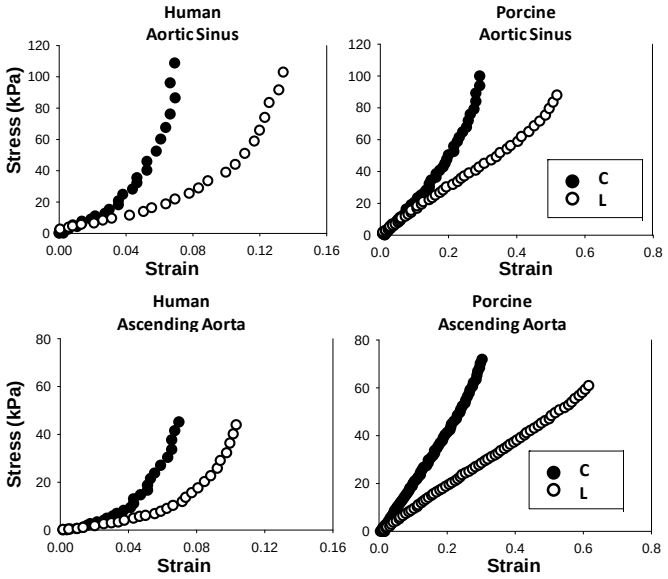

Figure 1. (Left) Human aortic sinus ascending aorta stress-strain curves in circumferential (c) direction (black dots) and longitudinal (l) direction denoted (white dots).

Significant differences (p<0.001) were also found between the stiffness of human ascending aorta and aortic sinus to the porcine specimens tested by Gundiah *et al*. in both the circumferential and longitudinal directions (See Fig. 2).

Higher stiffness of human aortic tissues might be accounted for by several factors. One factor is the advanced age of the patients selected in this study. Tissue stiffness increases with age due to an increase in collagen and elastin content (*8*). The human specimens were all elderly to provide a better representation of the average patient suffering from aortic stenosis. However, the differences in the shape of the stress-strain curves between the human and porcine tissues suggest that the two may not be analogous at all.

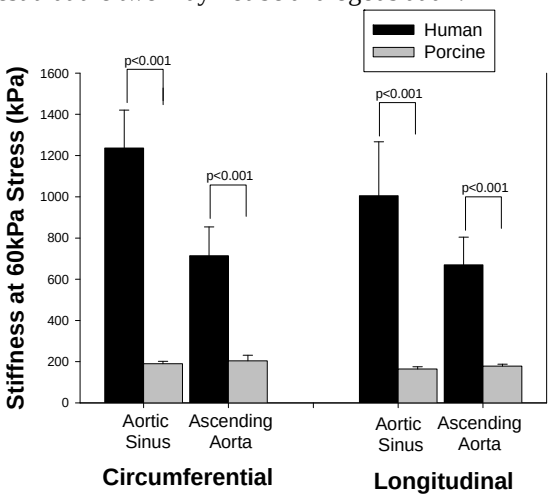

Figure 2. Stiffness of our human data and Gundiah *et al.*'s porcine data (*7*) of the ascending aorta and aortic sinuses at a stress of 60kPa.

Another factor to consider for the vast differences in mechanical properties is calcification. For many patients, stenosis is associated with calcium deposits along the aortic valve (*9*). In several of the human aortic specimens tested in this study, crystalline calcium deposits were found along the edges of the aortic sinuses and leaflets. Although the belly of the sinus, where it was subjected to biaxial test, did not exhibit calcification, it may be an indication of changes in mechanical properties of the entire aortic root. There was no calcification evident in any of the porcine tissues.

This study was limited by small sample size due to limited tissue supply. A future study will include a larger sample size, and constitutive modeling to further characterize the material properties of aortic tissues.

In conclusion, we observed clear differences in the mechanical properties of aged human and porcine aortic tissues. Such findings are important for quantifying the mechanical properties of aortic tissues needed for the PAV intervention and for the consideration of animal studies in the PAV clinical trials.

IV. REFERENCES

1. M. Ferrari *et al.*, *Heart* **90**, 1326 (2004).
2. J. Liddicoat, R. *et al.*, *Catheterization and Cardiovascular Interventions* **60**, 410 (2003).
3. J. G. Webb *et al.*, *Circulation* **116**, 755 (2007).
4. E. Grube *et al.*, *Circulation* **114**, 1616 (2006).
5. B. Iung, A. Vahanian, *The Lancet* **368**, 969 (2006/9/22/, 2006).
6. M. S. Sacks, W. Sun, *Annual Review of Biomedical Engineering* **5**, 251 (2003).
7. N. Gundiah *et al.*, *The Journal of heart valve disease* **17**, 606 (2008).
8. R. B. Hickler, *Clin. Cardiol.* **13**, 317 (1990).
9. V. Khetarpal *et al.*, *Journal of the Neurological Sciences* **287**, 32 (2009).

Bioactive, Semi-degradable Hydrogels for Cartilage Tissue Engineering

K.L. Spiller, Y. Liu, W. Liu, Y. Cao, A.M. Lowman
Drexel University
3141 Chestnut St.
Philadelphia, PA 19104

***Abstract*—Poly(vinyl-alcohol) (PVA) hydrogels have long been investigated as replacement materials for articular cartilage, but their lack of bioactivity has impeded their utility. We have prepared bioactive PVA hydrogels by incorporating a degradable phase of poly(lactic-co-glycolic acid) (PLGA) that enhances porosity and controls the release of growth factors. Hydrogel properties such as porosity, pore size, and degradability were dependent on the hydrogel composition and fabrication conditions. Porosity and pore size increased over time in physiological conditions as the PLGA phase degraded within the nondegradable PVA hydrogels. Cell-seeding efficiency and tissue formation *in vitro* were proportional to the amount of PLGA. When insulin-like growth factor-1 (IGF-1) was incorporated into the degradable PLGA phase, release was controlled over 6 weeks, with no burst effect. Hydrogels containing a low or high dose of IGF-1 were wrapped in PGA fibers, seeded with chondrocytes and implanted subcutaneously into nude mice. After 6 weeks, the amount of cartilage tissue formation and integration with the hydrogels were higher compared to controls without IGF-1, although there were no differences in mass, proteoglycan content or compressive modulus between hydrogels with low and doses of IGF-1. These simple modifications to PVA hydrogels may finally make them suitable as cartilage replacements.**

I. Introduction

Poly(vinyl alcohol) (PVA) hydrogels have long been investigated as materials to replace damaged articular cartilage because of their similar water contents and mechanical properties. However, their hydrophilic nature prevents cell adhesion and protein adsorption, so implanted PVA hydrogels fail to integrate with surrounding cartilage [1]. Degradable scaffolds of poly(lactic acid) (PLA), poly(glycolic acid) (PGA), and their copolymers (PLGA) have been widely used as tissue engineering scaffolds. Engineered cartilage grown on PGA fiber scaffolds integrated well with surrounding cartilage upon implantation into osteochondral defects, but their mechanical properties were far from sufficient to withstand loads found in the knee [2]. We sought to combine the advantages of PVA hydrogels and PGA scaffolds while diminishing their disadvantages. By blending PLGA solutions with hydrogel solutions prior to physically crosslinking, a degradable phase of PLGA microparticles was dispersed throughout a highly porous PVA hydrogel network. We characterized the effects of PLGA content on the hydrogel microstructure and on chondrocyte proliferation *in vitro*. We then incorporated insulin-like growth factor-1 (IGF-1), an important growth factor in normal cartilage development and repair, into the PLGA microparticles, and examined the effects on cartilage tissue formation *in vivo* in a nude mouse model.

II. Materials and Methods

A. Hydrogel fabrication and characterization

Superporous hydrogels with degradable phases of 0, 20, 30, 40 and 60wt% PLGA with respect to the nondegradable phase of PVA were created through a modified double emulsion technique. A primary emulsion of phosphate buffered saline (PBS) and PLGA dissolved in dichloromethane (DCM) was added to a 10wt% solution of PVA and 0.1wt% poly(vinyl pyrrolidone) for added stability, and stirred for 30 minutes before freezing in an acetone/dry ice bath. The volumes of DCM used were 10vol% for the hydrogels prepared without PLGA and 35vol% for the hydrogels prepared with PLGA. This double emulsion was then subjected to 6 cycles of freezing for 21hrs and thawing for 3hrs, creating a physically crosslinked hydrogel network around the organic phase. The resultant PLGA-PVA hydrogels were then dehydrated through an ethanol series and dried by critical point drying to retain their shape. Hydrogels containing IGF-1 were prepared with 60w% PLGA and 35v% DCM, as above except the internal aqueous phase was a solution of IGF-1 (low dose, 33μg, and high dose, 27μg, per gram dry scaffold) in 10mM acetic acid and 0.1% BSA.

The microstructures of the hydrogels were analyzed after 0, 4 and 7 weeks of swelling in PBS. The porous networks were imaged using environmental scanning electron microscopy (ESEM), so that hydrogels could be viewed in their hydrated state. Dry samples were analyzed using micro-computed tomography (μCT) (Skyscan 1172, Belgium), and reconstructed 3-D models were used to determine values of porosity and pore size, using CTAn software.

*B. Chondrocyte proliferation i*n vitro

Hydrogels containing 0, 30, and 60w% PLGA were seeded with 5 million chondrocytes isolated from the femoral condyles of calves and cultured *in vitro* for 7 weeks. Samples were fixed in 4% paraformaldehyde, immersed in 30% sucrose, sectioned to 25um on a cryostat, and stained using hematoxylin and Safranin'O.

C. Controlled release of IGF-1 in vivo

Hydrogels containing insulin, used as a model for IGF-1, were immersed in PBS for 6 weeks, and samples of the release

media were periodically measured using high performance liquid chromatography. Hydrogels containing no, low, or high doses of IGF-1 were wrapped in PGA fibers to increase the area available for cell seeding, seeded with 10 million chondrocytes isolated from the femoral condyles of immature pigs, and implanted subcutaneously in nude mice. After 6 weeks, the hydrogels were removed and analyzed histologically and mechanically in uniaxial compression. The total content of glycosaminoglycans (GAGs) was measured through reaction with dimethylmethylene blue dye.

III. Results and Discussion

The simple addition of PLGA and DCM to PVA hydrogels resulted in PLGA microparticles distributed throughout highly porous networks, a result of the hydrogel solution crosslinking around the organic phase (Fig. 1).

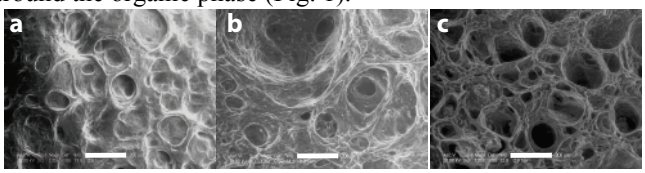

Fig. 1. Representative ESEM images of cross-sections of hydrogels prepared with (a) 0% PLGA and 10v% DCM, (b) 30w% PLGA and 35v% DCM, and (c) 60w% PLGA and 35v% DCM. Scale bars are 200μm.

The porosity, average pore size, equilibrium water content, and mechanical properties of the hydrogels were dependent on the relative amounts of PLGA and DCM added prior to crosslinking, allowing a high degree of control over hydrogel properties. For example, increases in PLGA content cause a decrease in average pore size, and increases in DCM content cause an increase in porosity. The average porosity ranged from 65 to 85% and the average pore size ranged from 60 to 120μm. Both average porosity and pore size increase with time in physiological conditions, as the PLGA degrades within the PVA hydrogels. When chondrocytes were seeded in these porous scaffolds and cultured *in vitro* for 7 weeks, immature cartilage tissue filled the pores. The robustness of proteoglycan staining by Safranin'O was proportional the initial PLGA content, with very few cells and no visible proteoglycans found in hydrogels without PLGA (Fig. 2).

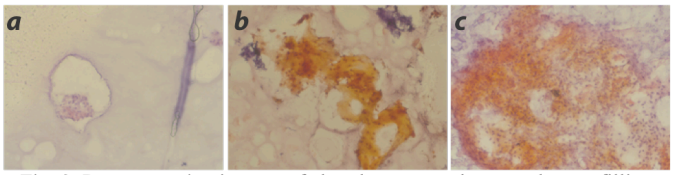

Fig. 2. Representative images of chondrocytes and proteoglycans filling the pores of hydrogels made with initial amounts of PLGA of (a) 0, (b) 30, and (c) 60w%, after 7 weeks in cell culture (Safranin'O and hematoxylin). Original magnification is 200x.

To enhance chondrogenesis within the hydrogels, IGF-1 was incorporated into the PLGA microparticles. The release of insulin, used as a model for IGF-1, was controlled over 7 weeks, with no burst effect, and depended on the degradation of PLGA (Fig. 3).

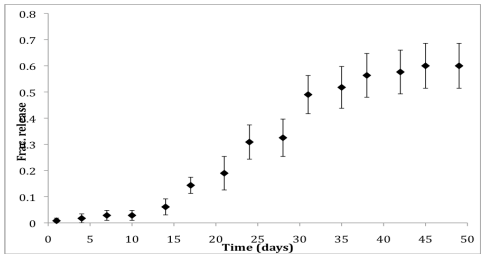

Fig. 3. Release of insulin, a model for IGF-1, over 7 weeks *in vitro*.

Hydrogels of 60w% PLGA containing no, low, or high doses of IGF-1 were wrapped in PGA fibers, seeded with 10 million chondrocytes, and implanted subcutaneously in nude mice. In this way, the effects of controlled release of IGF-1 on chondrogenesis could be examined separately from the effects of the hydrogel structure. A layer of cartilage formed in the PGA fibers surrounding the hydrogel. The layers were thicker for hydrogels containing IGF-1 than those without, but there was no difference resulting from an increase from the low to high dose (Fig. 4). Pockets of ossification were seen on all samples, and may be a result of some osteocytes contaminating the initial cell population. These results were confirmed histologically. The total GAG content and compressive modulus of the constructs were higher for those with IGF-1 than those wihtout, though there were no differences between low and high doses (Table 1).

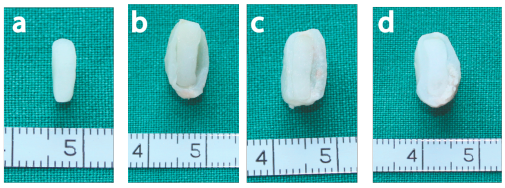

Fig. 4. Gross view of cartilage-hydrogel constructs for hydrogels (a) without chondrocytes, (b) with chondrocytes but no IGF-1, and with chondrocytes and with (c) low and (d) high doses of IGF-1.

TABLE 1
PROPERTIES OF HYDROGEL-CARTILAGE CONSTRUCTS.

Dose of IGF1	Total GAGs (mg)	Compressive modulus (kPa)
High	10.5±1.93	169.5±40.11
Low	9.89±2.24	200.5±120.0
None	8.63±1.68	71.25±23.44
No cell control	0.19±0.03	39.58±27.42

In conclusion, the simple addition of PLGA to PVA hydrogels through a novel double emulsion technique results in an interspersed phase of degradable microparticles, a highly porous structure, and the ability to encapsulate and control the release of growth factors. These hydrogels retain the desirable mechanical and swelling properties of PVA hydrogels, but with additional cell adhesiveness and bioactivity. This technology may finally allow the use of PVA hydrogels as biomaterials to replace damaged cartilage.

IV. References

[1] S. Maher, S. Doty, P. Torzilli, S. Thornton, A. Lowman, J. Thomas, et al., "Nondegradable hydrogels for the treatment of focal cartilage defects," *J. Biomed. Mater. Res.,* vol. 83A, pp. 145-155, 2007.

[2 G. Zhou, W. Liu, L. Cui, X. Wang, T. Liu, Y. Cao, "Repair of porcine articular osteochondral defects in non-weightbearing areas with autologous bone marrow stromal cells," *Tissue Engineering*, vol. 12, pp. 3209-3220, 2006.

Bioengineering a Complex 3D Human Breast Tissue Culture System on Silk Scaffolds

Xiuli Wang[a], Carlos Sonnenschein[b], David L Kaplan[a,b]
[a]Tufts University, 4 Colby Street, Medford, MA 02155
[b]Tufts University School of Medicine, 136 Harrison Ave, Boston, MA 02111

***Abstract*-Epithelial-stromal interactions play a crucial role in normal embryonic development and carcinogenesis of the human breast while the underlying mechanisms of these events remain poorly understood. Here, we constructed a physiologically relevant, 3D culture surrogate of complex human breast tissue that included a tri-culture system made up of human mammary epithelial cells (MCF10A), fibroblasts and adipocytes in a Matrigel™/collagen mixture on porous silk scaffolds. The presence of stromal cells inhibited MCF10A proliferation and induced both alveolar and ductal morphogenesis and enhanced casein expression. Only alveolar structures with reverted polarity were observed in MCF10A monocultures. In contrast to the immature polarity exhibited by co-cultures with either fibroblasts or adipocytes, the alveolar structures formed by the tri-cultures exhibited proper polarity similar to that observed in breast tissue. Furthermore, consistent with their phenotypic appearance, more functional differentiation of epithelial cells was also observed in the tri-cultures, where casein α and β- mRNA expression was significantly increased. This *in vitro* tri-culture system sustained on silk scaffold effectively represents a more physiologically relevant 3D microenvironment for mammary epithelial cells and stromal cells than either co-cultures or monocultures. This experimental model provides an important first step for bioengineering an informative human breast tissue system.**

INTRODUCTION

Breast cancer is the second leading cause of cancer-related death for women in the United States [1,2]. Thus, it's essential to develop appropriate and functionally relevant, sustainable human breast tissue model systems to advance our understanding of how cells of all types sense signals in a 3D microenvironment and how these signals are processed to influence mammary gland morphogenesis and carcinogenesis.

Currently, heterotypic co-cultures of epithelium are available, for the study of cell-cell and cell-ECM interactions. However a lack of more complex and sustainable models involving more than two cell types still persists. This is important, as increasing evidences have shown the critical role played by the microenvironment in establishing normal mammary tissue architecture and its aberrant behavior in the progression of cancer. On the other side, although hydrogel systems have been utilized in 3D culture, a further optimized culture system is still in need due to their limitations in mechanical property and degradation. Thus, based on our previous studies on silk protein [3,4], here, we hypothesizes that slow degrading silk scaffolds with appropriate cells-ECM/stroma will provide a rational approach to construct a more physiologically relevant, sustainable normal or diseased 3D human breast tissue *in vitro*.

MATERIALS AND METHODS

In tri-culture, MCF10A cells, fibroblasts (HMF) and pre-differentiated hASCs were mixed with the (GFR)-Matrigel™-collagen type I solution (1:1, 1.0 mg/ml collagen) and seeded on the preconditioned silk scaffolds in a 2:1:1 ratio keeping the number of MCF10A constant. Co-cultures and monocultures of MCF10A in the same conditions served as controls. To distinguish different cell types within the tri-cultures or co-cultures, CellTracker™ DiI and Green CMFDA were applied to label MCF10A and stromal cells. Morphologic development and functionality of the constructs were characterized by their growth profile, marker proteinsand genes expression level assayed by viability staining, immuno-staining as well as real-time RT-PCR. Statistical differences were determined by *Student's two-tailed t test* [5].

RESULTS AND DISCUSSION

To characterize the 3D tri-culture model *in vitro*, we first evaluated the influence of stromal cells on the proliferation of epithelial cells. A synergistic inhibitory effect of fibroblasts and pre-differentiated hASCs was observed in the 3D tri-culture group, as shown by a lower percentage of Ki67 positive staining MCF10A cells when compared with either the monoculture or the co-culture groups (data not provided).

Both alveolar and duct-like structures were generated in the tri-culture and co-cultures; in contrast, only alveolar structures were observed in MCF10A monoculture (Fig.1). These results indicate that stromal cells promote ductal morphogenesis by epithelial cells.

Cell polarization is an important parameter to evaluate an experimental epithelial model *in vitro* [6]. Besides the effect on ductal morphogenesis, a more "mature" polarity was exclusively observed in the tri-cultures, where the expression pattern of sialomucin and GM130 mimicked the breast tissue *in vivo*, when compared with the "immature" polarity exhibited by the co-cultures and the inside-out polarity observed in the monoculture of MCF10A (Fig.2). This result indicates that either fibroblasts or pre-differentiated hASCs contribute to the appropriate polarity of MCF10A cells in 3D

co-culture systems; moreover, once they were incorporated within a same 3-D system, a synergistic effect on the extent of the epithelium polarization was generated.

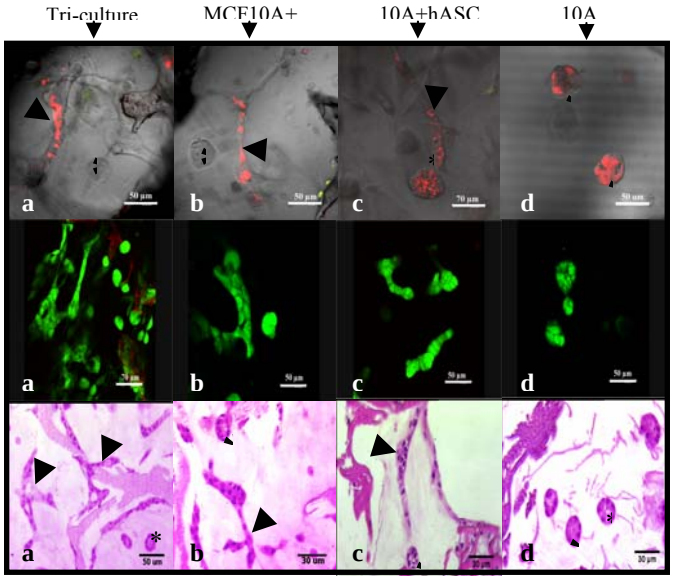

Fig. 1. Growth profile and viability of MCF10A cells in different cultures developed on silk scaffolds. CLSM images showed both alveolar and duct-like structures formed in co-cultures (Top row, $\mathbf{a_1}$-$\mathbf{c_1}$), while only alveolar structures were observed in the monocultures ($\mathbf{d_1}$). Viability of MCF10A in different groups was detected by viability staining (middle row, $\mathbf{a_2}$-$\mathbf{d_2}$)). H&E staining showed morphological characteristics of the epithelial structures formed by MCF10Ain different groups (bottom row, $\mathbf{a_3}$-$\mathbf{d_3}$). (Arrowhead notes duct-like structure).

Consistent with the more differentiated phenotype exhibited by epithelial cells in tri-culture, a higher expression of casein transcripts was also induced in the tri-cultured MCF10A cells when compared with those cultures under co-culture or monoculture conditions (Fig.3). This highlights the critical role of stromal cells in regulating the functionality of mammary epithelial cells. In addition, a synergistic effect of the stromal cells on the functionality of epithelial cells was also observed, as evidenced by the fact that b-casein gene expression was exclusively detected in the tri-culture group. This synergistic effect might in part be explained by the unique microenvironment constructed by more than one type of stromal cell, as well as the epithelial cells embedded within the ECM on the 3D silk scaffolds [7].

CONCLUSIONS

A complex 3D human tissue culture system was described in which human breast epithelial cells were cultured with two types of predominant mammary stromal cells on silk scaffolds and displayed more differentiated morphological phenotype and functional activity. This *in vitro* tri-culture model can be utilized to address several important issues in breast biology, including the role of cell-cell and cell-substrate interactions in regulating the response of breast epithelium to ovarian hormones, the induction of specific protein synthesis, as well as neoplastic transformation.

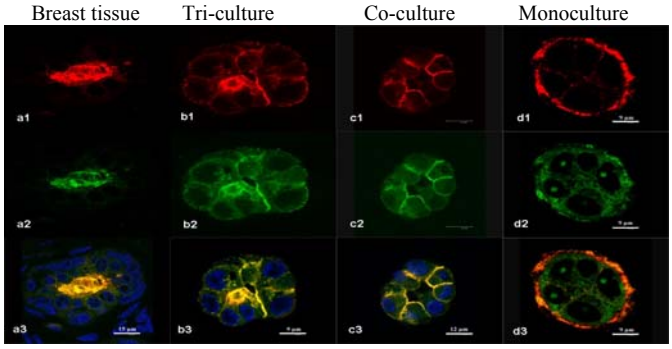

Fig.2. Immunostaining with sialomucin (red) and GM130 (green) showed the polarity of the alveolar structures formed by tri-cultured MCF10A cells on silk scaffold ($\mathbf{b_1}$-$\mathbf{b_3}$, day 6), which is similar to the positive control of human native breast tissue ($\mathbf{a_1}$-$\mathbf{a_3}$) in comparison to the co-cultures ($\mathbf{c_1}$-$\mathbf{c_3}$, $\mathbf{d_1}$-$\mathbf{d_3}$). The cell nucleus was counter-stained by DAPI (blue). Reversed polarity was also observed in the monoculture ($\mathbf{e_1}$-$\mathbf{e_3}$, day 6).

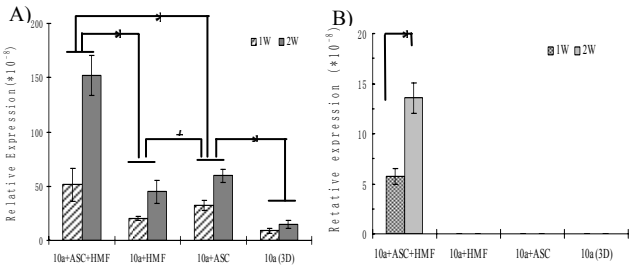

Fig. 3 Transcript expression levels of a-casein (A) and b-casein (B) by real-time RT-PCR at the indicated time points. A significant increase in the expression of both α and β-casein was detected in MCF10A cells with both stromal cells. ($n=3$, $^{*}p < 0.05$, $^{\#}p > 0.05$).

ACKNOWLEDGEMENT

This work was supported by Phillip Morris International (CS) and the NIH P41 (EB002520) Tissue Engineering Resource Center (TERC). We thank Prof. Jeff Gimble, Pennington Research Center, for the contribution of the hASCs.

REFERENCES

[1] C. Mettlin, "Global breast cancer mortality statistics." CA Cancer J Clin, 1999, vol.49, pp.138–144.

[2] A. Thomsen, J.M. Kolesar, "Chemoprevention of breast cancer," Am J Health Syst Pharm, 2008, vol.65, pp.2221-2228.

[3] Y. Wang, H.J. Kim, G. Vunjak-Novakovic, D.L. Kaplan, "Stem cell-based tissue engineering with silk biomaterials," Biomaterials, 2006, vol.27, pp.6064-6082.

[4] S. Hofmann, S. Knecht, R. Langer, et al, "Cartilage-like tissue engineering using silk scaffolds and mesenchymal stem cells," Tissue Eng, 2006, vol.12, pp.2729-2738.

[5] X.L. Wang, X.H. Zhang, L. Sun, B. Subramanian, et al, " Preadipocytes stimulate ductal morphogenesis and functional differentiation of human mammary epithelial cells in 3D silk scaffolds." Tissue Eng Part A, 2009, vol.15, pp.3087-3098.

[6] M.J. Paszek, V.M. Weaver, "The tension mounts: Mechanics meets morphogenesis and malignancy," J of Mammary gland Biology and Neoplasia, 2004, vol.9, pp.325-342.

[7] Schmidhauser, M.J. Bissell , Myers CA, G.F. Casperson, "Extracellular matrix and hormones transcriptionally regulate bovine 18-casein 5' sequences in stably transfected mouse mammary cells," Proc. Natl. Acad. Sci,1990,vol.87, pp.118-122.

Characterization of HA/βTCP 3-D Printed Scaffolds for Custom Bone Repair Applications

L. Witek[1], A. Murriky[1], E. Clark[1], J. Smay[2], M. Pines[1], N. Silva[1], and J.L. Ricci[1]

[1]New York University College of Dentistry
345 East 24th Street, Room 804S
New York, NY 10010
[2]Oklahoma State University
School of Chemical Engineering
423 Engineering North
Stillwater, OK 74078

***Abstract* – To evaluate scaffolds used for bone repair, composed of HA/β-TCP, *in vitro* and *in vivo*. Chemical and mechanical characterization was performed on the bulk material while the *in vivo* portion was utilized to study host response to the scaffold.**

I. INTRODUCTION

To examine the physical, chemical, and *in vivo* properties of biphasic hydroxyapatite (HA) / beta tri-calcium phosphate (βTCP) composite scaffolds, for custom replacement of bone structures *in vivo*. Basic ceramic structures (rods) as well as 3D-printed (direct-write) scaffolds were fabricated for mechanical/chemical testing, *in vitro* studies, and animal studies using a rabbit trephine defect model. The *in vivo* study was used to examine bone and soft tissue response to the scaffolds. The scaffolds used were either empty, filled with calcium sulfate (CS), or chitsosan (CH). The physical and chemical properties will help determine the ideal scaffold configuration for specific bone applications (ie;.craniofacial versus orthopaedic).

II. METHODS

A 15/85% HA/βTCP mixture was used to create rods, which were fired at 1100°C. These rods with dimensions of 18mm in length and 4.1mm diameter were mechanically tested using a modified 3-point bend method (n=12) to determine the load to failure and load versus displacement plot. Also rods were sectioned to have dimensions of 4.1mm in length and 4.1 mm diameter, to undergo diametral-compression testing (n=12) for tensile stress. In addition to mechanical testing, *in vitro* dissolution and chemical characterization studies were performed to examine mass loss and the crystal size and consistency of the HA/βTCP material before and after firing. Direct write (DW) technology was used to 3-D print lattice scaffolds composed of the same material. These had 270μm strut elements (after firing), and regions with different strut spacings (and as well as solid barrier layers. They were also subjected to *in vitro*, physical, and chemical analysis, and were implanted into bilateral 11mm diameter trephine defects in 24 White New Zealand rabbits. There were three types of scaffolds tested: empty, CS filled, and CH filled. Most of the animal work was conducted using CS filled scaffolds evaluated at 8 and 16 weeks.

III. RESULTS

3-point bending and compression tests were used to determine the base line properties of the 15/85 HA/βTCP. These HA/βTCP rods had a maximum flexural load of 74.23±17.24 N/mm. This value was used to find the strength of cylindrical rods in three-point flexure, using Equation 1 [1].

$$\sigma = {}^{8PL_0}\!/_{\pi D^3} \qquad (1)$$

The average strength of these rods was 27.44±6.34 MPa. The 3-D scaffolds of the same material failed in compression at 416.82±22.21N. Rods of different dimensions, which underwent compression testing, had a maximum compression load of 210.87±98.35N. Using equation 2, and the maximum compression values results in an average tensile stress of 7.77±3.85MPa.

$$\sigma = {}^{2P}\!/_{\pi Dl} \qquad (2)$$

The *in vitro* mass loss study showed significant mass loss of the empty scaffolds when compared to those of filled with either CS or CH [2]. The *in vivo* study results exhibit significant bone in-growth in the 15/85 HA/βTCP scaffolds filled with CS. Scaffold volume fractions ranged from 44 to 68% depending on scaffold strut spacing. Total volume of new bone formation ranged from 30±6 to 33±8% at 8 weeks, and 41±13 to 48±14% at 16 weeks depending on scaffold volume fraction. Bone formation as a function of available volume ranged from 51±10 to 81±7% at 8 weeks, and 70±14 to 86±13 at 16 weeks. Significant scaffold remodeling was observed at both time periods, and the largest amounts of scaffold remodeling were observed in the 44% volume fraction scaffolds. These lost ~30% of their volume at 16 weeks. Strut

size was reduced from about to 267±8µm to 167±35µm (Figure 1). Statistical analysis will be performed by one-way ANOVA at 95% level significance.

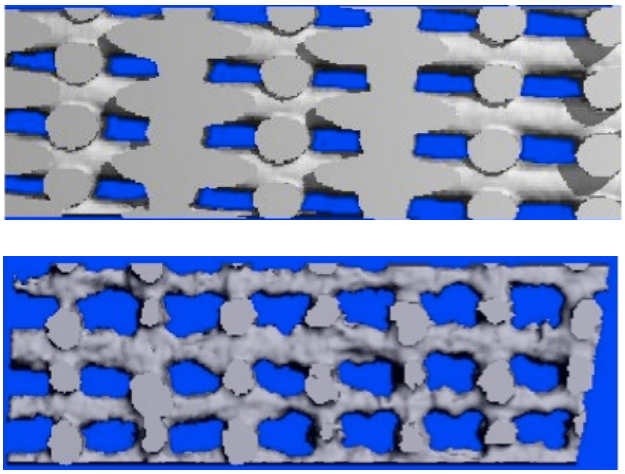

Figure 1: (top) MicroCT image of a 3D reconstructed image of a scaffold pre-implantation. (bottom) A 16-week 15:85 HA/βTCP scaffold (44% volume fraction scaffold) showing extensive osteoclastic erosion of the implanted scaffold

IV. DISCUSSION

The biphasic HA/βTCP ceramic has good initial compressive strength in strut form as well as in 3-D printed form. CS filling enhances mechanical properties and does not impede bone ingrowth as the CS is soluble in vitro and in vivo. Scaffolds with smaller volume fraction (larger pores) show more bone in-growth and remodeling when compared to the smaller pore scaffolds. The smaller pore scaffolds exhibited a lamellar bone in-growth pattern while the larger pore scaffolds showed a trabecular bone pattern. The results suggest that scaffold porosity can be used to control amounts of bone ingrowth and remodeling. This suggests that scaffold design can be used to control the mechanical and bone ingrowth properties, and that scaffolds can be designed for the specific mechanical and temporal requirements needed for different craniofacial and orthopaedic bone repair applications.

REFERENCES

[1]ASTM, 2008, C 1684 – 08
[2]Cretiu-Vasiliu, C., 2008, Masters Thesis, Oklahoma State University, Stillwater, OK.

Injectable Multifunctional Scaffold for Spinal Cord Repair

Lauren Conova[1], Pamela Kubinski [2], Ying Jin[3], Jennifer Vernengo[2], Birgit Neuhuber[3],

Itzhak Fischer[3], Birgit Neuhuber[3], Anthony Lowman[1]

[1]Department of Chemical and Biological Engineering, Drexel University, Philadelphia, PA 19104, [2]Department of Chemical Engineering, Rowan University, Glassboro, NJ 08028, [3]Department of Neurobiology and Anatomy, Drexel University College of Medicine, Philadelphia, PA 19129

Abstract- **Spinal cord injury (SCI) affects thousands of Americans each year. The injury results in local cell loss in the spinal cord, interrupting the connections between brain and periphery. Current treatment options for SCI are limited due to the inability of adult neurons to regenerate in the inhibitory environment of the injured central nervous system (CNS). The primary goal of this work is to design a multifunctional, injectable hydrogel that supports neural repair following SCI. This project proposes the use of a branched copolymer based on poly(N-isopropylacryalmide) (PNIPAAm) and poly(ethylene glycol) (PEG). The thermosensitive nature of the hydrogel allows for easy implantation together with cellular grafts, and the controlled delivery of therapeutic factors. In this study, we investigated the cytocompatibility of the scaffold *in vitro* and also report its performance *in vivo*, with and without brain derived neurotrophic factor (BDNF) in a rodent model of SCI. Our results show that the injectable PNIPAAm-PEG scaffold completely fills the injury site, and does not elicit a larger host inflammatory response than a commercially available gelatin sponge. In addition, we have shown that the scaffold loaded with BDNF is permissive to host axon growth. With these promising results, we suggest that an injectable PNIPAAm-PEG hydrogel can serve as a multi-functional device that will result in an effective platform technology for the treatment of SCI.**

I. Introduction

Spinal cord injury (SCI) affects thousands of Americans each year. Repairing SCI is challenging due to the inability of adult neurons to regenerate and the inhibitory environment of the injured central nervous system (CNS). While currently there is no cure for SCI, significant advancements have been made in the areas of neuroscience, cell transplantation and biomaterials that could lead to new treatments. Some of the most promising strategies that have emerged over the past decade include therapies involving polymer scaffolds, delivery of neurotrophic factors (NTFs), and cellular transplants. Here, we propose the development of a novel, injectable polymeric scaffold that allows for the delivery of cells and NTFs to the injury site. The use of this scaffold is particularly promising because it integrates current strategies in spinal cord repair into one multifunctional device, while overcoming known disadvantages associated with existing polymeric materials.

The scaffold is composed of the thermally responsive copolymer, poly(N-isopropylacrylamide) and poly(ethylene glycol) (PNIPAAm-PEG). Below its lower critical solution temperature, (typically around 32°C) PNIPAAm is hydrophilic, so it forms a miscible solution with water. Above its LCST, it becomes hydrophobic, so the polymer and water separate, forming a solid gel (1). This property allows for easy delivery of a scaffold to the site of injury where it conforms to the shape of the cavity. Additionally, the polymer structure can be tailored to match the mechanical properties of the gel to spinal cord tissue (2). Because of the injectable nature of the system, therapeutic factors like brain derived neurotrophic factor (BDNF) can be co-dissolved in the polymer solution at room temperature and be released from the polymer by diffusion once gelation occurs (2). In addition, the potential for incorporation of cells, e.g. neural precursor cells, into the gel allows for the replacement of lost or damaged neurons and glial cells. In this study, the performance of the PNIPAAm-PEG branched copolymer, with and without BDNF, was evaluated *in vivo*. Results were compared to a commercially available matrix, Gelfoam® (Pfizer). Host inflammatory response to the scaffold and its ability to permit host axon growth were evaluated in an adult rodent model of SCI.

II. Materials and Methods

PNIPAAm-PEG copolymers were prepared as described previously (1). To prepare hydrogels, the copolymers were dissolved in cell culture medium at a concentration of

10wt% polymer. Solutions were steam-sterilized prior to use. For the cytocompatibility tests, $6.5x10^4$ primary rat fibroblasts were suspended per milliliter of polymer solution and cultured *in vitro* for 7 days. Cell viability was evaluated with Live/Dead stain (Molecular Probles). For the *in vivo* studies, adult female Sprague-Dawley rats received a partial hemisection at C3/C4. Immediately after injury, 3-5 uL of the PNIPAAm-PEG solution, with or without 0.05 ug/uL co-dissolved BDNF, was injected into the injury. Animals were euthanized and perfused with warm saline and 4% paraformaldehyde WHEN. The tissue was cut along the horizontal plane at 20 um thickness and immunostained to determine host inflammatory response (anti-IBA-1 for detecting macrophages and microglia), host axon growth (mouse anti-RT97 for neurofilments) and scar formation (rabbit anti-glial fibrillary acidic protein (GFAP) for astrocytes).

III. Results

In testing the compatibility of the scaffold with cells the *in vitro* Live/Dead cell staining indicated viability of fibroblast cells encapsulated within the hydrogel for 7 days (Figure 1). Analysis of scaffold implantation by injection into the injured spinal cord indicated that the hydrogel filled the injury site and remained for at least 4 weeks (not shown). Neurofilament staining for PNIPAAm-PEG with BDNF (Figure 2) clearly shows host axons entering the gel-filled injury site. In addition, by comparing the extent of macrophages and microglia staining for PNIPAAm-PEG (Figure 3) to commercially available cell transplant Gelfoam® (not shown), it was determined that our scaffold did not elicit a greater host inflammatory response. These preliminary results support the feasibility of this scaffold for use in the CNS.

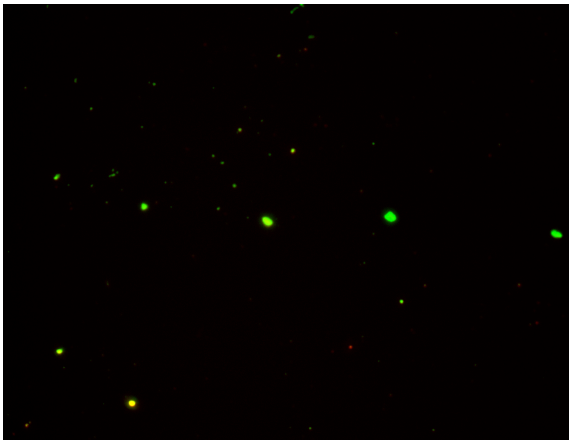

Fig. 1. Live/Dead staining of primary rat fibroblasts encapsulated in PNIPAAm-PEG gel for 7 days.

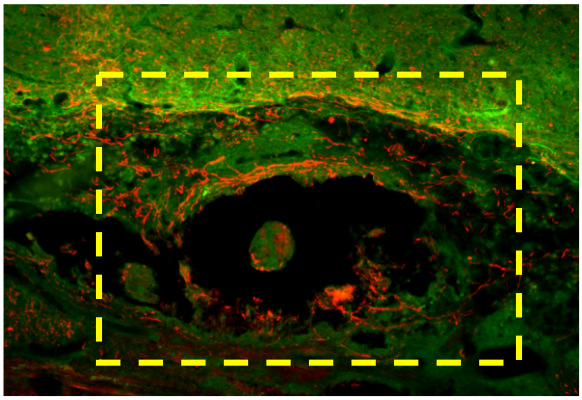

Fig. 2. Neurofilament (red) and GFAP (green) immunostaining of defect site implanted with PNIPAAm-PEG copolymer and co-dissolved BDNF. The injury site is highlighted in yellow.

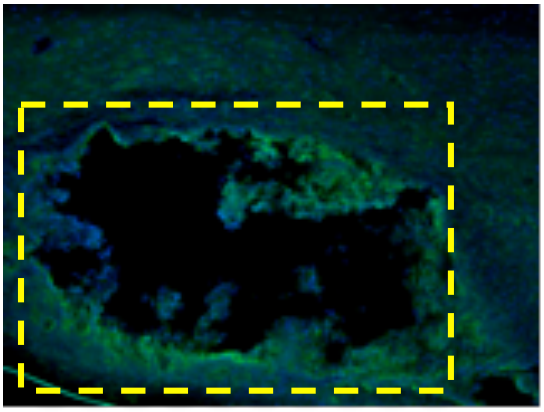

Fig. 3. IBA-1 staining (green) of the injury site implanted with PNIPAAm-PEG with co-dissolved BDNF highlights macrophages and microglia. The injury site is highlighted in yellow.

IV. Conclusions

Our preliminary *in vitro* results demonstrate the viability of encapsulated rat fibroblasts for at least 7 days. Our *in vivo* analysis have shown that the PNIPAAm-PEG scaffold completely fills the injury site and does not elicit a larger host inflammatory response than a commonly used commercially available scaffold. We have also demonstrated that the scaffold, with the inclusion of BDNF, is permissive to host axon growth. Currently, we are evaluating the potential of this multi-functional scaffold to serve as a transplantation vehicle for neural precursor cells. Our future work will focus on combining these treatment strategies with anti-scar therapy.

V. References

1. Vernengo J, Fussell GW, Smith NG, Lowman AM. Evaluation of novel injectable hydrogels for nucleus pulposus replacement. Journal of Biomedical Materials Research Part B: Applied Biomaterials. 2008;84B(1):64-9.
2. Comolli N, Neuhuber B, Fischer I, Lowman A. In vitro analysis of PNIPAAm–PEG, a novel, injectable scaffold for spinal cord repair. Acta Biomaterialia. 2009;5:1046-55.

In Vitro Degradation of Calcium Sulfate Polymer Composites for the Reconstruction of Bone

N. Tovar[1,2] , P. Lee[1], S. Mamidwar[2], H. Alexander [2] and J. Ricci[1]
[1] New York University College of Dentistry, Room 804S
345 East 24th Street
New York, NY 10010
[2]Orthogen, LLC
505 Morris Avenue, Suite 104
Springfield, NJ 07081

Abstract. **We are testing degradation rates of calcium sulfate/polymer composites meant for use as bone graft substitutes. The goal is to demonstrate the potential of composite degradable and biocompatible materials that will resorb slower than pure calcium sulfate. We will determine which composites give us degradation profiles that are appropriate for different types of bone regeneration**

Introduction. Various bone grafting materials have been used in the medical industry, but none have been used as long as calcium sulfate (CS). CS is osteoconductive, biodegradable and biocompatible. The main problem associated with CS is its rapid degradation, which prevents its use in large defects. The purpose of this *in vitro* study is to evaluate the degradation rate of novel CS/polymer composites and compare them to pure CS. The goal is to find a composite with an appropriate degradation rate based on granule size and polymer:CS ratio. Composites of CS with different polymers were fabricated. The polymers used were poly(DTE)-carbonate (p(DTE-C)), salicylate-based poly(anhydride-esters) (PA) and poly(L-lactic) acid (PLLA). Ratio of polymer/CS was 4:96. P(DTE-C) is a biocompatible and biodegradable material that has a higher tensile strength than pure CS. PA releases salicylate and is an anti-inflammatory polymer that could locally reduce inflammation and pain at site of implantation. As an anti-inflammatory, PA can potentially also reduce bone resorption. PLLA, a common biomaterial, should also regulate the degradation of CS. With potentially longer degradation profiles, anti-inflammatory properties, and ability to heal and reduce bone resorption, these composites could be used in larger bony defects, where normal CS has not worked well.

Materials and Methods. All materials were made by agglomeration and provided by Orthogen, LLC (Springfield, NJ). All materials were sieved in order to obtain granules in the size range of 600 µm. *In vitro* testing was done as described by Mamidwar *et al.*. Composite granules were wrapped in individual meshes and submerged in simulated body fluid (SBF) at 37 ºC [1];. SBF was prepared according to Kokobu *et al*'s formula [2]. SBF was changed every 3-4 days. An initial weighing was done at day 4, which serves as the baseline. Weighing during each change provided data to support a degradation curve, which is used to determine each composite's degradation profile.

Results. Preliminary 38-day data (Figure 1) shows that all materials have dissolved and lost mass over time. CS has degraded to approximately 50% of its original mass, while 4% PLLA has degraded the least and is approximately 80% of its original mass. 4% PA and p(DTE-C) are approximately 70% or their original masses.

Discussion. Composites of CS and resorbable polymers can be produced as agglomerated granules in defined size ranges. Small amounts of polymer can significantly delay dissolution of CS. This will allow us to produce CS composites that can be used to repair larger bone defects. We will test selected composites in critical sized cranial defects in rabbits, in order to determine potential materials for human clinical use.

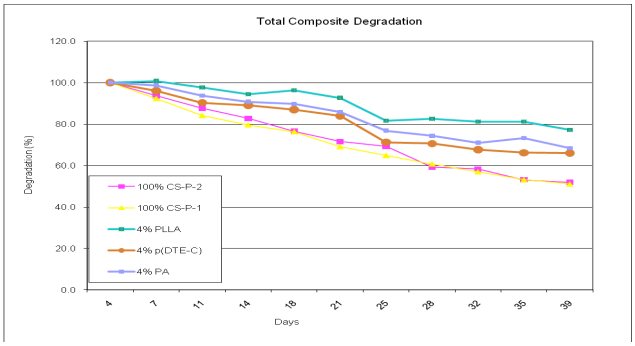

Figure 1: Degradation profiles of 600 µm composites at 38 days.

References

[1] Mamidwar S., Weiner M., Alexander H. and Ricci J. Implant Dentistry 17(2):208, 2008.
[2] Kokubo T., Kushitani H., Sakka S., Kitsugi T. and Yamamuro T. Journal of Biomedical Materials Research 24(6):721-734, 1990.

Supported by NIH Grant R44DE015703

A Novel Drug Delivery Device for Orthopedic Applications

Shang Song[1], Yupeng Chen[2], Hicham Fenniri[4] and Thomas J. Webster[1, 3]

[1]Division of Engineering, [2]Chemistry Department, [3]Department of Orthopaedics, Brown University, Providence, 02912, RI, USA.
[4]National Institute for Nanotechnology and Department of Chemistry, National Research Council and University of Alberta, Edmonton, AB T6G ZV4, CANADA.

Abstract

Rosette nanotubes (RNTs) are novel, biomimetic, synthetic, self-assembled drug delivery agents. Because of base stacking and hydrophobic interactions, the RNT hollow-tube structure can be used for incorporating drugs. Another advantage of using RNTs is their ability to be injected and become solid at body temperatures for orthopedic applications without the use of any external stimuli (such as UV light or crosslinking agents). The nano-features of RNTs create a favorable, biologically-inspired, cellular environment. In this study, methods to incorporate DEX (DEX, a bone growth promoting drug) into RNTs were investigated. The drug-loaded RNTs were characterized using Nuclear Magnetic Resonance (NMR), Diffusion Ordered Spectroscopy (DOSY) and Ultraviolet-visible Spectroscopy (UV-vis). Results showed that small molecular drugs with hydrophobic aromatic rings were incorporated into RNTs. Subsequent drug release experiments demonstrated that DEX was released from the RNTs and had a positive impact on osteoblast functions. Importantly, compared to other drug carriers, RNTs increased the total drug loading and was the highest when DEX was incorporated during the RNT self-assembly process. Thus, this study offered a novel drug delivery device that itself is bioactive and can be used to deliver a variety of drugs for various orthopedic applications.

I. INTRODUCTION

To enhance the integration of implant materials with bone forming cells (osteoblasts) and surrounding bone, nano-featured implant materials have received numerous attention as the next generation of bone implant materials. One type of nanomaterial, rosette nanotubes (RNTs), are novel biomimetic self-assembled supramolecular structures, whose basic building blocks are guanine (G) and cytosine (C) DNA base-pairs which can solidify into a viscous gel [1~2]. The G^C units undergo a hierarchical self-assembly process under physiological conditions to form a six-membered supermacrocycle by the formation of 18 hydrogen bonds. Because of electrostatic forces, base stacking interactions and hydrophobic effects, the rosettes form a stable stack with an inner channel 11Å in diameter. An amino acid side chain (lysine) was chosen to impose chirality and surface chemistry on the RNTs. Especially, the nano-structured, biomimetic features of RNTs created a favorable, biologically-inspired cellular environment. It was reported that such nanotubes have a similar size and morphology with collagen, enhance select protein adsorption and consequently a variety of cell functions [2~3].

In the present study, to determine if RNTs are ideal drug delivery devices, the objective of this study was to verify the drug-delivery ability of RNTs. Specifically, the drug-loaded RNTs were characterized using Nuclear Magnetic Resonance (NMR), Diffusion Ordered Spectroscopy (DOSY) and Ultraviolet-visible Spectroscopy (UV-vis).

II. METHODS

Characterization of DEX loaded RNTs-K1

4.07mg of RNTs-K1 building blocks were first dissolved in 1mL d-methanol. After RNTs-K1 self-assembled after one day, 1.3 μL Tert-butanol (Sigma, (≥99.5%; anhydrous) was added as a standard control for comparing any decrease in DEX (Sigma, D4902) integration on ^{1}H NMR. 5.11mg of DEX was added for drug loading giving a 5mg/mL DEX to d-methanol solution. Thus, a ratio of 5:3 DEX to RNTs-K1 was studied. After two days of the drug loading process, the supernatant was taken for analysis. The supernatant was then characterized by Proton Nuclear Magnetic Resonance (^{1}H NMR), Diffusion Coefficient Spectroscopy (DOSY) and Ultraviolet-visible spectroscopy (UV-vis). The percentage of the diminishing drug peak was recorded compared to the standard to determine the amount of drug loaded on ^{1}H NMR spectra. Under the same experimental conditions, DOSY experiments were performed to detect subtle changes in coefficients of unincorporated DEX under the presence of RNTs-K1.

For UV-vis experiments, the supernatant of about 4.07 mg drug loaded RNTs-K1 was diluted with methanol into a 0.025 mg/mL drug loaded RNTs-K1 mixture. In addition, another two groups were also prepared: 1. 0.005 mg/mL DEX was made in methanol; 2. 0.025mg/mL RNTs-K1 was created. 3mL of each group was placed into a 1cm x 1cm cuvette for UV-vis experiments, in which peaks from DEX, RNTs-K1, and DEX-RNTs-K1 were compared for differences.

Drug release study for RNTs-K1 drug loaded with DEX (Sigma, D2915)

Glass coverslips (circular; Dia: 18mm; Thickness: 1mm) were purchased from Fisher Scientific. They were cleaned by methanol, acetone and water in a sonicator. Three groups were prepared in deionized water: 1. glass coverslips were dipped in 1mg/mL of a DEX solution; 2. RNTs were dissolved and self-assembled in 1mg/mL of a DEX solution making a 0.1mg/mL RNT solution. Then glass coverslips were immersed into such a solution; 3. Glass coverslips were first soaked into a 0.1 mg/mL RNT solution. After air drying, they were then immersed into in a 1 mg/mL DEX solution. Then, all three groups were air dried and placed in 6-well plates with 3 mL of a PBS buffer per well inside a 37^{o}C incubator. The supernatant was then extracted on a daily basis for up to 10 days. A BCA assay was used at an absorbance of 562nm to determine released DEX.

Drug bioactivity experiments

Osteoblasts (bone-forming cells, ATCC, CRL-11372 population numbers <9) were seeded at 1000 cells/cm^2 in well plates and were cultured in Dulbecco's modified eagle's medium (DMEM; Gibco/BRL, Grand Island, NY) supplemented with 10% fetal bovine serum (FBS; HyClone, Logan, UT) and 1% penicillin/streptomycin (P/S; Hyclone) under standard cell culture conditions (37 ºC, a humidified, 5% CO_2/95% air environment). 10µL of released DEX from controlled release experiments and fresh DEX that were sterilized and diluted to 10^{-8} M were added along with the culturing medium to wells. After the prescribed time period, non-adherent cells were removed by washing with phosphate buffered saline (PBS) twice. At the end of 1, 3 and 5 days, osteoblasts were fixed with 10% normal buffered formalin (NBF; Fisher Scientific), stained with 4',6-diamidino-2-phenylindole, dihydrochloride (DAPI; Invitrogen, Carlsbad, CA), and counted on five random fields of view for each well under a fluorescence microscope.

Statistical analysis

Data were expressed as the mean standard deviation (SD). Statistics were performed using student's one-tailed t test, with $p<0.05$ being considered statistically significant.

III. RESULTS AND DISCUSSION

Due to their large molecular weight and long relaxation time, RNTs and the DEX incorporated RNTs were not visible on 1H NMR spectra. Therefore, the percentage of drug loaded could only be analyzed by deducting differences in peak heights of the drug compared with standards. As shown in Table 1, at the DEX:RNT ratio of 5:3, about 32% of DEX was incorporated into the RNTs. To further provide evidence for the incorporation of DEX into RNTs, a change in the diffusion coefficient of the DEX peak from 5.8 to 5.1 was observed in DOSY spectra (Table 2), which indicated the interaction between RNTs and DEX.

For UV-vis experiment, after incorporated with RNTs, DEX showed a different UV adsorption curve. Such results also proved the bonding between RNTs and DEX in the solution, as shown in Figure 1.

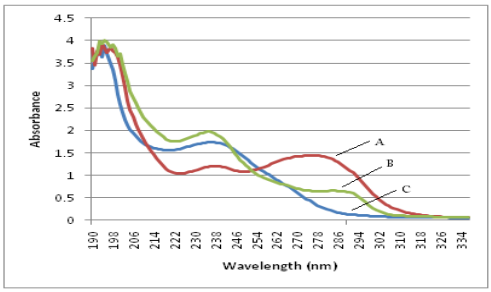

Figure 1. Comparison of UV-vis adsorption of 0.025mg/mL RNTs-K1 (A), 0.025mg/mL DEX-RNTs-K1 (B) and 0.005mg/mL DEX (C).

The drug release studies showed that the RNTs were able to load more drugs onto glass surfaces than unaltered glass surfaces. Specifically, on the average of the last three days of total drug release amount, DEX coated on RNTs had loaded 54.6% more drugs than the controls and DEX embedded with RNTs had loaded 78.1% more drugs than the controls. Such results suggested that DEX were incorporated into RNTs via their self-assembly by hydrophobic interactions and base stacking efforts (Figure 2).

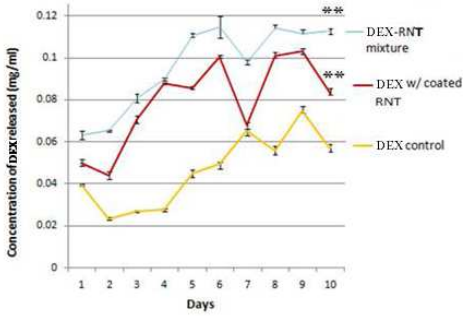

Figure 2. DEX release curve up to 10 days. Data are mean ±SEM (n = 12). **p < 0.05 compared to the controls (DEX only).

From drug bioactivity cell studies, released DEX was not only as active as fresh DEX solutions, but the RNT:DEX solution also resulted in higher osteoblast density due to the bioactivity of the released RNTs (Figure 3).

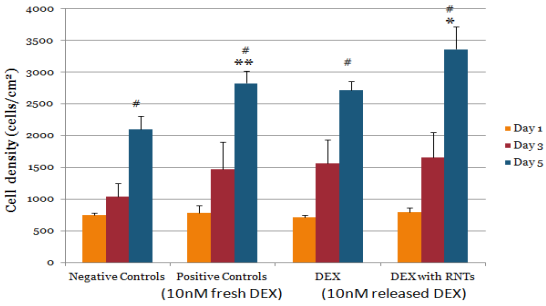

Figure 3. Osteoblast density cultured with released DEX. Data are mean ± SEM (N=3). **p<0.05 compared to negative controls (no additives). *p<0.05 compared to both controls and DEX. #p<0.05 compared to day 1 and 3 results.

IV. CONCLUSIONS

This study demonstrated that RNTs were able to incorporate drugs (DEX) and increase drug loading when self-assembled at body temperatures. Moreover, DEX released from RNTs was still bioactive, even more so than fresh DEX alone. In this manner, RNTs are multi-functional drug delivery devices, which are able to deliver drugs with different properties by chemical functionalization of short peptides on the outer layer and by physical adsorption of small molecules in the tubes for bone regeneration.

V. ACKNOWLEDGEMENTS

The authors would like to thank Mr. Jae Young for assisting NMR and DOSY studies and the Hermann Foundation for funding.

VI. REFERENCES

[1] Chun AL, Moralez JG, Fenniri H, Webster TJ. "Helical rosette nanotubes: a biomimetic coating for orthopedics?" *Biomaterials 2005*, 26: 7304-7309.

[2] Fenniri H, Mathivanan P, Vidale KL, Sherman DM, et al. "Helical rosette nanotubes: design, self-assembly and characterization," *J. Am. Chem. Soc. 2001*, 123, 3854-3855.

[3] Zhang L, Chen Y, Rodriguez J, et al. "Biomimetic helical rosette nanotubes and nanocrystalline hydroxyapatite coatings on titanium for improving orthopedic implants," *Int J Nanomedicine. 2008*, 3(3):323-333.

Calcium Phosphate Coating on Tendons via Concentrated Simulated Body Fluid Soaking

P. Chuang, M.A. Advincula, H.H. Lu
Columbia University
351 Engineering Terrace, 1210 Amsterdam Ave
New York, NY 1027

***Abstract*—The regeneration of the tendon to bone insertion site affects how well the ACL heals. The addition of a calcium phosphate coating to a tendon graft can help to promote osteointegration and healing of the insertion. Patellar tendons were harvested from neonatal bovines and coated in semi-crystalline calcium phosphate. The tendons were subjected to two 5x concentrated simulated body fluid solutions to layer first an amorphous calcium phosphate coating, followed by a semi-crystalline layer. X-ray diffraction confirms the resultant coating to be similar to hydroxyapatite, which is the mineral phase found in bone. Tensile mechanical testing shows no effect on the ultimate tensile strength of tendons coated in semi-crystalline calcium phosphate. The similarities of the coating to the mineral found in natural bone as well as negligible effects of the coating on the mechanical strength of the tendon give the grafts potential for use in repair of the tendon to bone insertion site.**

I. Introduction

During anterior cruciate ligament (ACL) reconstruction, the fixation of tendons within the bone tunnel and the regeneration of the tendon-to-bone insertion site affect how well the ACL heals [1]. The addition of a calcium phosphate layer to tendon grafts can help to promote osteointegration of the tendon to the bone and potentially improve the mechanical strength of the graft. A popular method of applying calcium phosphate coatings to substrates has been simulated body fluid (SBF) soaking. SBF soaking offers a low temperature processing technique, ideal for substrates that can be altered by the high temperatures involved in other techniques such as plasma spraying [2]. This method also allows for a relatively uniform coating on complex surfaces [3]. While several techniques have demonstrated an ability to apply low-crystalline calcium phosphate coatings to tendons [4], having a more crystalline form of calcium phosphate affixed to the tendons is desirable as it would closely match the hydroxyapatite structure found naturally in bone. The objective of this research is to apply a coating of crystalline calcium phosphate (apatite) to tendons. We hypothesize that the addition of a crystalline calcium phosphate layer to tendons will improve osteointegration.

II. Methods

Tissue Preparation: Patellar tendons were obtained from neonatal bovine knee joints (Green Village). Samples were rinsed in phosphate buffered saline prior to lyophilization. The freeze dried samples were stored at room temperature.

Simulated Body Fluid Soaking: Concentrated simulated body fluid (SBF) solution preparation was adapted from Habibovic *et al* [5]. Tendons were coated using a series of SBF solutions, SBF A and SBF B. The two SBF solutions were prepared with ion concentrations according to the table 1 below. All chemicals were acquired from Sigma Aldrich.

TABLE 1
Solution Ion Concentrations

Ion	SBFx5 (mM)	SBF A (mM)	SBF B (mM)
Na^+	710	733.5	733.5
K^+	25		
Mg^{2+}	7.5	7.5	1.5
Ca^{2+}	12.5	12.5	12.5
Cl^-	739	720	720
HPO_4^{2-}	5	5	5
SO_4^{2-}	2.5		
HCO_3^-	21	21	10

SBF A: The SBF A solution forms an amorphous calcium phosphate coating on the submerged sample to act as a precursor (or calcium phosphate seed) to the crystallization of hydroxyapatite (HA). Recent studies have shown that the final form of HA is preceded by an intermediate amorphous calcium phosphate phase [6]. Distilled water was brought to and maintained at 37°C. NaCl, $MgCl_2 \cdot 6H_2O$, and $CaCl_2$ were added in order while mixing with a magnetic stir bar. The pH of the solution was brought below 4 through bubbling with CO_2 gas before the $Na_2HPO_4 \cdot 2H_2O$ and $NaHCO_3$ were added. The CO_2 was left bubbling in the solution until the pH fell below 6.2. The CO_2 source was then removed and the tendon samples were suspended in the solution. The solution was kept stirring and fixed at 37°C for 24 hours to allow for the CO_2 gas to gradually leave the solution. The samples were then removed from the solution and rinsed in distilled water to remove excess amorphous calcium phosphate coating.

SBF B: The coated sample is then placed in a SBF B solution, whose ion content is similar to SBF A except for a lowered crystal growth inhibitor ion content (Mg and HCO_3), leading to the maturation of calcium phosphate into an HA like phase. The SBF B solution was made following the SBF A procedure except for two noticeable differences: the Mg^{2+} and HCO_3^- ion concentrations were lowered according to the ion concentration table, and the temperature of the solution

was kept at 50°C. After the SBF B solution was brought below a pH of 6.2 through CO_2 bubbling, the amorphous calcium phosphate coated tendons were hung in the solution. After the 24 hour immersion, the pH of the solution was monitored to be above 7.0 before removal of the tendons. The samples were rinsed in distilled water and lyophilized prior to storage at room temperature.

Control Groups: Control group tendons were prepared by immersing tendons in distilled water at 37°C for 24 hours, to mimic the SBF A solution cycle, and 50°C for 24 hours to mimic the SBF B solution cycle.

Characterization: Residue calcium phosphate powder from both solutions as well as tendon samples was collected for x-ray diffraction (XRD) analysis. Scanning electron microscopy (SEM) images of the tendon surface were obtained to examine the morphology of the tendon surface. Young's modulus and ultimate tensile strength of coated and uncoated tendons were determined via tensile test (n=5) and analyzed statistically by the tukey HSD model.

III. Results

XRD analysis shows the presence of peaks characteristic of those found in hydroxyapatite in both the coated tendon and the isolated SBF B powder (figure 1). Of particular interest are peaks found at 2θ locations around 32.0535-34.1952, and 46.788-53.5459, which are specific to hydroxyapatite (table 2; International Centre for Diffraction Data file). SEM images give evidence of the rough surface resulting from the calcium phosphate coating (figure 2). Tensile testing of the tendon samples show that the coated tendon samples have a lower Young's modulus than the control tendon sample, and no effect on the ultimate tensile strength (figure 3; $p<0.05$).

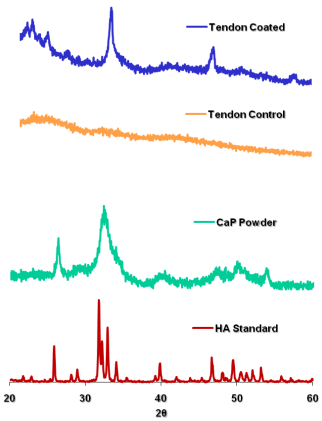

TABLE 2
SELECT PEAK LOCATIONS (DEGREES)

CaP Powder	HA (ICDD)
25.7255	25.8786
28.3268	28.6804
31.7953	32.0535
	34.1952
39.4549	39.6722
	42.4011
45.2356	43.9154
46.3918	46.788
49.2822	49.4963
53.0397	53.5459

Figure 1: *XRD patterns of a coated tendon sample (top), a tendon control, isolated SBF B powder, and HA standard (bottom) with a table comparing the peak locations of the SBF B and HA powders*

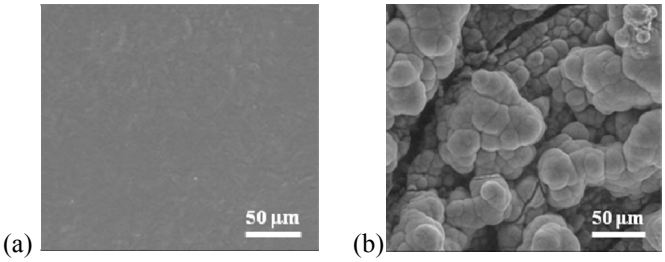

Figure 2: *Scanning electron microscopy images for (a) uncoated and (b) coated tendons at 15kV, 1000 X magnification*

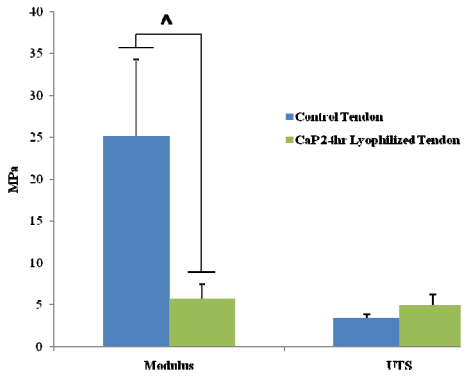

Figure 3: *Comparison of Young's moduli and ultimate tensile stress for coated and uncoated tendons (^ $p<0.05$)*

IV. Discussion

The resulting x-ray diffraction spectra (figure 1) show a crystalline form of calcium phosphate was formed on the tendons. While multiple peaks should exist in the 32.0535-34.1952, and 46.788-53.5459 angle ranges for hydroxyapatite, the presence of two broad peaks suggest that the coating is semi-crystalline calcium phosphate and the broad peaks represent merged signals. A cross sectional SEM image of the tendon (not shown) shows the thickness of the coating to be 350±50µm. The mechanical properties results suggest that the presence of the calcium phosphate coating lowers the Young's modulus of tendon grafts, but has no effect on the ultimate tensile strength. The similarities of the resultant coating to that of natural bone mineral, and the negligible effects of the coating on the strength of the tendon give promise for use of these grafts in ACL reconstruction.

References

[1] F. Tomita, B. *et al*, "Comparisons of intraosseous graft healing between the doubled flexor tendon graft and the bone-patellar tendon-bone graft in anterior cruciate ligament reconstruction," *Anthroscopy,* vol. 17.5, pp. 461-76, 2001.

[2] C. Du, *et al*, "Biomimetic calcium phosphate coatings on polyactive 1000/70/30," *J. Biomed. Mater. Res.,* vol. 59, pp. 535-46, 2002.

[3] P. Layrolle, *et al,* "Biomimetic calcium phosphate coatings and their biological performances," *Bioceramics*, vol. 13, pp. 391-94, 2001.

[4] S. Tanaka, *et al,* "Apatite coating in/on rabbit tendons using an alternative soaking process," *Bioceramics,* vol. 192-1, pp. 479-82, 2000.

[5] P. Habibovic, *et al,* "Biomimetic hydroxyapatite coating on metal implants," *J. Am. Chem. Soc.*, vol. 3, pp. 517-22, 2002.

[6] S. Weiner, *et al.,* "Overview of the amorphous precursor phase strategy in biominearlization," *Front. Mater. Sci.*, vol. 3, pp. 104-08, 2009.

Osteogenic Differentiation of hESCs After Culturing on Fibrillar Type I Collagen Coatings

Yongxing Liu[1], A. Jon Goldberg[1], John T. Elliott[2], Anne L. Plant[3] and Liisa T. Kuhn[1]
[1]Reconstructive Sciences, University of Connecticut Health Center, Farmington, CT,
[2]Biochemical Science Division, National Institute of Standards and Technology, Gaithersburg, MD, [3]NIST, Gaithersburg, MD

***Abstract*-This paper reports a new method to induce osteogenic differentiation of human embryonic stem cells (hESCs). Singly dissociated hESCs treated with ROCK inhibitor Y27632 were plated on type I fibrillar collagen (FC) coatings and achieved a high rate of survival. After culturing in osteogenic medium for 10 d, several cell colonies developed on the coatings. Cells forming the colonies showed homogenous, fibroblastic-like morphology. Subcultures of these cells on FC coatings in osteogenic medium developed an osteoblastic phenotype evidenced by strong staining for deposited minerals and expression of the ostoblastic related genes Runx2 and Col1a1. However, gene expression of osteocalcin (OC) was not detected, implying that while mineral deposition was mediated by the cells they did not mature during the culture period. FACS analysis showed the surface markers were 82.9% $CD73^+$, 81.0% $CD105^+$ and 99.8% $CD45^-$,consistent with the pattern of MSCs'. Additionally, in subsequent second subcultures these cells displayed a 5-fold increase in OC gene expression. We conclude that FC either exerted a unique cell-matrix interaction which promoted osteogenic differentiation or it selectively supported the survival and growth of cells committed to the osteoblastic lineage. Further characterization of the cells and the cell-collagen coating interactions are in progress.**

I. INTRODUCTION

Controlling the differentiation of hESCs to obtain homogeneous, high yields of the desired terminal cell type remains a challenge. Biomaterials could be employed here because they can have a strong influence on stem cell differentiation and maintenance [1]. For example, type I collagen surfaces have been shown to effectively promote osteogenic differentiation of osteoblastic progenitor cells [2] and fibrillar collagen (FC) can have additional important influences [6]. Thus we postulated that FC may also promote the osteogenic differentiation of human embryonic stem cells (hESCs).

The dissociation method also affects differentiation of hESCs. Differentiation improved when the undifferentiated cells were singly dissociated and plated in contrast to the use of embryoid bodies (EBs) [3]. However, the traditional enzymatic dissociation of hESCs generally causes high rates of cell death and survival rates usually lower than 5% [3]. Therefore, we employed recently reported methods to promote the survival rate of singly dissociated hESCs, i.e., combing the treatment with a ROCK inhibitor Y27632 [4] and the use of Accutase® to dissociate cells [5]. After 10 days, homogenous, fibroblastic-like cell colonies were obtained on the coating and the cells obtained were subcultured to test for the differentiation potential towards osteoblasts.

II. MATERIALS AND METHONDS

A: Cells

H9 (WiCell, Madison, WI, USA) were maintained on Matrigel with mouse embryonic fibroblast (MEF)-conditioned medium supplemented with 4 ng/ml bFGF. Passage 44 was used for the differentiation experiment.

B: FC Coatings

Purified bovine collagen monomers stabilized in an acidic solution (PureCol, Inamed Biomaterials) was used at a concentration of 300 µg/ml to prepare fibrillar coatings following a NIST protocol with modifications [6]. Briefly, the collagen was diluted in phosphate buffered saline solution (PBS) using the following proportions 70:1:1:8 v:v of 1x PBS, 0.1 M NaOH, 10 x PBS and PureCol solution in a 50 mL conical tube. The collagen stock solution was added last to minimize the formation of insoluble aggregates. 1 ml of the diluted solution was added per well in 12-well non-tissue culture treated plates. After incubating at 37^{o}C in humidified air with 5% CO_2 for 12-21 hrs, the gel-like supernatant was aspirated from the plates and the coating surfaces were rinsed with PBS twice. 1 ml PBS was added to each well to cover the coatings for later use.

C: Plating and Culturing Cells

Before dissociation, the hESCs were treated with Y27632 which was added to the maintenance medium at 10 uM concentration and incubated for 1 hr. Then colonies were dissociated into single cells using Accutase®. The cells were spun down and re-suspended in the maintenance medium supplemented with 10 uM Y27632. Cells were incubated for one day, then the medium was supplemented with an equal volume of osteogenic medium (OM). After incubating for two more days only OM was used with changes every 3-4 days. For subcultures, cells were trypsinized by 0.25% Trypsin+EDTA.

D: Osteogenic medium (OM)

The OM contained basal alpha-MEM, 10% FBS, 1% penicillin and streptamycin, 100 nM dexamethasone, 50 uM ascorbic acid-phosphate, and 4mM beta-glycerophosphate. In

the first subculture, higher concentrations of the components were used for the last one week, i.e., 20% FBS, 1 uM dexamethasone, 250 uM ascorbic acid-phosphate.

III. RESUTLS

The singly differentiated hESCs began to attach onto the FC coatings one day after plating. After supplementing OM on the second day, cells continued to attach. After 10 d several colonies could be observed at the edge regions of the culture wells (Fig. 1A), while most of the plate was devoid of cells. This unique phenomenon was observed only on the FC coatings in contrast to non-fibrillar coatings or tissue culture treated polystyrene where cell attachment was more robust. After trypsinizing and subculturing in OM for 10 d, the cells showed homogenous fibroblastic-like morphology (Fig. 1B). After 35 d, mineral deposition was observed which was stained strongly by xylenol orange dye (Fig. 1C and D). Gene expression for Runx2 and collagen type I measured with RT-PCR, showed >10-fold increase compared to the undifferentiated hESCs (Fig. 3). However, the marker for mature bone formation osteocalcin was not detected. FACS sorting indicated that these cells were 82.9% $CD73^+$, 81.0% $CD105^+$ and 99.8% $CD45^-$ which is consistent with the pattern of MSCs' [7]. This implied these cells were not yet fully differentiated into osteoblasts. We further subcultured these cells under osteogenic conditions on the FC coatings and observed an increase in mineralized nodule formation (Fig. 2), and Runx2, Col1a1, and OC gene expression (Fig. 3). Although the osteocalcin expression level was relatively weak there was a 4.4-fold increase above that for hESCs.

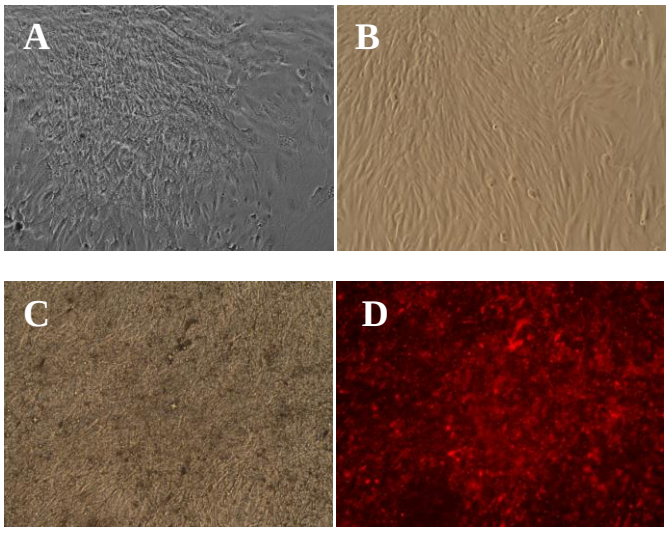

Fig. 1. Phase contrast images of the homogenous fibroblast-like cells on the FC coating, (A) after culturing for 10 d in OM, (B) the first subculture atr 10 d, (C) at 35 d and (D) xylenol orange staining for the 35 d culture. magnification: 100x.

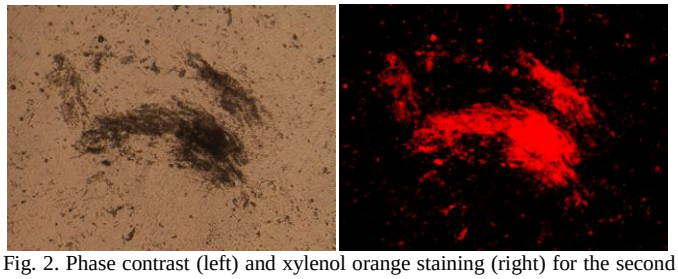

Fig. 2. Phase contrast (left) and xylenol orange staining (right) for the second subculture on 28 d. Magnification: 100x.

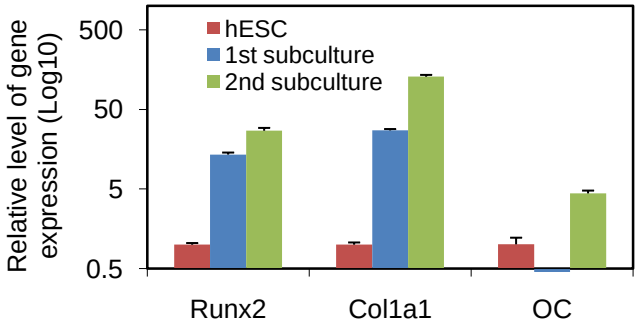

Fig. 3. RT-PCR analysis for the gene expression of Runx2, Col1a1, and OC. The gene expression level is relative to the undifferentiated hESCs'.

IV. CONCLUSIONS

This preliminary data is supportive of our hypothesis that the cells derived on FC coatings have been selected or guided by the biomaterial to differentiate towards the osteoblastic phenotype in the osteogenic medium. Apparently type I fibrillar collagen can exert unique stimuli on the differentiation of hESCs. The mechanism is not yet known, but we continue to study the underlying biomaterials-stem cell interactions. Further characterization, including immunostaining and in vivo functional assays will be conducted to critically define these cells and fully determine their capacity for osteogenesis.

REFERENCES

[1]. A.J. Engler, S. Sen, H.L. Sweeney and D.E. Discher," Matrix Elasticity Directs Stem Cell Lineage Specif.,"*Cell*, Vol. 126(4), pp. 677-689, 2006.

[2]. M.P. Lynch, J.L. Stein, G.S. Stein, and J.B. Lian, "The influence of type I collagen on the development and maintenance of the osteoblast phenotype in primary and passaged rat calvarial osteoblasts:," *Exp Cell Res* Vol.216, 35, 1995.

[3]. J. M. Karp, L.S. Ferreira, A. Khademhosseini, A.H. Kwon, J.Yeh, R.S. Langer, "Cultivation of Human Embryonic Stem Cells Without the Embryoid Body Step Enhances Osteogenesis In Vitro, *Stem cells*," Vol. 24, pp. 835–843, 2006.

[4]. A ROCK inhibitor permits survival of dissociated human embryonic stem cells K. Watanabe, M. Ueno, D. Kamiya. A. Nishiyama, M. Matsumura, T. Wataya, et al., *Nature Biotechnology*, Vol. 25, pp. 681-686, June 2007.

[5] R. Bajapai, J. Lesperance, M. Kim, A. Terskikh, "Efficient Propagation of Single Cells Accutase-Dissociated Human Embryonic Stem Cells," Molecular reproductionand Development, Vol. 75, pp. 818–827, 2008.

[6]. J.T Elliott, A. Tona, J.T. Woodward, P.L. Jones, and A.L. Plant, Thin films of collagen affect smooth muscle cell morphology. *Langmuir*, Vol. 19, pp.1506-1511, 2003

[7]. M. Dominici, K. Le Blanc, I. Mueller, I. S. Cortenbach, F.C. Marini, D.S. Krause, et al., Minimal criteria for defining multipotent mesenchymal stromal cells. The International Society for Cellular Therapy position statement. *Cytotherapy*, Vol. 8(4), pp. 315, 2006.

Development of Schwann Cell-Seeded Conduit Using Chitosan-Based Biopolymers for Nerve Repair

Atul Khataokar[1], Nolan Skop[1,2], Haesun Kim[3], Bryan Pfister[1], Cheul H. Cho[1]
[1]Department of Biomedical Engineering, New Jersey Institute of Technology, Newark, NJ 07102
[2]Department of Biomedical Engineering, University of Medicine and Dentistry of New Jersey (UMDNJ), Newark, NJ 07102
[3]Department of Biology, Rutgers University, Newark, NJ 07102

Abstract— **The purpose of this study is to develop biodegradable nerve guidance conduits seeded with Schwann cells (SC) using chitosan-based biopolymers for improving nerve regeneration. Chitosan, prepared from alkaline hydrolysis of chitin, is a natural polysaccharide biopolymer, having biocompatibility and biodegradability. In this study, chitosan and chitosan-gelatin membranes were prepared, characterized, and evaluated. The SC isolated from rat sciatic nerve was seeded on chitosan and chitosan-gelatin membranes to investigate their interactions. To enhance the SC attachment and growth on the membranes, we incorporated the poly-L-lysine (PLL) into chitosan and chitosan-gelatin network at various ratios of 1:800, 1:200, 1:50 (chitosan or chitosan-gelatin: PLL). We have also investigated the effect of extracellular matrix (ECM) molecules on the proliferation of SC. We observed that SC proliferation on PLL-coated surface was significantly higher than that of ECM coated and uncoated surfaces. With the increase of PLL ratio into chitosan or chitosan-gelatin network, the attachment and growth of SCs were significantly enhanced. This study indicates that the incorporation of PLL into chitosan and chitosan-gelatin membranes significantly improves the bioactivity of the materials. The Schwann cell-seeded films can be used to construct a three-dimensional nerve conduit for enhancing nerve regeneration.**

I. Introduction

The bridging of large nerve defects in the peripheral nerve system is a great challenge for nerve repair. Tissue engineered nerve grafts using biomaterials and cells are one of the promising strategies for nerve regeneration after injury. Mammalian cells require a substrate to grow on which makes biomaterial scaffolds an integral part of tissue engineering. The more the scaffold mimics the natural environment of the body, the more effective it will be. The scaffold will represent the three-dimensional conditions of the local ECM. Schwann cells play a critical role in peripheral nerve regeneration.

The autologous tissue graft used include autologous nerve grafts, autologous muscle and vein grafts (1). These autologous nerve grafts are biocompatible and less toxic than the artificial material, but have disadvantages of isolation from the donor site. Isolation generally requires an extra surgery and adds to the inconvenience of the patient. Nerve guidance conduits, that can physically guide the regenerating axons and also reduce the infiltration of scar tissue, can play a major role in nerve repair. In order to guide the regenerating nerve, bridging the nerve gap by tubes/conduits is promising strategy (1, 2). The biomaterial used to construct the conduit should provide optimal environment (structural, cellular) for the nerve to grow across the gap and also should not collapse in vivo after implantation.

In this study, chitosan and chitosan-gelatin membranes were prepared, characterized, and evaluated to develop biodegradable nerve guidance conduits seeded with SC for improving nerve regeneration. It is hypothesized that Schwann cell-seeded films composed of chitosan-based polymers will retain their structure and also promote neurite outgrowth.

II. Methods

A. Formation of Polymer: 1% chitosan solution was prepared by adding 1% acetic acid. 1% gelatin solution was prepared at 50°C. To prepare chitosan-based films, 0.5 mg/ml PLL solution was mixed with 1% chitosan (10 mg/ml) and 1% gelatin (10 mg/ml) solutions in quantities (weight ratios) as described below. The final concentration of poly-L-lysine in the solution were 0.2 mg/ml (CP50, CGP50), 0.05 mg/ml (CP200, CGP200), and 0.0125 mg/ml (CP800, CGP800). Chitosan-based films were made by casting and air-drying method.

Table 1. Chitosan/Gelatin (CP) and Chitosan/Gelatin/PLL (CGP) blends.

Ratio	Chitosan	PLL
CP50	50	1
CP200	200	1
CP800	800	1

Ratio	Chitosan/Gelatin (1:1)	PLL
CGP50	50	1
CGP200	200	1
CGP800	800	1

B. Cell Source: The Schwann cells were isolated from the neonatal rat sciatic nerves, as described earlier (3). Fetal rat dorsal root ganglions (DRG) were obtained from E 14.5 rat embryos.

C. Assays: The MTT colorimetric assay was performed to evaluate the effect of ECM on the Schwann cell attachment and growth. BrdU assay was performed to detect and compare the proliferating Schwann cells in culture conditions. Cellular morphology and phenotypes were evaluated by immunofluorescence staining and scanning electron microscopy.

III. RESULTS

MTT assay was used to compare the effect of, poly-L-lysine, gelatin, and extracellular matrix molecules like collagen, fibronectin and laminin, on the attachment and growth of Schwann cells. Maximum absorbance was observed on poly-L-lysine coated surface followed by laminin, fibronectin, gelatin, and collagen (Fig. 1). There is a considerable difference in the absorbance for Schwann cells cultured on poly-L-lysine and other molecules. There is no significant difference between uncoated tissue culture dishes, collagen coated surface and gelatin coated surface. There is also no significant difference between the fibronectin and laminin coated surface. Results of this study indicate that poly-L-lysine is the most suitable substrate for the Schwann cells to adhere, survive and proliferate.

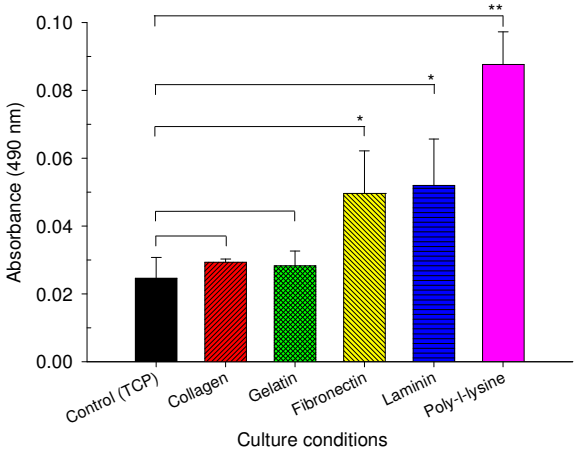

Fig. 1. Effect of ECM molecules on Schwann cell growth by MTT assay after 4 days of culture. The cells were maintained in the Schwann cell growth medium. Maximum absorbance was observed in case of Schwann cells growing on poly-L-lysine coated surface. (* $P < 0.05$; ** $P < 0.005$).

Schwann cells proliferate well on CP50 and CGP50 conditions, similar to SC cultured on PLL surface. As shown in Figure 2. B, the SC seeded on chtiosan-PLL film exhibited good cell attachment and growth, having spindle-shaped morphology. The actin microfilament was evenly distributed throughout the cells. Further analysis of the cells by scanning electron microscopy (Fig. 2C) revealed interactions of individual cells and spatial organization growing on the chitosan-PLL films. The Schwann cells seeded on the films exhibited a spindle-shaped morphology with abundant microvilli projected onto the film.

To further assess neurite outgrowth on SC-seeded films, we seeded dissociated DRG neurons on the top of SC-seeded chitosan-PLL films. Axonal outgrowth on the SC-seeded films was visualized by neurofilament staining after 7 days of culture. The DRG neurons co-cultured on the SC-seeded chitosan-PLL complex film exhibited a significant increase of the neurite outgrowth after 7 days of culture.

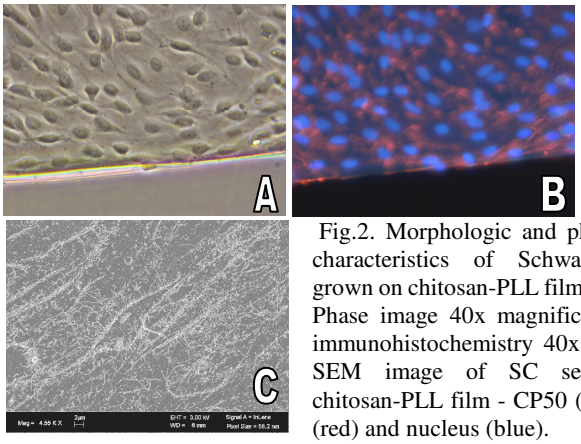

Fig.2. Morphologic and phenotypic characteristics of Schwann cells grown on chitosan-PLL film at Day 7. Phase image 40x magnification (A) immunohistochemistry 40x (B), and SEM image of SC seeded on chitosan-PLL film - CP50 (C). Actin (red) and nucleus (blue).

IV. DISCUSSION

In this study we were able to optimize chitosan-based biopolymer compatible for culturing Schwann cells. Chitosan modified by blending it with gelatin and poly-L-lysine is more supportive to the attachment and growth of Schwann cells. The Schwann cell proliferation was maximal on PLL-coated surfaces compared to ECM molecules. Schwann cells seeded on CP50 and CGP50 films showed similar attachment and growth to that cultured on PLL surface. DRG neurons cultured on SC-seeded chitosan-PLL complex film exhibited good neurite extension. The films are semi-permeable and prevent tissue in-growth that may prevent axon regeneration. The Schwann cell seeded films can be rolled to prepare conduits of required dimensions or the conduits can be fabricated by freeze-drying chitosan solutions. Both techniques are currently being studied in this lab. It is necessary to test the effectiveness and stability of these biomaterials in vivo. The in vivo testing can be carried out in the nerve injury rat model, where they can be implanted in the injured sciatic nerve and evaluated for regeneration. The Schwann cell-seeded conduits using chitosan-based biomaterials will be useful for many neural tissue engineering applications for nerve repair.

ACKNOWLEDGEMENT

This study was supported by NJIT startup fund.

REFERENCES

[1] Schmidt, C.E., and Leach, J.B. Neural tissue engineering: strategies for repair and regeneration. Annu Rev Biomed Eng 5, 293, 2003.

[2] Kim, I.Y., Seo, S.J., Moon, H.S., Yoo, M.K., Park, I.Y., Kim, B.C., and Cho, C.S. Chitosan and its derivatives for tissue engineering applications. Biotechnol Adv 26, 1, 2008.

[3] Brockes, J.P., Fields, K.L., and Raff, M.C. Studies on cultured rat Schwann cells. I. Establishment of purified populations from cultures of peripheral nerve. Brain Res 165, 105, 1979.

Expression, cross-linking and characterization of recombinant chitin binding resilin

Guokui Qin[1], Shaul Lapidot[2], Keiji Numata[1], Xiao Hu[1], Sigal Meirovitch[2], Mara Dekel[2], Itai Podoler[2], Oded Shoseyov[2], David L. Kaplan[1]
[1]Department of Biomedical Engineering, 4 Colby Street, Tufts University, Medford, MA 02155, United States
[2]The Robert H. Smith Institute of Plant Sciences and Genetics in Agriculture, Robert H. Smith Faculty of Agriculture, Food and Environment, the Hebrew University of Jerusalem. P.O. Box 12 Rehovot 76100 Israel.

***Abstract*—Resilin is a polymeric rubber-like protein secreted by insects to specialized cuticle regions, in areas where high resilience and low stiffness are required. Resilin binds to the cuticle polysaccharide chitin via a chitin binding domain and is further polymerized through oxidation of the tyrosine residues resulting in the formation of dityrosine bridges and assembly of a high-performance protein-carbohydrate composite material. We describe for the first time a comprehensive study on the mechanical, structural and biochemical function of chitin binding recombinant *Drosophila melanogaster* resilin. Various resilin constructs were cloned including the full length gene enabling Ni-NTA purification, as well as heat and salt precipitation for rapid and efficient purification. The binding isotherms and constants (K_d, B_{max}) of resilin to chitin via its chitin binding domain were determined and displayed high affinity to chitin, implying its important role in the assembly of the resilin-chitin composite. The structural and elastic properties were investigated using Fourier Transform Infrared Spectroscopy (FTIR), Circular Dichroism (CD) and Atomic Force Microscopy (AFM) with peroxidase crosslinked solid resilin materials. Generally, little structural organization was found by these biophysical methods, suggesting structural order was not induced by the dityrosine crosslinks. Further, the elastomeric properties found from the full length protein compared favorably with the shorter resilin generated previously from exon 1. The unusual elastomeric behavior of this protein suggests possible utility in biomaterials applications.**

I. Introduction

Resilin is found within structures where energy storage and long-range elasticity are needed, such as the flight system of locusts, the jumping mechanism of fleas, and the sound producing organ of cicadas [1]. Resilin behaves like an entropic elastomer, and was initially proposed to consist of randomly coiled protein chains linked by stable covalent cross-links, the elastic force being accounted for by a decrease in conformational entropy when the material was strained [2]. Further, resilin possesses high resilience, 92% or more, and a very high fatigue lifetime, due to the covalent cross-linkage between tyrosine residues, generating di- and trityrosines [2].

Ardell and Andersen identified *Drosophila melanogaster* resilin gene and reported two significant elastic repeat motifs; an N-terminal domain comprising 18 pentadecapeptide repeats (GGRPSDSYGAPGGGN) and a C-terminal domain comprising 11 tridecapeptide repeats (GYSGGRPGGQDLG) [3]. Each repeat is found entirely on the first and third exons (exon 1 and exon 3), respectively. In addition the exon 2 gene comprises the typical cuticular chitin binding domain (ChBD, PAKYEFNYQVEDAPSGLSFGHSEMRDGDFTTGQYNVL LPDGRKQIVEYEADQQGYRPQIRYEGDANDGSGPSGP) type R&R-2 that allows direct binding and strong interaction between the resilin and chitin during the process of resilin deposition and construction of the cuticle composite. In order to understand and assess the functional and structural properties of native resilin more completely, we cloned and expressed the full native resilin protein of the *Drosophilla* CG15920 gene, which encodes the three exons of the native protein (exon 1 + exon 2 + exon 3). The structural and elastic properties of uncrosslinked and crosslinked full length resilin were characterized by Fourier transform infrared spectroscopy (FTIR) and Atomic Force Microscopy (AFM). Here we present experimental data confirming that the peptide sequence identified as ChBD type R&R-2 in *D. melanogaster* resilin confers chitin binding to resilin, implying its role in the formation of the cuticle composite structure.

II. Results and Discussion

A. Gene construction, protein purification and crosslinking of full length resilin

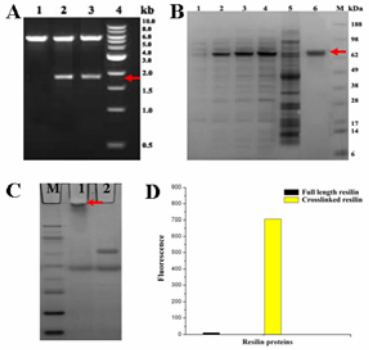

Fig. 1. Gene construction, protein purification and crosslinking of soluble full length resilin.

PCR amplification was used to successfully prepare the full length gene to construct the plasmid pET22b/Res containing the full length 1,818 bp resilin gene (Figure 1A). After the plasmid pET22b/Res was transformed into *E. coli* strain BL21 Star™ (DE3), the expression was carried out for 6 h at 37°C. Using a heat and salting-out method, the resilin protein was

purified (Figure 1B). Successful formation of crosslinked resilin was obtained using horseradish peroxidase. Cross-linked samples showed high molecular weight which barely entered the 4-12% SDS-PAGE gel, indicating significant polymerization (Figure 1C). Fluorometric analysis also indicated crosslinks, with absorption and emission maxima at 320 and 400 nm, respectively. Based on the fluorometric analysis results (Figure 1D), the fluorescence of this crosslinked resilin was higher than that of full length resilin.

MSYYHHHHHHDYDIPTTENLYFQGA
MGPEPPVNSYLPPSDSYGAPGQSGPGGRPSDSYGAPGGGNGGRPSDSYGA
PGQGQGQGQGQGGYAGKPSDTYGAPGGGNGNGGRPSSSYGAPGGGNGGRP
SDTYGAPGGGNGGRPSDTYGAPGGGGNGNGGRPSSSYGAPGQGQGNGNGG
RSSSSYGAPGGGNGGRPSDTYGAPGGGNGGRPSDTYGAPGGGNNGGRPSS
SYGAPGGGNGGRPSDTYGAPGGGNGNGSGGRPSSSYGAPGQGQGGFGGRP
SDSYGAPGQNQKPSDSYGAPGSGNGNGGRPSSSYGAPGSGPGGRPSDSYG
PPASGSGAGGAGGSGPGGADYDNDEPAKYEFNYQVEDAPSGLSFGHSEMR
DGDFTTGQYNVLLPDGRKQIVEYEADQQGYRPQIRYEGDANDGSGPSGP

Fig. 2. Amino acid sequence of 6H-resChBD. *Italics* mark the N-terminal tail; bold letters mark the ChBD that is missing in 6H-res protein.

B. Construction, expression and purification of 6H-resilin genes

The 975 and 1200 base pair products coding for resilin elastic repeats with or without the ChBD, respectively (6H-resChBD amino acids 19-415, 6H-res, amino acids 18-324, Figure 2), were expressed in *E. coli*. 6H-res protein was produced as control to confirm that the chitin binding is conferred by the putative ChBD. Specific chitin binding was evident only for 6H-resChBD (Figure 3). Equilibrium adsorption isotherms were conducted and a Kd of 1.6 μM and Bmax of 0.082 μmol/gr were calculated from a nonlinear regression of the adsorption isotherms (Figure 4).

C. Conformational properties of resilin

The FTIR spectra of full length and crosslinked resilins are shown in Figure 5A and 5B, which includes an expansion of the Amide I region for secondary structure analysis. The broad nature of the Amide I bands (centered around 1650 cm^{-1}) indicates a wide range of heterogeneous conformations, and peak deconvolution suggested potential contributions from all known secondary structures. The band between 1635 and 1655 cm^{-1} (centered around 1650 cm^{-1}) exhibited characteristics of random coil configurations (more than 40%). This high degree of disorder is also consistent with the observed CD spectra (Figure 5C). The crosslinked resilin and the uncrosslinked full length resilin had similar FTIR and CD spectra, and hence had similar secondary structure distributions. These data suggest that the full length recombinant resilin chains are mobile, and sample a wide range of conformations, which is also the case for the crosslinked resilin.

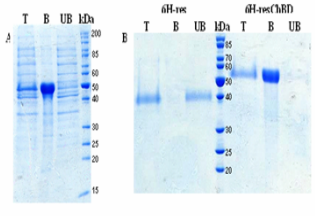

Fig. 3. Chitin binding of 6H-resChBD.

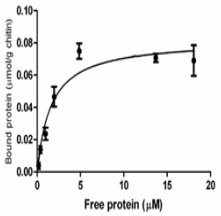

Fig. 4. Non-linear regression of 6H-resChBD binding to chitin.

D. Mechanical properties of full length and crosslinked resilin

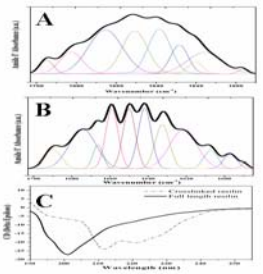

Fig. 5. Secondary structure analysis of full length and crosslinked resilins.

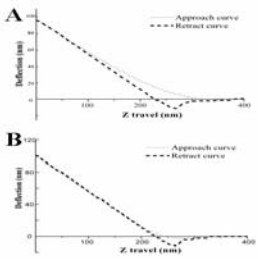

Fig. 6. Elasticity of resilins by AFM. Force-distance curves were recorded for the full length resilin (A) and crosslinked resilin (B).

Resilience is a measure of the ability of a material to deform and recover and it has become routine to use AFM to measure the modulus or stiffness of materials with resolution of nanometers, similar to a conventional compression tests [4]. Force-distance curves for both samples are shown in Figure 6. Compared with 92% resilience of the partial resilin clone, rec1-resilin [5], the full length resilin was 94% (±1%), and 96% (±2%) for the crosslinked material. Thus the full length protein offered similar material functions to the partial clone. This resilience is superior to that of a known low-resilience rubbers, such as chlorobutyl rubber (56%), and even to high-resilience polybutadiene rubbers (80%).

III. CONCLUSIONS

Full length recombinant resilin was generated and characterized. The material features of this protein were compared to previous studies where partial clones and proteins were generated and found to be comparable in both structure and function. Moreover, we showed that the chitin binding domain has high affinity to chitin implying for its role in the formation of the resilin-chitin composite in the cuticle.

ACKNOWLEDGEMENT

We would like to acknowledge the assistance of Qiang Lu with the AFM. We are also grateful to Dr. Hanna Dams-Kozlowska for technical assistance. Support from the NIH P41 Tissue Engineering Resource Center (NIBIB) is gratefully acknowledged.

REFERENCES

[1] T. Weis-Fogh, "A Rubber-Like Protein in Insect Cuticle," *J. Exp. Biol.*, vol. 37, pp. 887-907, 1960.

[2] S.O. Andersen, "The Crosslinks in Resilin Identified as Dityrosine and Trityrosine," *Biochim. Biophys. Acta*, vol. 93, pp. 213-215, 1964.

[3] D.H. Ardell and S.O. Andersen, "Tentative identification of a resilin gene in *Drosophila melanogaster*," *Insect Biochem Mol Biol.*, vol. 31, pp. 965-970, 2001.

[4] M.G. Huson and J.M. Maxwell, "The measurement of resilience with a scanning probe microscope," *Polymer Testing*, vol. 25, pp. 2-11, 2006.

[5] C.M. Elvin, A.G. Carr, M.G. Huson, J.M. Maxwell, R.D. Pearson, T. Vuocolo, N.E. Liyou, D.C.C. Wong, D.J. Merritt, and N.E. Dixon, *Nature*, vol. 437, pp. 999-1002, 2005.

Non-physiological mineral deposition *in vitro* by primary human osteoblasts under osteogenic conditions

L.F. Charles, J.L. Woodman, A.J. Goldberg, G.A. Gronowicz, L.T. Kuhn
University of Connecticut Health Center
263 Farmington Avenue
Farmington, CT 06032

***Abstract*—The pluripotency of human embryonic stem cells (hESCs) provides the unique opportunity to derive tissue specific cells, an ability of particular interest in regenerative medicine. In the study of bone regeneration, there is interest in directing hESCs to mesenchymal stem cells (MSCs), which under the appropriate conditions gives rise to mineral-producing osteoblasts. To evaluate the efficiency of such a process and cellular functionality, standard *in vitro* mineralization tests are employed to determine the cells' ability to generate a mineralized matrix. To guide the cells in these tests from their progenitor state to functional osteoblasts, osteogenic supplements must be provided in culture. However, it is critical to discern between physiological (cell-mediated) and non-physiological mineralization *in vitro*. Here, we investigated the mineralization pattern of human osteoprogenitor cells in the presence of varying concentrations of the common osteogenic supplements fetal bovine serum, β-glycerol phosphate, and dexamethasone.**

INTRODUCTION

Our laboratory is interested in differentiating human embryonic stem cells (hESCs) into osteoblasts for bone regeneration in large boney defects. To guide stem cells to functional osteoblasts, osteogenic supplements such as ascorbic acid, β-glycerol phosphate (β-GP), dexamethasone, and fetal bovine serum (FBS) must be provided in culture. The role of these supplements has been studied previously in mammalian cell culture systems.

In *in vitro* osteogenic cultures, ascorbic acid is necessary to promote extracellular matrix production. It has been shown to act as a co-factor in the hydroxylation of proline and lysine residues in collagen [1-2]. *In vitro*, β-glycerol phosphate is a mineralization promoter which induces nodule formation and mineral deposition. There have been concerns that high concentrations of β-glycerol phosphate lead to dystrophic mineralization because of the ability of alkaline phosphatase produced by osteogenic cells to cleave phosphate groups from β-glycerol phosphate and cause non-physiological calcium phosphate deposits [3]. Dexamethasone is a glucocorticoid which can act in both a stimulatory and inhibitory manner on osteogenic differentiation [4]. Some studies have provided evidence for the necessity of dexamethasone in *in vitro* mineral formation, particularly in rat marrow-stromal derived cells [5], and human mesenchymal stem cells [4].

The concentration of the supplements used in culture is critical because an excess will lead to non-physiological mineral deposition that occurs even in the complete absence of osteoblast differentiation [6].

METHODS

Since *in vitro* mineralization tests are one of the primary screens in developing osteoprogenitors especially from hESCs, it is important to determine appropriate, yet much optimal, osteogenic culture conditions for assessing their functional ability. Accordingly, we performed osteogenesis optimization studies using varying concentrations of three common osteogenic supplements: dexamethasone, β-glycerol phosphate, and fetal bovine serum (FBS). Primary human osteoprogenitor (pHOB) cells obtained from bone chip outgrowths [7] were used for the studies. Cells cultured for up to 21 days were assayed for differentiation by real time-qPCR using TaqMan gene expression assays (Applied Biosystems, USA). Human bone cDNA (DV Biologics, USA) was used as a positive control for osteogenic gene expression. Mineral deposition was assessed by image analysis of fluorescent micrographs taken after xylenol orange (XO) staining and by further calcium content analysis using a calcium detection kit (Eagle Diagnostics, USA). Human fibroblasts were used as a negative control for calcium content assays. Concentrations of supplements were as follows, dexamethasone: 0 and 100 nM; β-glycerol phosphate: 4 and 10 mM; and fetal bovine serum: 10 and 15%. Ascorbic acid 2-phosphate (AA2P) concentration of 50μM was used for all experiments.

RESULTS

Results showed that dexamethasone was required for mineralization in the primary human osteoblasts (Fig. 1). In the presence of dexamethasone, independent of the concentration of the other supplements, mineral deposition was observed throughout the culture along with high calcium concentrations (Fig. 2A). Increasing the FBS concentration from 10 to 15% did not result in any change in observed mineralization. However, RT-qPCR analysis of osteoblast-related genes in pHOB cultures, relative to human bone cDNA, showed a lack of bone sialoprotein (BSP) and osteocalcin (OCN) expression, two markers related to mature, mineral-depositing osteoblasts (Fig. 3).

Importantly, human fibroblast cells cultured in osteogenic media containing 100 nM dexamethasone and varying concentrations of β-glycerol phosphate (0, 2, 4 mM)

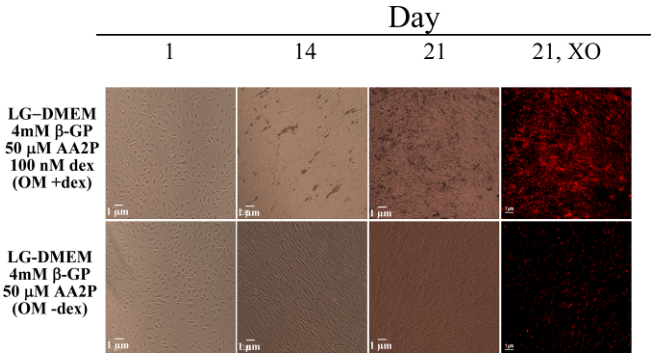

Fig. 1. Phase contrast and xylenol orange fluorescent images of pHOB cells' morphology on treated tissue culture plastic at various times indicated throughout the culture. Phase contrast images are shown for cultures in osteogenic media (OM) with (OM +dex) or without (OM –dex) dexamethasone (100 nM). Images labeled "21, XO" represent fluorescent images of the areas shown at day 21 stained by xylenol orange.

unexpectedly showed similar mineral deposition and calcium concentrations comparable to osteogenic cultures (Fig. 2B). The RT-qPCR data of osteoblast cultures and mineral deposition in fibroblast cultures suggest that the observed mineral in the osteogenic cultures is non-physiological or dystrophic. It did not occur in cell culture medium alone without cells, thus there is an element of mediation by the cells. This poses a problem for determining cellular functionality.

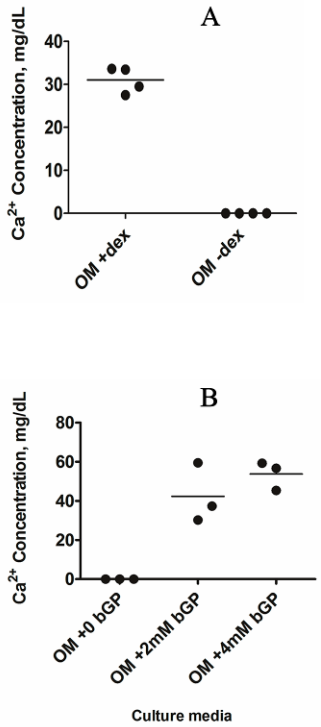

Fig. 2. Calcium content measurement of pHOB (A) and human fibroblast (B) cells. In (A) cells were cultured in low glucose DMEM, 4mM β-GP, 50 μM AA2P, 10% FBS (OM), in the presence or absence of 100 nM dexamethasone. In (B) cells were cultured in OM, 100 nM dexamethasone, and varying concentrations of β-GP. OM – osteogenic media.

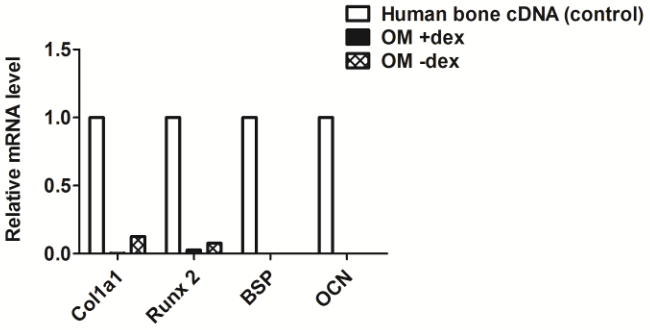

Figure 3. Expression of some osteogenic genes in pHOB cells cultured in cultured in low glucose DMEM, 4 mM β-GP, 50 μM AA2P, 10% FBS in the presence (OM +dex) or absence (OM-dex) of 100 nM dexamethasone relative to human bone cDNA.

CONCLUSION

We conclude that osteogenic conditions commonly used by many investigators led to non-physiological mineral deposition of primary human osteoblasts that was not correlated to the cell's differentiation status. Further work is needed to identify the conditions that can be used for *in vitro* mineralization screening of osteoblastic cultures while preventing non-physiological mineral deposition.

REFERENCES

[1] R.I. Schwartz. "Procollagen secretion meets the mininmum requirements for the rate-controlling step in the ascorbate induction of procollagen synthesis." *J. Biol. Chem*. 260:3045-3049, 1985.

[2] R.I. Schwartz, P. Kleinman, N. Owens. "Ascorbate can act as an inducer of the collagen pathway because most steps are tightly coupled." *Ann NY Acad Sci* 498:172–185, 1987.

[3] H.I. Khouja, A. Bevington, G.J. Kemp, R.G. Russell. "Calcium and orthophosphate deposits in vitro do not imply osteoblast-mediated mineralization: mineralization by betaglycerophosphate in the absence of osteoblasts." *Bone* 11:385-291, 1990.

[4] N. Jaiswal, S.E. Haynesworth, A.I. Caplan, S.P. Bruder. "Osteogenic differentiation of purified, culture-expanded human mesenchymal stem cells in vitro." *J Cell Biochem* 64:295-312, 1997.

[5] C. Maniatopolous, J. Sodek, A.H. Melcher. "Bone formation in vitro by stromal cells obtained from bone marrow of young adult rats." *Cell Tissue Res* 254:317–330, 1988.

[6] A.L. Boskey and R. Roy. "Cell culture systems for studies of bone and tooth mineralization." *Chem Rev* 108(11): 4716-4733, 2008.

[7] H. Zhang, C.G. Lewis, M.S. Aronow, G.A. Gronowicz. "The effects of patient age on human osteoblasts' response to Ti-6Al-4V implants in vitro." *J Orthop Res*.22(1):30-8, 2004.

The human umbilical vein as a biologic scaffold for vocal fold reconstruction

R.W. Chan
Biomedical Engineering; Otolaryngology – Head & Neck Surgery
University of Texas Southwestern Medical Center
Dallas, Texas 75390-9035

***Abstract* — A variety of extracellular matrix (ECM) scaffolds have been promising in various tissue engineering applications, such as the porcine small intestinal submucosa. Yet no particular scaffolds have been optimal for vocal fold regeneration. The decellularized human umbilical vein (HUV) is a novel allogeneic scaffold that has shown some promise for cardiovascular tissue engineering. This study examines the potential of the HUV as an acellular scaffold for engineering the vocal fold, in order to develop an implantable tissue substitute that can promote constructive tissue remodeling. A saline-based decellularization protocol was used to fabricate a biodegradable, acellular, three-dimensional scaffold from native HUV tissue. Histological examination and scanning electron microscopy demonstrated that native cellular materials in the HUV were removed with a fine three-dimensional structure of proteins and proteoglycans well preserved. Primary human vocal fold fibroblasts were seeded on the abluminal surface of the acellular HUV scaffold and cultured for 21 days. Significant proliferation and infiltration of the fibroblasts in the scaffold were observed. These data supported the promise of the HUV scaffold for vocal fold regeneration and restoration.**

I. Introduction

The human vocal fold is a highly differentiated layered structure optimally designed for vibration and sound production. In particular, the vocal fold lamina propria is primarily an extracellular matrix (ECM) that undergoes flow-induced self-oscillation under a unique micromechanical environment, including small- and large-amplitude oscillations (~1-3 mm) at high magnitudes of acceleration (up to 300 g) and at high frequencies (~100-300 Hz). Vocal fold fibroblasts regulate the expressions of matrix proteins, such as collagen, elastin, decorin, fibromodulin, hyaluronan, and fibronectin, and disturbed patterns of protein regulation lead to various laryngeal pathologies such as vocal fold scarring, vocal polyps, cysts, and many other benign lesions of the lamina propria. In order to engineer an implantable tissue replacement for the surgical repair of such ECM disorders, this study examines the potential of a novel allogeneic, acellular scaffold, the human umbilical vein (HUV), for regeneration of the vocal fold lamina propria ECM.

II. Methods

Following the protocol reported by Daniel et al. [1], native HUV tissue was harvested and frozen onto a stainless steel mandrel with a 6mm diameter at -80ºC for two days before dissection. An automated dissection procedure using a high-speed, steel cutting tool was performed with the tissue/mandrel secured on a modified lathe, resulting in a uniform tissue thickness of 750μm when frozen [1]. After dissection, the HUV tissue was thawed by immersion in double distilled water at 5ºC for 1 hour.

HUV tissue sections were treated with a novel proteolytic enzyme-free, detergent-free saline-based decellularization protocol developed in our laboratory [2]. Briefly, the protocol involved the use of a highly hypertonic salt (3M NaCl) solution creating an extreme osmotic stress for cells in the HUV, followed by cycles of osmotic stress with incubation in PBS solution and ethanol under mechanical agitation. RNase and DNase were added to remove the nucleic acids exposed by rupture of the cell membrane [2]. Antibiotics were used to maintain tissue sterility. Structure of the acellular HUV scaffold was examined with light microscopy and scanning electron microscopy. Human vocal fold fibroblasts from primary culture were seeded on the abluminal surface of the scaffold, and were cultured in 5% CO_2 at 37ºC for 21 days.

III. Results and Discussion

Figure 1 shows the structure of the decellularized HUV scaffold, demonstrating the removal of native cellular structures in the HUV tissue. The three-dimensional structure of the matrix protein network is well preserved, as shown in the scanning electron micrograph (Figure 2). Twenty-one days following seeding onto the abluminal surface of the acellular scaffold, primary vocal fold fibroblasts have proliferated and infiltrated in the acellular scaffold to a depth of around 600 microns, roughly the thickness of Wharton's jelly, i.e., the connective tissue layer in the HUV scaffold (Figure 3).

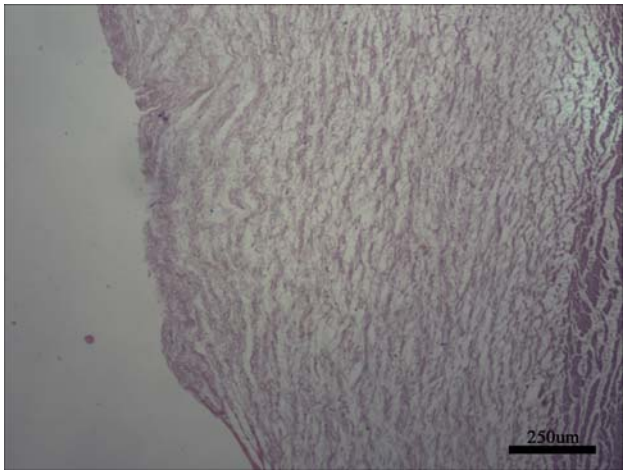

Figure 1: An acellular HUV scaffold stained with H&E. Note the luminal surface to the right and abluminal surface to the left. Total magnification = 40 ×.

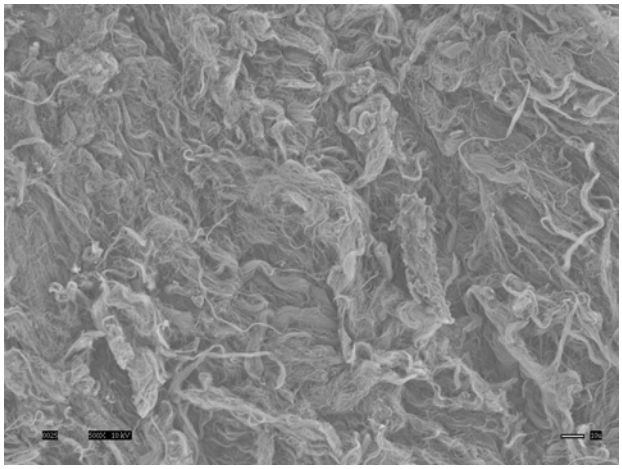

Figure 2: Scanning electron micrograph of the abluminal surface of an acellular HUV scaffold, showing the 3-D protein network of the ECM. Total magnification = 500 ×.

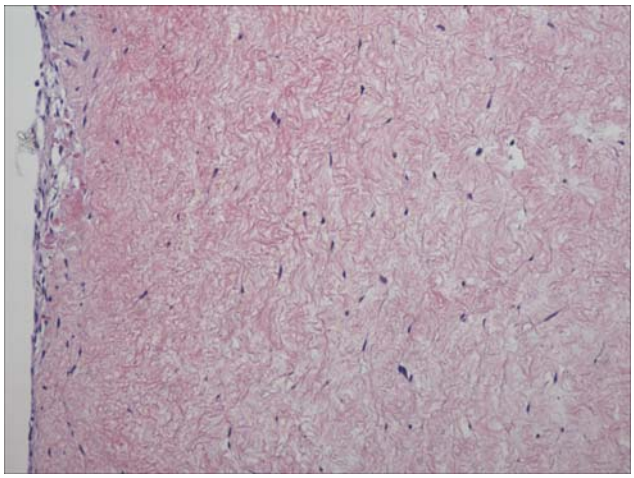

Figure 3: An acellular HUV scaffold recellularized with primary human vocal fold fibroblasts (H&E staining). Significant proliferation and infiltration of the fibroblasts can be seen. Total magnification = 100 ×.

IV. Conclusion

The results of this study showed that our saline-based decellularization protocol was capable of fabricating a three-dimensional, biodegradable, acellular scaffold from native HUV tissue. Preliminary findings on the histological structure of the scaffold, as well as proliferation and infiltration of human vocal fold fibroblasts in the scaffold demonstrated the biocompatibility of the acellular HUV scaffold. These data supported the potential of the scaffold for vocal fold tissue engineering applications.

Acknowledgement

This work was supported by NIH Grant R01 DC006101. We would like to thank Dr. Peter S. McFetridge for sharing his HUV tissue and dissection technology with us.

References

[1] J. Daniel, K. Abe, and P.S. McFetridge, "Development of the human umbilical vein scaffold for cardiovascular tissue engineering applications," *ASAIO J*., vol. 51, pp. 252-261, 2005.

[2] C.C. Xu, R.W. Chan, and N. Tirunagari, "A biodegradable, acellular xenogeneic scaffold for regeneration of the vocal fold lamina propria," *Tissue Eng*., vol. 13, pp. 551-566, 2007.

Screening Materials and Soluble Compounds for Mineralized Tissue Engineering

D.M. Brey and J.A. Burdick
Department of Bioengineering
University of Pennsylvania
Philadelphia, PA

***Abstract*—As more materials and soluble molecules are developed, the ability to screen these materials for applications in tissue engineering becomes increasingly important. A combinatorial library of poly(β-amino ester)s was screened to identify an osteoconductive material based on material properties and cellular interactions. The optimal material, A6, was then implanted into a critical-sized cranial defect loaded with a known osteoinductive factor to promote mineralized tissue formation. The identification of new osteoinductive cues from a library of known compounds was completed using high-throughput screening techniques. Several potential 'hits' were then screened in a dose response study that found 5 compounds to be the most potent. These methods of rapidly identifying materials and compounds from large libraries will be increasingly important in the field of tissue engineering.**

I. Introduction

The field of tissue engineering has long searched for the proper combination of materials, soluble factors, and cellular therapies for a variety of clinical applications. These studies have often involved narrowly focused experiments on materials with only small variations, limited exposure to expensive growth factors or genetic therapies, or the use of different populations of multipotent stem cells. Recently, combinatorial libraries of biomaterials have largely increased the pool of potential materials for use as tissue engineering scaffolding [1,2]. Although pharmaceutical companies have used combinatorial syntheses and screening techniques to identify potential drug therapies [3], these approaches are only now finding use within the field of tissue engineering. This technology may be very useful in identifying formulations for optimal tissue regeneration approaches. In our work, a new library of photocrosslinkable, biodegradable poly(β-amino ester)s (PBAEs) has been developed as a class of materials for a range of biomedical applications [4]. This library has being screened to identify a polymer with osteoconductive properties. Libraries of soluble factors have also been screened using high throughput technology to identify potential osteoinductive molecules. The development of these material synthesis and screening techniques will be useful in rapidly detecting useful formulations for applications in tissue engineering.

II. Materials and Methods

A. *Macromer Synthesis and In Vitro Screening:*

A library of commercially available amines and diacrylates [4] were mixed at a diacrylate to amine ratio of 1.2:1 at 90°C overnight. The photoinitiator 2,2-dimethoxy-2-phenyl acetophenone (DMPA) was added to the liquid macromers at a final concentration of 0.5% (w/w). Bulk polymer, thin films, and scaffolds were polymerized with UV light exposure (~10 mW/cm^2, 365 nm, 10 min, Blak-Ray). Polymer slabs were degraded in phosphate buffered saline (PBS) on an orbital shaker at 37ºC. Compression testing was completed using a Dynamic Mechanical Analyzer (Q800 TA Instruments) at a rate of 10%/min. The modulus was determined as the slope of the stress/strain curve at low strains (<20%). Human mesenchymal stem cells (hMSCs, Lonza) were seeded on thin films of selected polymers in 24 well plates at 6000 cells/cm^2. Cell viability (mitochondrial activity) was measured using Alamar Blue (Invitrogen) over 7 days after seeding. Initial osteogenic activity was measured using a fluorescent alkaline phosphatase assay (ALP, Sigma) after 3 days in osteogenic media for candidates that demonstrated viability.

B. *Animal Model:*

Scaffolds were prepared as described previously [5], using a poragen leaching technique with sintered 200 μm PMMA beads. Scaffold composites were then made by partially filling the void space with collagen (Inamed Biomaterials) either alone or loaded with 2μg of rhBMP-2 (R&D systems).

Scaffolds were then implanted into a critical sized cranial defect (8mm) in rats for 6 weeks. Implants were processed for histology and calvaria were scanned using a VivaCT40 uCT scanner (Scanco, 55 kVp, 145 mA, 200 ms). Scans were performed with an isotropic voxel size of 10.5 μm and images were reconstructed in 1,024 x 1,024 pixel matrices. A lower threshold of 743.4 mg/cm^3 and an upper threshold of 2000 mg/cm^3 were determined by visual inspection to best distinguish between bone and non-bone material.

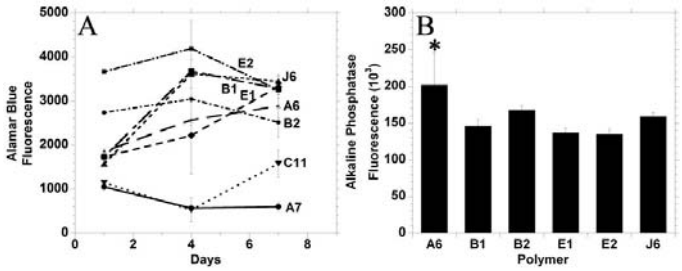

Figure 1. (A) Alamar Blue results of hMSCs grown on thin films of polymer and (B) the alkaline phosphatase activity in the hMSCs after 3 days in osteogenic media. * denotes significance from all groups except B2.

C. *High-throughput Screening of Soluble Factors*

A National Institute of Neurological Disorders and Stroke (NINDS) library of 1040 known compounds were screened for osteogenic promotion and inhibition of MSCs. Human MSCs (P3-4) plated on 384 well plates overnight in growth media. The media was then switched to either OG+ (positive control, growth + 10 nM dexamethasone, 25 μg/mL ascorbic acid-2-phosphate, and 10 mM β-glyecerol phosphate), or OG- (negative control, OG+ without dexamethasone) media and soluble factors were added. Media and factors were refreshed after 4 days. On day 8, Alamar Blue (Invitrogen) was used to determine cell viability and a fluorescent alkaline phosphatase assay (Sigma) was used to mark osteogenic differentiation.

III. Results and Discussion

A. *Macromer Synthesis and In Vitro Screening:*

A polymer library (120 formulations) was first screened for degradation. From this library, 10 polymers were identified as having the preferred degradation rate (~3-5 months) and degradation profiles that indicated gradual mass loss. MSC viability varied on these 10 polymers. C11 and C12 both created an acidic environment and all cells died. Several polymers supported an initial increase in activity over the first few days, but longer viability decreased at 7 days. This could be due to some cytotoxicity as the polymers degraded. A6 and E1 both exhibited steady increases in mitochondrial activity with culture, indicative of proliferation. The ALP activity was measured at 3 days in osteogenic media on samples that supported cell viability and was found to be significantly greater on A6 films than on other polymers except B2. Therefore, A6 was used for implantation.

B. *Animal Model:*

Critical sized defects created in rat calvaria were left empty or filled with scaffolds that were (i) empty, (ii) loaded with a collagen gel, or (iii) loaded with rhBMP-2 collagen gel. The rats were sacrificed at 6 weeks and μCT of the calvaria showed limited bone formation in all cases except scaffolds implanted with BMP-2.

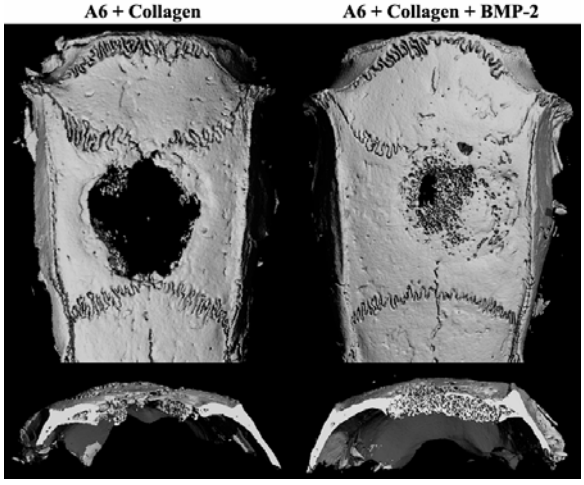

Figure 2. Sample μCT reconstructions and cross sections of calvaria 6 weeks after surgery.

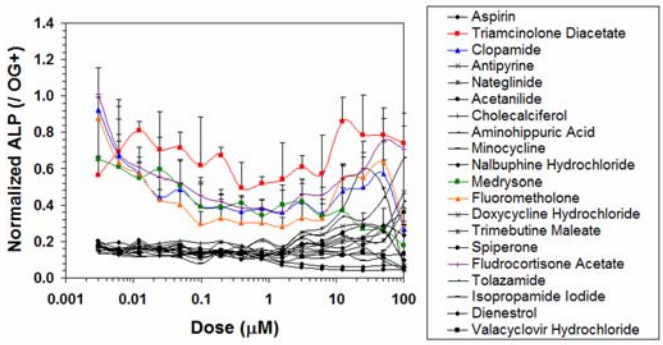

Figure 3. Dose response curves of alkaline phosphatase activity of identified osteoinductive molecules. Values relative to samples grown in traditional osteogenic media.

This was found in both the radiographs and histology, as well as the μCT. Inspection of the bone via μCT and histology indicates that the bone likely fills the pores in the scaffold, yet the polymer still remains. As expected, while these polymers have been shown to be biocompatible and to have osteoconductive properties, their presence alone is not enough to promote mineralization; however, the addition of rhBMP-2 led to substantial mineralization.

C. *High-throughput Screening of Soluble Factors*

From the original library of 1080 compounds and after 7 days of culture, 36 compounds were identified as potential osteogenic promoters and 20 were identified as osteogenic inhibitors. These molecules also met the criteria of maintaining at least 80% of the viability of untreated cultures and included several glucocorticoids, antibacterials, and analgesics. Of the promoters, 5 compounds increased alkaline phosphatase activity at low (tens of nM) concentrations.

Acknowledgement

The authors would like to acknowledge Dr. Diamond, Nuzhat Motlekar, and the PCMD for assistance and funding; and the Center for Research in FOP and Related Disorders at the University of Pennsylvania for funding.

References

[1] R. Hoogenboom, M.A.R. Meier, U.S. Schubert, "Combinatorial methods, automated synthesis and high-throughput screening in polymer research: Past and present," *Macromolecular Rapid Communications*, vol 24 pp 16-32, 2003.

[2] H. Park, C. Cannizzar, G. Vunjak-Novakovi, R. Langer, C.A. Vacant, O.C. Farokhzad, "Nanofabrication and microfabrication of functional materials for tissue engineering.," *Tissue Engineering*, vol 13, pp 1867-1877, 2007.

[3] M. Goldberg, K. Mahon, D. Anderson, "Combinatorial and rational approaches to polymer synthesis for medicine," *Advanced Drug Delivery Reviews,* vol 60, pp 971-978, 2008.

[4] D.G. Anderson, C.A. Tweedie, N. Hossain, S.M. Navarro, D.M Brey, K.J. Van Vliet, R. Langer, J.A. Burdick, "A combinatorial library of photocrosslinkable and degradable materials," *Advanced Materials* vol 18 pp 2614-+, 2006.

[5] D.M. Brey, J.L. Ifkovits, R.I. Mozia, J.S. Katz, J.A. Burdick, "Controlling poly(beta-amino ester) network properties through macromer branching," *Acta Biomaterialia* vol 4, pp 207-217, 2008.

Creation of Vessel-like Patches Enabled by Poly(caprolactone)/Collagen/Elastin Composite Nanofibers

Xiaochuan Yang, Hongjun Wang.
Chemistry, Chemical Biology and Biomedical Engineering Dept.
Stevens Institute of Technology
Castle Point on Hudson
Hoboken, NJ, 07030

Abstract – **It is critical to fabricate ideal scaffolds for tissue engineered vascular graft. Nanofibers composted with collagen, elastin and polycaprolactone (PCL) were prepared by electrospinning. The obtained composite fibers had an average diameter around 300-500 nm. Mouse smooth muscles cells and endothelial cells cultured on these composite fibrous meshes showed enhanced cell attachment and accelerated cell proliferation. Three-dimesional cell-scaffolds construct were fabricated using layer-by-layer electrospinning technique. Taken together, the electrospun PCL fibers containing collagen, elastin and PCL show a great potential in vascular tissue engineering.**

I. Introduction

In vascular tissue engineering, it is very important to fabricate scaffolds which can provide vascular cells a stimulatory environment, and construct multiple layered cell-scaffold structure for facilitating tissue formation. Electrospinning has been considered a very promising technique to fabricate nanofiber scaffold for tissue engineering applications. We are attempting to develop biomimetic nanofibrous scaffolds, together with a layer-by-layer electrospinning technique to create multiple layered cell-fibers structure for tissue engeering[1], which can be used to regenerate vascular grafts.

II. Methods

Composite nanofibers were prepared by electrospinning a blended solution of collagen, elastin and polycaprolactone (PCL). Mouse smooth muscles cells and endothelial cells were cultured on these composite fibrous meshes. F-actin staining was used to illustrate cell morphology on the composite nanofibers. MTT assay was performed to evaluate cell attachment and proliferation on the fabricated scaffolds. 3-D cell-fiber complex structure was fabricated via layer-by-layer electrospinning technique.

III. Results

The obtained electrospun fibers had smooth surface with an average diameter around 300-500 nm (Fig. 1 C). F-actin staining results revealed that this composite fibrous meshes also favoured the typical cell morphology for both cell types (Fig. 1 A, B). Mouse smooth muscles cells and endothelial cells showed enhanced cell attachment and accelerated cell proliferation on these composite nanofiber scaffolds (Fig. 2). Three-dimensional (3D) cell-scaffolds complex structure composed of multilayered smooth muscle cells, endothelial cells and nanofibers were created, which showed homogeneous cell distribution and uniform tissue formation across the entire construct (H&E staining) (Fig. 3).

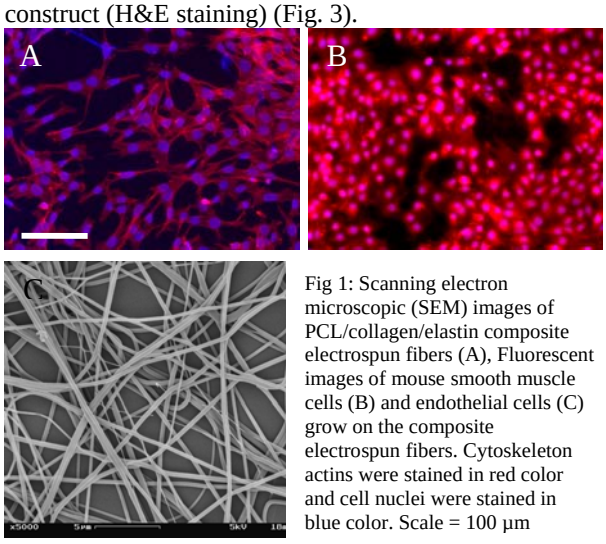

Fig 1: Scanning electron microscopic (SEM) images of PCL/collagen/elastin composite electrospun fibers (A), Fluorescent images of mouse smooth muscle cells (B) and endothelial cells (C) grow on the composite electrospun fibers. Cytoskeleton actins were stained in red color and cell nuclei were stained in blue color. Scale = 100 µm

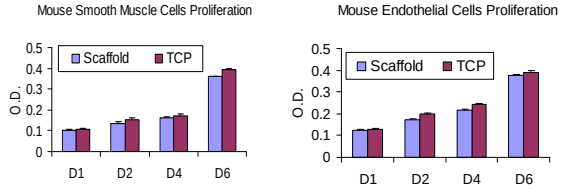

Fig 2: Mouse smooth muscle cells and endothelial cells proliferate on the composite nanofibers tested using MTT assay.

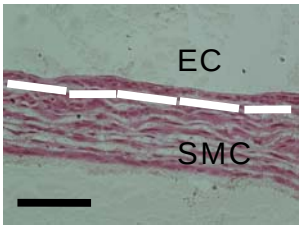

Fig 3: 3-D cell-scaffolds structure was fabricated using layer-by-layer electrospinning technique. Scale = 100 μm

IV. Conclusions

A Layer-by-Layer cell-fiber assembly approach toward 3D tissue formation was proven by using elctrospun fibers and mouse blood vessel cells in this study. A continuous new tissue formation was observed in the L-b-L–assembled cell-scaffold constructs. In summary, vessel-like patch graft can be fabricated using mouse smooth muscle cells and endothelial cells together with composite collagen, elastin and PCL electrospun nanofibers.

References:

1. Yang X., Shah DJ., and Wang H. Tissue Engineering Part A. 2009(15); 945-956